

**POSITION AND ORIENTATION RECOVERY OF  
INTRAMEDULLARY NAIL DISTAL HOLES**



**A THESIS SUBMITTED IN PARTIAL FULFILLMENT  
OF THE REQUIREMENTS FOR  
THE DEGREE OF MASTER OF ENGINEERING  
(BIOMEDICAL ENGINEERING)  
FACULTY OF GRADUATE STUDIES  
MAHIDOL UNIVERSITY**

**2007**

**COPYRIGHT OF MAHIDOL UNIVERSITY**

Thesis  
Entitled

**POSITION AND ORIENTATION RECOVERY OF  
INTRAMEDULLARY NAIL DISTAL HOLES**



*Paweena U-Thainual*

Miss Paweena U-Thainual  
Candidate

*Jackrit Suthakorn*

Assist. Prof. Jackrit Suthakorn,  
Ph.D., (Robotics)  
Major-Advisor

*Saowapak Sothvirat*

Lect. Saowapak Sothvirat, Ph.D.,  
(Electrical Engineering)  
Co-Advisor

*B. Mahaisavariya*

Prof. Banchong Mahaisavariya,  
M.D.  
Dean  
Faculty of Graduate Studies

*Jackrit Suthakorn*


Assist. Prof. Jackrit Suthakorn,  
Ph.D., (Robotics)  
Chair  
Master of Engineering Programme in  
Biomedical Engineering  
Faculty of Engineering


Thesis  
Entitled


**POSITION AND ORIENTATION RECOVERY OF  
INTRAMEDULLARY NAIL DISTAL HOLES**


was submitted to the Faculty of Graduate Studies, Mahidol University  
For the degree of Master of Engineering (Biomedical Engineering)  
on  
December 3, 2007


  
Miss Paweena U-Thainual  
Candidate

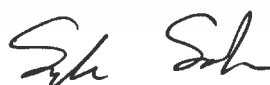
  
Prof. Banchong Mahaisavariya, M.D.,  
Dip Thai Brd Orthop Surg., FRCS (T)  
Member


  
Assist. Prof. Warakorn Charoensuk,  
Ph.D., (Electrical Engineering)  
Chair


  
Admiral Paibul Nacaskul, Ph.D.,  
(Electrical Engineering)  
Member

  
Assist. Prof. Jackrit Suthakorn, Ph.D.,  
(Robotics)  
Member

  
Assist. Prof. Chatchai Neatpisarnvanit,  
Ph.D., (Electrical Engineering)  
Member

  
Lect. Saowapak Sotthivirat, Ph.D.,  
(Electrical Engineering)  
Member

  
Prof. Banchong Mahaisavariya, M.D.  
Dean  
Faculty of Graduate Studies  
Mahidol University

  
Assist. Prof. Rawin Raviwongse, Ph.D.  
Dean  
Faculty of Engineering  
Mahidol University

## ACKNOWLEDGEMENT

Firstly, I would like to express my profound thank to my major advisor, Assist. Prof. Dr. Jackrit Suthakorn, who always supports, teaches and pushes me to keep working all these years. I would like to thank him for his academic assistance, and encouragement throughout my master study. He is the first person who initiated my interest in Biomedical Engineering and Robotics. Without him, I would not have had the privilege of participating in such an interesting and successful research experience. To me, Dr. Jackrit is more than just an academic advisor; he is also a source of inspiration and wisdom in life both inside and outside school. I gratefully thank my co-advisor, Dr. Saowapak Sotthivirat, for her suggestion throughout my master study and her inputs and excellent Image processing classes I have attended. Thank you for her valuable time for improving my dissertation. I would like to thank Prof. Banchong Mahaisavariya, M.D. for his kindness and valuable information of the Closed Intramedullary Nailing of Femur. Without him, I would not have had an opportunity of attending the operation which is my interested topic. I would like to thank Assist. Prof. Dr. Warakorn Charoensuk and Assist. Prof. Dr. Chatchai Neatpisarnvanit for their valuable suggestions throughout my master study and research.

I would also like to thank my committee members, Assist. Prof. Dr. Jackrit Suthakorn, Assist. Prof. Dr. Warakorn Charoensuk, Assist. Prof. Dr. Chatchai Neatpisarnvanit, Dr. Saowapak Sotthivirat, Prof. Banchong Mahaisavariya and Admiral Dr. Paibul Nacaskul for their participations in this work. My dissertation will consume some of their valuable time. I really do appreciate their efforts.

I would like to thank Assoc. Prof. Dr. Gabor Fichtinger for his academic assistance, valuable guidance throughout my research at Johns Hopkins University. To my friends at Hopkins: Ameet, Hassan, Pezhman, Iulian, Anton, Ankur, Gouthami, Panadda, and Ofri, I really had a good time with everyone over the period of 6 months. They deserve special thanks for helping me get through this working and coming up with helpful suggestions. Additionally, I would like to thank Peerapat Owatchaiyapong for his kindness and his helpful throughout my dissertation. I would like to give my thanks to all my friends and staffs at Dept. of Biomedical Engineering and the Center for Biomedical and Robotics Technology, Faculty of Engineering, Mahidol University, Thailand, for all the support.

Furthermore, I would like to acknowledge the Thailand Graduate Institute of Science and Technology (TGIST) and National Metal and Materials Technology Center (MTEC) of National Science and Technology Development Agency (NSTDA), Thailand, for the good supporting in education and research they offered me. I would like to thank the Center for Biomedical and Robotics Technology (BART LAB), Mahidol University, Thailand, for the good supporting in everything. Without BART LAB I would not be able to finish my master study and research.

Finally, I would like to thank my parents for their supporting and understanding for my hard working all these years. I also thank to my sisters for their hard working to support our family.

Paweena U-Thainual

**POSITION AND ORIENTATION RECOVERLY OF INTRAMEDULLARY NAIL  
DISTAL HOLES****PAWEENA U-THAINUAL 4837544 EGBE/M****M.Eng. (BIOMEDICAL ENGINEERING)****THESIS ADVISORS: JACKRIT SUTHAKORN, Ph.D. (ROBOTICS),  
SAOWAPAK SOTTHIVIRAT, Ph.D. (ELECTRICAL ENGINEERING)****ABSTRACT**

Numerous orthopedic operations require locating of implants and internal organs such as bone. Currently, this requires x-ray exposure during the surgery to allow the surgeon to indicate the position and orientation of the patient's internal organs and medical inserting devices. An orthopedic operation, called "Closed Intramedullary Nailing of Femur (Closed Nailing)," is one of the frequent cases among orthopedic surgeries. This surgery also requires accurate positioning and orientating of the implant. One of the most difficult tasks for surgeons is to identify the position and orientation of the screwing holes (typically in circular shape) at both ends of the intramedullary nail (IMN) after being inserted into a patient's femoral canal. The distal hole locations may be shifted by external forces and torques applied to the IMN during the insertion procedure resulting in the IMN to deform. In the conventional closed nailing surgery, surgeons require high experience, and a number of trial-and-error adjustments to correct the path for inserting the screws through those distal holes. The process can be done by gradually adjusting the shooting angle until the projection of the two distal holes is seen as circular as possible on the x-ray image. Therefore, both surgeon and patient are continuously exposed to a great amount of x-ray exposure from the fluoroscopic imaging system. This could harm the surgeon and patient for their long term health.

This study investigates a new algorithm to recover the 3-D pose (position and orientation) of distal holes in the intramedullary nail by using only three x-ray imaging projections, such as AP (anterior/posterior) and lateral views. The algorithm is based on inverse kinematics approach. A mathematical model and an algorithm are developed and described using group theory. The study includes mathematical modeling, algorithm formulations, simulation and experimental results and conclusion of the algorithm performance.

**KEYWORDS: DISTAL LOCKING/ INTRAMEDULLARY NAILING/  
NAVIGATION SYSTEM IN ORTHOPAEDIC SURGERY****110 pp.**

การค้นหาค่าตำแหน่งและทิศทางของรูสกรูปลายแกนตามกระดูก (POSITION AND ORIENTATION RECOVERLY OF INTRAMEDULLARY NAIL DISTAL HOLES)

ปริญญานิพนธ์ 4837544 EGBE/M

วศ.ม. (วิศวกรรมชีวการแพทย์)

คณะกรรมการควบคุมวิทยานิพนธ์ : จักรกฤษณ์ สุทธากรณ์, Ph.D. (Robotics), เสาวภาคย์ โสคติ

วิรัช, Ph.D. (Electrical Engineering)

บทคัดย่อ

การศัลยกรรมทางออร์โธปิดิกส์ มีความจำเป็นที่จะต้องรู้ตำแหน่งของอวัยวะภายในเช่น กระดูก โดยระบบที่มีใช้ในปัจจุบันใช้วิธีการนำทางด้วยการถ่ายภาพรังสีจำนวนหลายครั้งตลอดระยะเวลาการผ่าตัด เพื่อให้ศัลยแพทย์สามารถระบุตำแหน่งและทิศทางของอวัยวะภายในของผู้ป่วยและเครื่องมือ การผ่าตัด “ยึดตรึงกระดูกหักด้วยแกนตามกระดูกที่บริเวณกระดูกต้นขา” เป็นอีกหนึ่งกรณีที่พบเห็นมากในการศัลยกรรมทางออร์โธปิดิกส์ หลังจากที่ศัลยแพทย์สอดใส่แกนตามกระดูกเข้าไปในโพรงกระดูกแล้ว จำเป็นจะต้องทำการใส่สกรูล็อคแกนตามกระดูกที่ส่วนต้นและท้ายของแกนตามกระดูก ขั้นตอนนี้ต้องใช้แพทย์ที่มีความสามารถและประสบการณ์สูงในการอ่านภาพถ่ายรังสี และวิเคราะห์ในระหว่างการผ่าตัด ทั้งยังต้องใช้การถ่ายภาพรังสีแบบเดาสุ่มเพื่อหาค่าตำแหน่งของรูใส่สกรู วิธีการนี้มีข้อเสียคือทั้งคนไข้และศัลยแพทย์ต้องรับรังสีเป็นปริมาณมากในระหว่างการผ่าตัดซึ่งเป็นอันตรายต่อสุขภาพในระยะยาว นอกจากนี้ระบบนี้ยัง การพัฒนาระบบการนำทางสำหรับช่วยในการผ่าตัด โดยให้มีจำนวนการถ่ายภาพรังสีน้อยที่สุด

การศึกษานี้เพื่อค้นหาค่าตำแหน่งของรูใส่สกรูล็อคแกนตามกระดูกโดยใช้ภาพถ่ายรังสีแค่ 3 ภาพ หลักการที่ใช้ได้แก่ การจำลองสถานการณ์เพื่อนำมาวิเคราะห์ตำแหน่งและการเปลี่ยนแปลงของแกนตามกระดูกใช้จุดและการกำหนดตำแหน่ง และทิศทางของเครื่องมือการแพทย์ และอวัยวะภายในของคนไข้ โดยใช้การวิเคราะห์การเคลื่อนที่ทางจลน์ ทั้งนี้การพัฒนาระบบประมวลผลทางคณิตศาสตร์ จะถูกนำมาใช้เพื่อสร้างแนววิถีนำทางในการผ่าตัด

110 หน้า

## CONTENTS

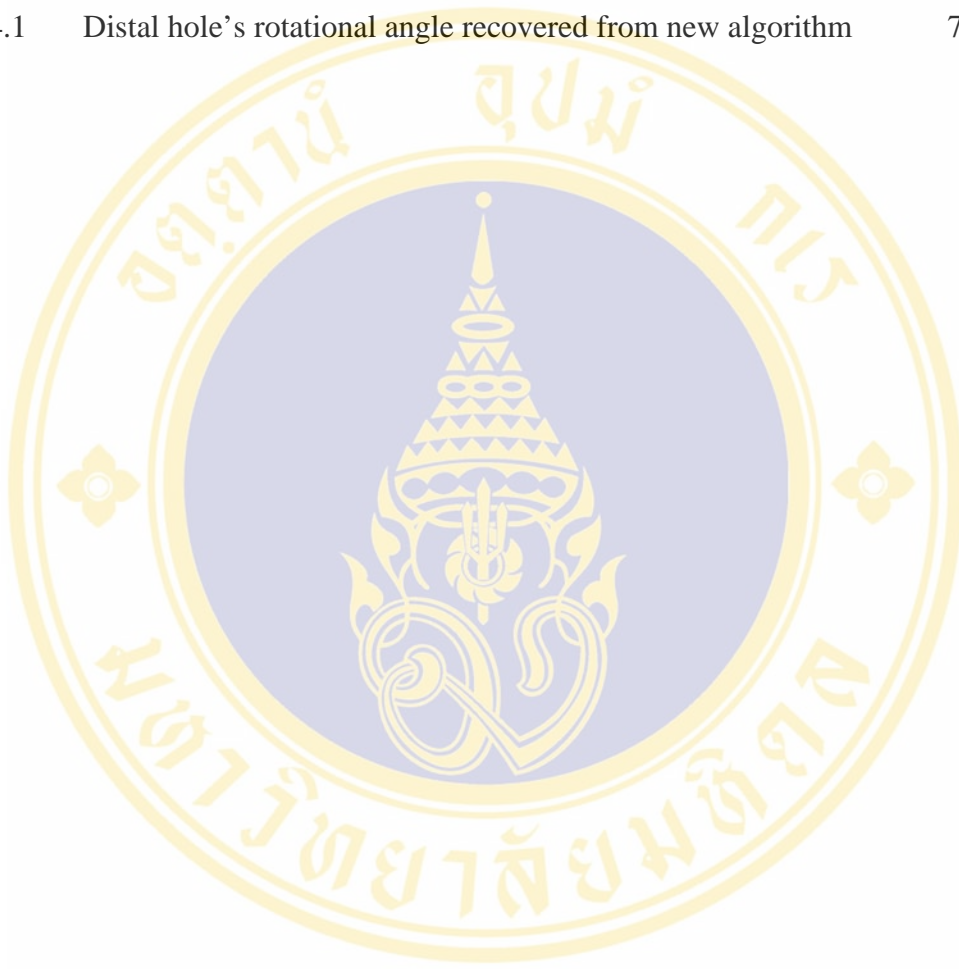
	<b>Page</b>
<b>ACKNOWLEDGEMENT</b>	<b>iii</b>
<b>ABSTRACT (ENGLISH)</b>	<b>iv</b>
<b>ABSTRACT (THAI)</b>	<b>v</b>
<b>LIST OF TABLES</b>	<b>viii</b>
<b>LIST OF FIGURES</b>	<b>ix</b>
<b>CHAPTER</b>	
<b>I INTRODUCTION</b>	<b>1</b>
1.1 Motivation/Background	1
1.2 Problem Statements	2
1.3 Objectives	5
1.4 Scope of Studies	5
<b>II LITERATURE REVIEWS</b>	<b>6</b>
2.1 Closed Intramedullary Nailing of Femur	6
2.2 Computer-Integrated Surgical System and Technology	10
2.3 Surgical Navigations and Algorithms in Orthopaedics Application	13
<b>III METHODS</b>	<b>20</b>
<b>Part I: Theoretical Reviews</b>	
3.1 Spatial Descriptions and Transformations	20
3.2 Related Image Processing Techniques	33
<b>Part II: Developed Methods</b>	
3.3 Overview methods of Fluoro-Navigation for Closed Intramedullary Nailing of Femur	44
3.4 Recovery of distal holes axis using X-Y span of distal hole's projection images	48

## CONTENTS (Continued)

	<b>Page</b>
3.5 Recovery of distal holes axis using interested area of distal hole's projection images	51
3.6 Recovery of distal holes axis using additional fiducial, Fluoroscope Tracking (FTRAC)	53
3.7 Chapter Summary	63
<b>IV EXPERIMENTAL RESULTS</b>	<b>64</b>
4.1 Recovery of Distal holes axis using X-Y span of distal hole's projection images	64
4.2 Recovery of distal holes axis using interested area of distal hole's projection images	68
4.3 Recovery of distal holes axis using additional fiducial, Fluoroscope Tracking (FTRAC.)	72
<b>V DISCUSSIONS</b>	<b>89</b>
5.1 Recovery of Distal holes axis using X-Y span of distal hole's projection images	89
5.2 Recovery of distal holes axis using interested area of distal hole's projection images	90
5.3 Recovery of distal holes axis using additional fiducial, Fluoroscope Tracking (FTRAC)	91
<b>VI CONCLUSION AND FUTURE WORKS</b>	<b>92</b>
<b>REFERENCES</b>	<b>94</b>
<b>APPENDIX</b>	<b>98</b>
<b>BIOGRAPHY</b>	<b>110</b>

## LIST OF TABLES

Table		Page
4.1	Distal hole's rotational angle recovered from new algorithm	71



## LIST OF FIGURES

FIGURE		Page
1.1	Intramedullary Closed Nailing of Femur.	2
1.2	IMN distal holes are shown at different angles of view. Top image shows the distal holes while their axes are perpendicular to the Fluoroscopic image plane, and Bottom image shows the distal holes at a rotated angle.	4
1.3	IMN diagram comparing images as seen from the optical stereoscopic (upper) and fluoroscopic (lower) systems.	4
1.4	Image depicts a full surgical navigation system in navigation research at Mahidol University.	4
1.5	Axes diagram.	5
2.1	The IMN was inserted into the femoral canal at the Trochanter of the femur bone which is far away from the broken area proposed by Kuntscher.	9
2.2	IMN with screws at both ends of the femur bone	10
2.3	The CIS architecture	12
2.4	CIS structure can be divided into three main parts	12
2.5	Experiment setup and the notation of projection images.	15
2.6	IMN distal hole orientation estimation procedures	19
3.1	The relationship between $\{A\}$ and $\{B\}$ in translation	24
3.2	The relationship between $\{A\}$ and $\{B\}$ in orientation	25
3.3	The general case of mapping.	26

## LIST OF FIGURES (Continued)

FIGURE		Page
3.4	The relationship between frame $\{A\}$ , $\{B\}$ and $\{C\}$	27
3.5	The relation of translation vectors	28
3.6	Represents rotations of the frame $\{B\}$ related to frame $\{A\}$	31
3.7	A mask for point detection	39
3.8	The masks for line detection	40
3.9	Illustration of basic morphological operations: a) Original set; b) Structuring element: square of side 3, reference pixel is at center; c) erosion; d) dilation; e) opening; f) closing.	43
3.10	Illustration of morphological <i>top-hat</i> transform.	44
3.11	The overview methods	45
3.12	X-ray images of an IMN in the difference of viewing from the C-arm.	45
3.13	IMN diagram comparing images as seen from the optical stereoscopic (upper) and fluoroscopic (lower) systems.	46
3.14	Distal hole axes.	47
3.15	Simulation of IMN rotations and all parameter's notation.	49
3.16	Diagram of the Propose Algorithm to Recover Intramedullary Nail's Distal Hole Axis	50
3.17	Simulation Rotation of the IMN about X-Axis	51
3.18	Overall of the algorithm using the area of the distal hole's projection images	52
3.19	The overview methods using the FTRAC	54

## LIST OF FIGURES (Continued)

FIGURE	Page
3.20 Data protocol for pose recovery of the FTRAC	54
3.21 FTRAC design	55
3.22 Flow chart of fiducial segmentation	56
3.23 Graph representation of edge image; a) Edge directions; b) corresponding graph.	58
3.24 Diagram of the Spatial Transformation	63
4.1 Simulation Results for Rotation about X	66
4.2 Simulation Results for Rotation about Y	66
4.3 Simulation Results for Rotation about X-Y	67
4.4 Simulation Results for Rotation about X-Y-Z	67
4.5 a) Fluoroscope (X-ray) imaging and b) taken by a digital camera	68
4.6 The experiment setup for this method	69
4.7 One data set of distal hole images at 0, 5, 10, 15 and 20 degrees	70
4.8 Tool Curve	70
4.9 C-arm models OCE 9600	72
4.10 Fiducial "FTRAC" which the diameter of 20 mm	73
4.11 Hauppauge WinTV USB, Frame grabber	73
4.12 Calibration Phantom made by Iulian, design by Gouthami	74
4.13 Lead Apron Radiation Protection and Thyroid Collar	75
4.14 The batch for measuring the x-ray exposure	75
4.15 Manual Rotary stage	76
4.16 FTRAC 20 mm on the Rotary Positioning stage	77
4.17 The x-ray images of FTRAC rotates about Y-axis	77

### LIST OF FIGURES (Continued)

<b>FIGURE</b>	<b>Page</b>
4.18 The x-ray images of FTRAC rotates about Z-axis	78
4.19 a) Calibration image before dewarping, b) Clean image before dewarping, c) Dewarped image	79
4.20 C-arm with Calibration phantom	79
4.21 Comparing the original image from C-arm and the dewarped Image	80
4.22 GUI for determining the FTRAC pose with respect to C-arm	81
4.23 GUI shows the residual error of the FTRAC	82
4.24 Experiment Setup	82
4.25 Connect the C-arm to the computer with the TV encoder	83
4.26 a) The TV encoder is connected to the PC monitor, which make less time for saving the images from C-arm b) the TV encoder is connected to the C-arm.	84
4.27 Diagram of rotating the C-arm during the experiment	84
4.28 A dataset of x-ray images in the difference viewing of the C-arm. The FTRAC and IMN are fixed without moving.	85
4.29 Acquiring the images and selecting the images from the C-arm	86
4.30 Dewarping the images	86
4.31 Segmentation of the FTRAC lines, points, and ellipses.	87
4.32 The pose of the FTRAC with respect to the C-arm in each view	87

# CHAPTER I

## INTRODUCTION

Medical navigation is gaining popularity in assisting surgeons in planning and guiding both in pre- and intra-operations. Medical navigation in orthopedic operations has been applied and developed for fifty years ago.

Numerous orthopedic operations require locating of implants and internal organs such as bone. Currently, standard procedures require x-ray exposure during the surgery to allow the surgeon to indicate the position and orientation of the patient's internal organs and medical inserting devices. An orthopedic operation, called "Closed Intramedullary Nailing of Femur (Closed Nailing)," is one of the frequent cases among orthopedic surgeries. This surgery also requires accurate positioning and orientating of the implant. One of the most difficult tasks for surgeons is to identify the position and orientation of the screwing holes (typically in circular shape) at both ends of the intramedullary nail (IMN) after being inserted into a patient's femoral canal. The distal hole locations may be shifted by external forces and torques applied to the IMN during the insertion procedure resulting in the IMN to deform.

### 1.1 Motivation/Background

Closed intramedullary femoral nailing is a minimally invasive surgery (MIS). In the conventional closed nailing surgery, surgeons require high experience, and a number of trial-and-error adjustments to correct the path for inserting the screws through those distal holes. Figure 1.1 illustrates the Closed Nailing of Femur. The process can be done by gradually adjusting the shooting angle until the projection of the two distal holes is seen as circular as possible on the x-ray image. Therefore, both surgeon and patient are continuously exposed to a great amount of x-ray exposure

from the fluoroscopic imaging system. This could harm the surgeon and patient for their long term health.



**Figure 1.1** Intramedullary Closed Nailing of Femur. [2]

## 1.2 Problem Statements

In a closed nailing surgery, one of the most difficult tasks for surgeons is to identify the position and orientation of the screwing holes (typically in circular shape) at both ends of the intramedullary nail after being inserted into a patient's femoral canal. This process called distal locking. The hole location may be shifted by external forces and torques applied to the IMN during the insertion procedure resulting in the IMN to deform. To recover the position and orientation (or "pose") of the screwing holes in the conventional operation, surgeons require high degree of experience, and a number of trial-and-error adjustments to correct the path for inserting the screws. This can be done by gradually adjusting the shooting angle until the projection of the two screwing holes is seen as circular as possible on the X-ray image. The concept of the proposed approach is to utilize a hybrid system of a fluoroscopic system and an optical stereoscopic system to quickly recover the screwing holes on the IMN, and to reduce the number of trial-and-error adjustments.

The operation starts after the surgeon inserts an IMN into the femur canal and sets the fractured bone into a desired position [2]. Two markers are attached to the patient in the location that can be seen from both fluoroscopic and optical stereoscopic imaging systems. The attaching procedure is done by attaching each marker directly to the distal and proximal part of the fractured bone through the skin (one marker for each position.)

Then, two X-ray images are taken by the fluoroscopic (C-Arm) system from different angles. The image processing and pattern recognition methods are used to generate (1) the frames attached to the markers, (2) the axis of the IMN and its perimeter, and (3) the screwing holes' location and orientation (pose) on the IMN. Note that in most cases, the shape of screwing holes viewed on X-ray images are in elliptical shape as shown in Figure 1.2, and a set of diagram comparing between images from optical stereoscopic and fluoroscopic is shown in Figure 1.3.

Simultaneously, the optical stereoscopic imaging system is capturing and generating the frames attaching to the same markers. A computer algorithm registers generated frames from both systems, thus, producing an insertion path which aids surgeon to navigate during the screw inserting procedure. Because the marker is fixed rigidly to the bone and visible on the optical stereoscopic images, the computer software uses this information to construct and track the insertion path, regardless of the patient's movement. Figure 1.4 illustrates the attached frames to the markers and holes, and the computed insertion path. During the screw insertion procedure, the proposed system requires only real-time images from the optical stereoscopic system which can be taken continuously and without risk of radiation exposure. The pre-registered insertion path generated from the algorithm is mapped onto the real-time optical images. The real-time images are shown in the monitors from two different views and angles so that the surgeon can use this guiding path to aid the surgical navigation.

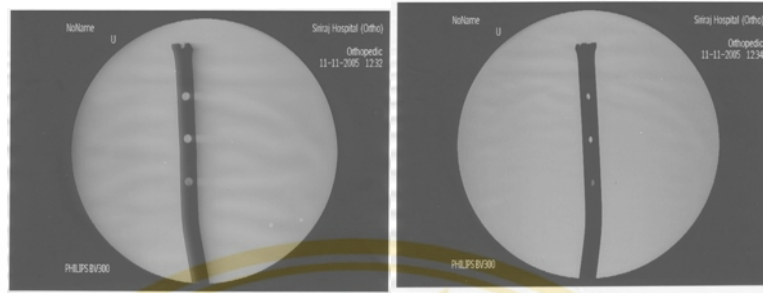


**Figure 1.2** IMN distal holes are shown at different angles of view. Top image shows the distal holes while their axes are perpendicular to the Fluoroscopic image plane, and Bottom image shows the distal holes at a rotated angle.

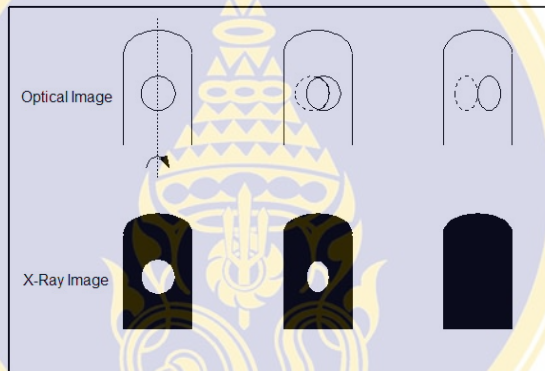


**Figure 1.3** IMN diagram comparing images as seen from the optical stereoscopic (upper) and fluoroscopic (lower) systems.

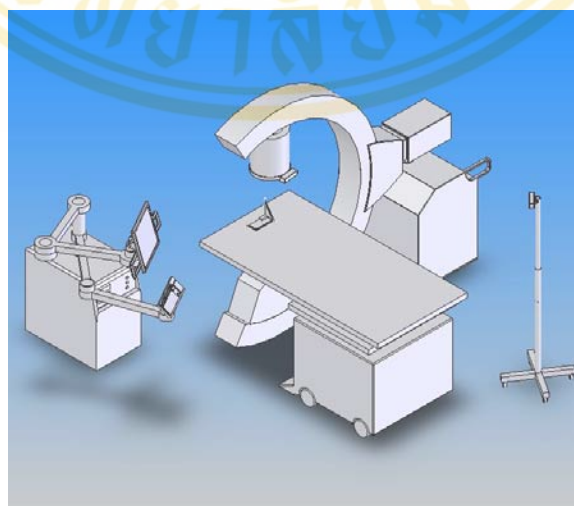


**Figure 1.4** Image depicts a full surgical navigation system in navigation research at Mahidol University.

### 1.3 Objectives

1.3.1 To investigate a new algorithm to recover the 3-D pose (position and orientation) of distal holes in the intramedullary nail by using no more than only four x-ray imaging projections.

1.3.2 To implement the recovering of IMN distal hole's orientation using a new algorithm.

### 1.4 Scope of Studies

Due to the complexity of current research problems, this project focuses on how to determine the axis of the IMN and IMN rotations about Axes X and Z (see axes diagram in Figure 1.5). Also, to further simplify the problem, it is assumed that the IMN translational movement is allowed in the X and Z directions, whereas the IMN rotational movement is allowed in the X and Z axes.

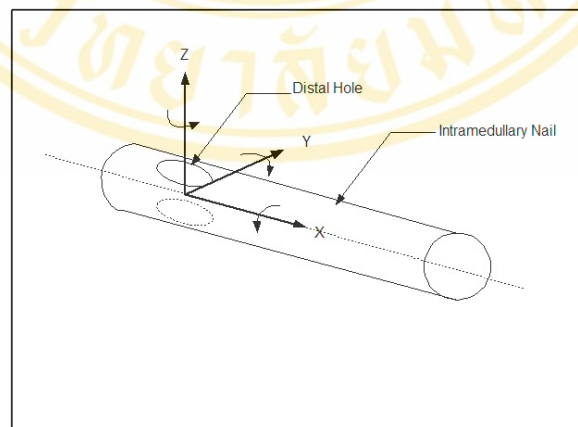


**Figure 1.5** Axes diagram.

In order to demonstrate the algorithm, a set of implementations will be done by using MATLAB in an experimental setup to simulate acquiring x-ray images.

## **CHAPTER II**

### **LITERATURE REVIEWS**

This chapter presents the relevant previous works, which can be divided into three main parts. There are “Closed Intramedullary Nailing of Femur,” “Computer-Integrated Surgical System and Technology,” “Surgical Navigations and Algorithms in Orthopaedics Application.”

2.1 Closed Intramedullary Nailing of Femur: this part will discuss about the background of the Closed Intramedullary Nailing of Femur and the method, surgeons use to find the distal holes pose.

2.2 Computer-Integrated Surgical System and Technology: in this part the overviews of the CIS system will be discussed.

2.3 Surgical Navigations and Algorithms in Orthopaedics Application: Navigations in orthopaedic surgery especially for the Closed Intramedullary Nailing will be discussed.

#### **2.1 Closed Intramedullary Nailing of Femur**

Orthopaedic Surgery with fixing bone fracture made giant strides forward fifty years ago [1]. It was developed from conservative treatment [2] to operative treatment. The bone fixation with operative treatment can be divided into two parts. There are internal fixation and external fixation. In this article, the internal fixation will be discussed only.

Basic modes of internal fixation can be divided into three: [2]

- Interfragmentary compression

- Splintage fixation
- Bridging fixation

Only Splintage and Bridging fixation involved with intramedullary nail. Splintage fixation allows the bone to move along fixing device such as “Intramedullary Nail”. Intramedullary Nail (IMN) has two main types, which are IMN without screw locking and with screw locking. Splintage fixation is suitable for a small number of pieces of bone fracture and will use IMN without screw locking. Bridging fixation is a method for fixing multiple pieces of bone fracture. Main fragment at top and bottom of bone fracture were fixed and IMN will pass through multiple pieces without fixation. The example of this method is the closed locked IMN. There are two locking methods of the screw which are dynamic locking and static locking.

In the past, many physicians try to do the experiment and research about methodology for orthopaedic surgery. The time line of internal bone fixation with using nail insertion method is as follows:

In 1841, a Prussian physician called “Dieffenbach” had done the nail insertion into broken bone canal. He used an elephant tusk as an IMN. This method was called “Dieffenbach’s operation” and was reported by Heine, which is a German physician in 1875. In 1880, Nicholas Senne used patient’s bone and made its shape look like a rod and inserted this bone into bone canal. He also started using steel rod to be the IMN. However, the steel rod was totally used by Nicolaysen. Most case of healing bone fracture with this steel rod was done in the femoral neck. In 1907, A Belgium physician called “Lambotte” started using screw locking and applied this technique in Clavicle fracture bone healing. In 1914, an England physician used knitting needle as an IMN and applied this device in femoral neck fracture healing. In the same year, Hey Groove found the problem of using steel rod as an IMN. This problem is biocompatibility of material. Steel rod is not suitable for human body because of the ferrous from the nail. In 1924, Lambotte used kirschner wire for fixing bone fracture and this technique was reported by Joly, who is a Belgium physician. In 1937, Rush brothers (L.V.Rush and H.L.Rush) reported a new technique with the use of Steinmann pin. They are the first group of physicians in America that were interested

in bone fixation with the use of IMN because this technique was accepted in Europe only. They had developed a device called “Rush pin”.

However, the most famous physician in this technique is Kuntscher, a German physician. Kuntscher successfully developed the bone fixation by closed nailing and his work was reported in 1940s. This is a big change in Orthopaedic surgery with IMN.

Orthopaedic surgery using IMN can be divided into two categories: opened nailing and closed nailing. Opened nailing is not complicated in the procedure of operation and requires a short time in operation. The disadvantage of opened nailing is the infection in the soft tissue because of contacting directly to the environment during the operation and the greater blood loss intra-operative and post-operative. While closed nailing is more complicated and required x – ray image from fluoroscope for guiding physicians during the operation. In the past, head-worn fluoroscope was used and that made a big trouble with x-ray exposure to physician. This method also requires long time of operation and high skill of physician. However, its result is better than opened nailing, less of infection and quicker in bone healing process.

An orthopaedic operation, called “Closed Intramedullary Nailing of Femur (Closed Nailing),” is one of the frequent cases among orthopaedic surgeries. This is a minimally invasive surgery (MIS) [1]. In 1940s, Kuntscher suggested the new method of the long bone fixing by inserted the IMN into the femoral canal at the Trochanter of the femur bone which is far away from the broken area as shown in Figure 1.1. The nail requires being locked by the screw at the distal or proximal part of the nail (Dynamic locking) or either both of them (Static locking) if there are many pieces of bone’s fractures as shown in Figure 1.2. This surgery also requires accurate positioning and orientating of the implant. One of the most difficult tasks for surgeons is to identify the position and orientation of the screwing holes (typically in circular shape) at both ends of the intramedullary nail (IMN) after being inserted into a patient’s femoral canal [3]. The distal hole locations may be shifted by external forces and torques applied to the IMN during the insertion procedure resulting in the

IMN to deform. In the conventional closed nailing surgery, surgeons require high experience, and a number of trial-and-error adjustments to correct the path for inserting the screws through those distal holes. The process can be done by gradually adjusting the shooting angle until the projection of the two distal holes is seen as circular as possible on the x-ray image. Therefore, both surgeon and patient are continuously exposed to a great amount of x-ray exposure from the fluoroscopic imaging system. This could harm the surgeon and patient for their long term health.



**Figure 2.1** The IMN was inserted into the femoral canal at the Trochanter of the femur bone which is far away from the broken area proposed by Kuntscher.  
[www.ispub.com]

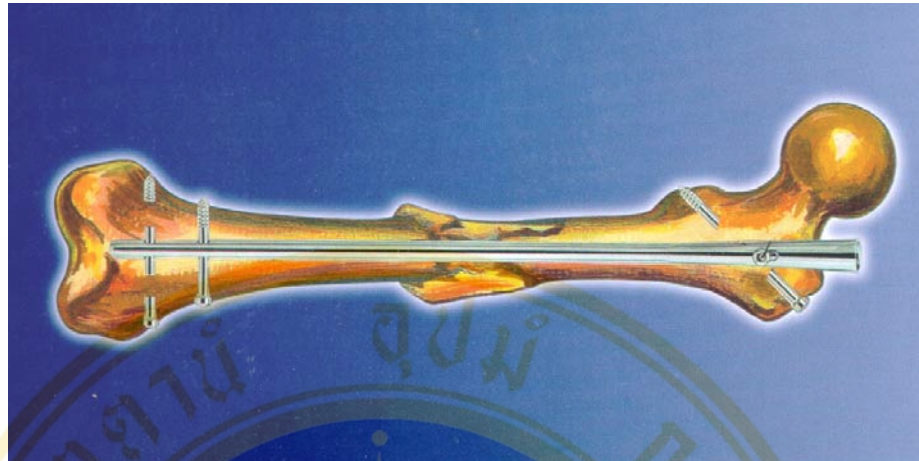


**Figure 2.2** IMN with screws at both ends of the femur bone [2]

## 2.2 Computer-Integrated Surgical System and Technology

This topic focuses on Computer-Integrated Surgical techniques, system, and applications exploiting quantitative information from medical images and sensors to assist physicians in all phases of treatment. Computer-Integrated Surgical (CIS) System and Technology is gaining popularity and can help surgeons solve the problems above. CIS becomes a main system and involves with all the processes of the operation, analysis to preoperative planning, implementation, and follow-up. It emphasizes the relationship between problem definitions, computer-based technology. The CIS's architecture and structure [4] are as shown in Figure 2.3 and Figure 2.4. Figure 2.3 shows the key system elements and interfaces of CIS system. The main system of CIS is a computer or network of computers running a variety of modeling and analysis processes, including image and sensor processing, creation and manipulation of patient-specific anatomical models, surgical planning, visualization, monitoring and control of surgical processes. These processes receive information about the patient from medical imaging devices about the patient and may directly act on the patient through the use of specialized robots or other therapy devices controlled by the computer. They also communicate with the surgeon through a variety of visualization subsystems, haptic devices, or other human-machine interfaces. The

surgeon remains in overall control of the procedure and, indeed, may do all of the actual manipulation of the patient using hand tools with information and decision support from the computer. The modeling and analysis processes within the computer will often rely upon databases of a priori information, such as anatomical atlases implanted device design data, or descriptions of common surgical tasks or sub-tasks. The computer also has the ability to retain essentially all information developed during surgical planning and execution and store it for post-operative analysis and comparison with long term outcomes.

Devices and techniques to provide the interfaces between the “virtual reality” of computer models and surgical plans to the “actual reality” of the operating room, patients, and surgeons are essential elements of CIS. The interface technology may be divided into three inter-related categories. First is the Imaging techniques and sensory devices, second is the Robotic devices and systems, and the third is Human-machine interfaces. Figure 2.4 shows that CIS can be divided into three main parts. There are preoperative phase, intra-operative phase and postoperative phase. First is Preoperative phase, this phase is related with surgical planning and collecting data from patient. In this step the surgeon will receive the anatomical information of patients. These information usually come from Image which is taken by Computer Tomography (CT), Magnetic Resonance Imaging (MRI) and Fluoroscope (C-Arm). Planning process requires the simulation of 3-D image from 2-D image and also computational surgical path planning. Second is the Intra-operative phase, the information from the first part will be used in this part. The information from the first step will be registered to the patient and based on information from various sensors that are attached in the system. The computer then uses a variety of interface devices to assist the surgeon in execution of the surgical plan. The last is the Postoperative phase; the information from preoperative and intra-operative phase will be combined together. This step is to verify the results of the procedure. The results of many procedures may be registered back to an anatomical atlas to facilitate statistical studies relating surgical technique to clinical outcomes.

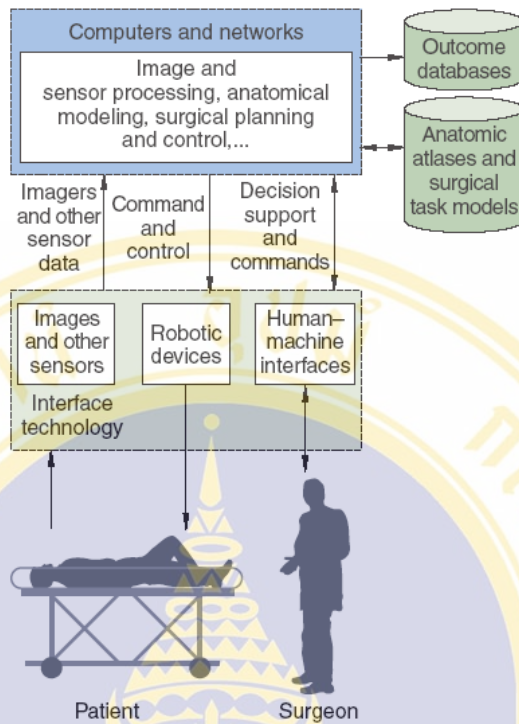


**Figure 2.3** The CIS architecture [5]

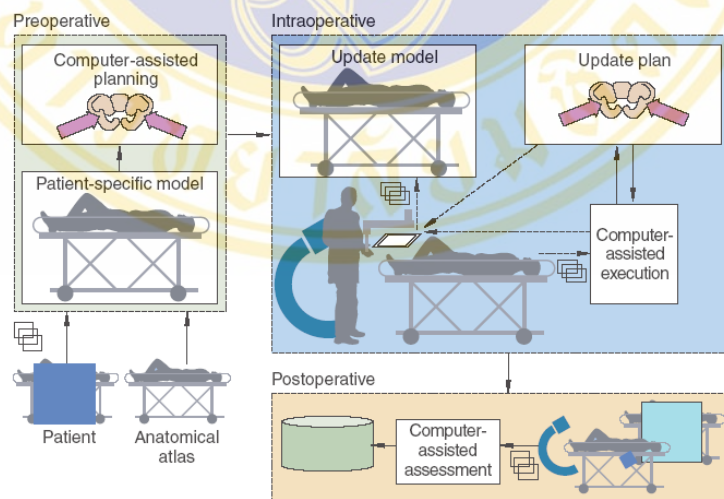


**Figure 2.4** CIS structure can be divided into three main parts [5]

CIS was applied in many tasks of orthopaedic surgery. Most are focused primarily on allowing the surgeon to better perform a difficult or inherently

inaccurate aspect of a surgical procedure [6]. The Imaging techniques and sensory devices require imaging method and proximal sensor to progress the information of patients as available from the preoperative and intraoperative phase. This part is the model-based vision. The problems in the model-based vision are the estimation of the position and orientation (pose) of a 3D object (sensors, fiducial markers or patient's bone) with respect to the 2D images [7]. The Robotic devices and systems require extremely high accuracy of the robot and imaging system for the task. The safety for both patient and surgeon is the main concern for any surgical robotic system and the system must be able to be made sterile, so the design of the devices must concern with the user's skill [6]. Human-machine interfaces require advanced algorithm and technology. This part is very sensitive for both surgeon and patient in term of sensing. Surgeons require sensing from the patient, called force feedback from touching to patients. These require haptic interfaces and superimposed visual displays.

CIS is applied to many applications in orthopaedic surgery and one of the frequent cases of Orthopaedic surgeries is Closed intramedullary Nailing of Femur, which is a minimal invasive surgery. CIS is applied to minimize complexity of the MIS. [8-14]

### **2.3 Surgical Navigations and Algorithms in Orthopaedics Application**

Navigation is applied in various applications and also in surgical system. Surgical navigations and algorithms in Orthopaedics application is gaining popularity and becomes a major part in the CIS technology. This topic presents previous works on Orthopaedic navigations system, especially, in operation called 'Closed Intramedullary Nailing of Femur.'

Yaniv and his research group from Israel is a current active group conducting research on the similar problem of Closed Nailing Navigation [15]. Yaniv identifies distal hole location using image processing. Surgeon needs to rotate the C-arm randomly until the distal hole appears in the x-ray image then calculate the hole position by rotate the C-arm in known position. Common C-Arm has no tracking

sensor to trace its motion. The drill guide performed by detecting the circular fiducials in the image and then the correct correspondence with their 3D model. Hough transform was applied in this procedure. Correctly pairing the detected fiducials and the 3D model fiducials is difficult. They use the geometry of the drill guide target: they use lines instead of points, since lines are less sensitive to partial occlusions. For nail hole identification, Model-based approach was applied. This uses only edge elements which belong to the convex hull of the set of elements. The drill guide pose is computed by non-linear minimization of the projection distances between the known fiducial projection coordinates and the expected ones as shown in Equation 2.1

$$\mathbf{v}^* = \arg \min_{\mathbf{v}} 0.5 \left( \sum_{i=1}^n (x_i - \hat{x}_i(\mathbf{v}))^2 + (y_i - \hat{y}_i(\mathbf{v}))^2 \right) \quad (2.1)$$

$$\mathbf{t} = \begin{bmatrix} \frac{z}{f} \mathbf{P}_x \\ \frac{z}{f} \mathbf{P}_y \\ z \end{bmatrix} \quad R = \begin{bmatrix} \mathbf{P}_x - \mathbf{Q}_x & \mathbf{P}_y - \mathbf{Q}_y & 0 \\ \mathbf{P}_y - \mathbf{Q}_y & \mathbf{Q}_x - \mathbf{P}_x & 0 \\ 0 & 0 & -1 \end{bmatrix}$$

Where the  $\mathbf{v}$  = rigid body transformation parameterization.

$(p_x, p_y)$  and  $(q_x, q_y)$  are the coordinates of the nail hole in the image.

$d_{in}$  = the average diameter of the image

$d$  = the real diameter of the image.

$f$  = camera focal length.

$t$  = Nail's locations

$R$  = Nail's orientation relative to the camera.

The experiment setup is shown in Figure 2.5.

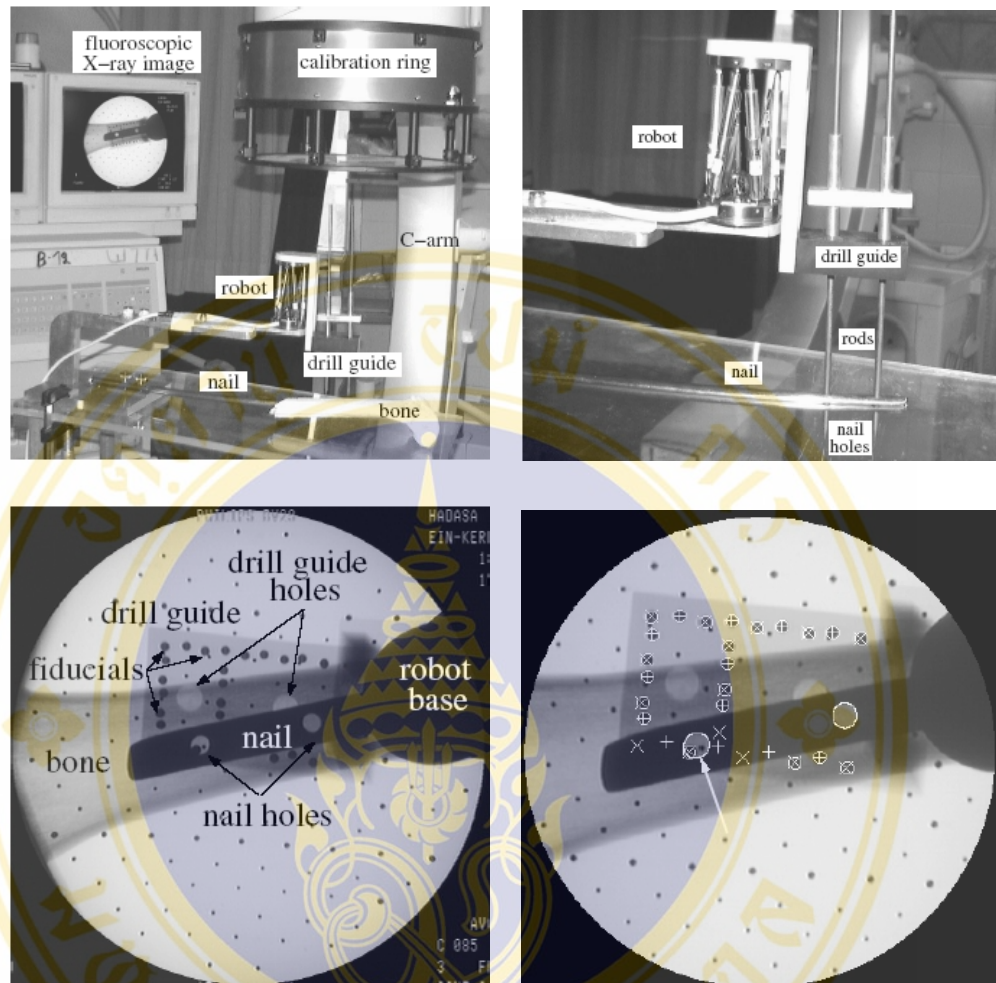


**Figure 2.5** Experiment setup and the notation of projection images.

This is an in vitro experiment. They try two approaches, one is the interactive approach, the x-ray technician aligns the viewing axis of the C-arm and nail hole in a fronto-parallel set up using image based guidance. The second is estimation of the nail pose from a single image of the nail holes. The better result is the interactive approach which results in a mean angular error of  $1.3^\circ$  (std =  $0.4^\circ$ ) between drill guide axes, and a mean 3.0mm error (std = 1.1mm.) Yaniv., finally continues implementation on MARS. More details can be found in [11, 14].

Other similar research by Wang *et al.* [16] proposed a new method by using a fluoroscopy-guided robot navigating system for distal locking of IMN which needs only two x-ray projection images from lateral and AP views. The study shows determination of positioning point for robot navigation by using two x-ray projection

images from lateral and AP views. The robot BPOR (Biplanar Orthopaedic Robot) is applied for implementing all navigating motions during the surgical procedure. In navigating phase, the base of BPOR robot is connected with fracture leg of patient via a foot-holder. At the same time the slight motion of patient's limb makes no efforts to the accuracy.

Several other approaches to present approaches on solving distal locking problems are carried on. Zheng et al. [17, 18] introduces optimal and robust approach based on two calibrated and registered fluoroscopic images using iteration fitting a cylindrical model to the x-ray images and estimate the distal hole axis. Then use the Iteration fitting geometrical models of the distal locking holes (DLHs) to the images. Hough transform is used to extract the feature points from the image. Canny Edge detection is also used to detect the parallel line of the nail. Geometrical Models are a combination of an inner cylinder model and two cone trapezoid openings, which are used later to simulate X-ray projection of the DLH model. They also set up a constraint to make it easy by assuming the femoral patient shaft should be roughly parallel to the image intensifier.

Prior to carrying out image processing, fluoroscopic image calibration may be required in most approaches. [19] shows how to automatically calibrate the Fluoroscopic views and determine the data from two images to build the 3D of the nail distal part. In the conventional way, calibration is one of the most concerning during the operation because it takes time and need to be very accurately. Tracking system is applied in this method. They fix the marker which has three spherical balls on its. This marker is a rigid body. Attach the marker to the proximal part of the nail and another one is fixed to the calibration plate. After inserting the nail, this method requires two x-ray images of the distal part of the nail. And both images need to be at least showing some part of the distal holes. Only the objects having a circular shape are conserved. C-arm position, are determined by the previous transformation. Determine the nail contour; Image processing becomes the main role in this procedure. Segmentation, threshold and labeling are applied. Projection cones of the two projection's nail. Construct the 3D nail model and the locking holes from the intersection of the two projection cones of the nail. During targeting, the marker is attached to the drilling tool. Display the nail and the drill models in real time on a

same view are required. The result shows the precision of the fluoroscopic image correction to be measured using the known positions of several calls of the calibration plate.

Yaniv and Joskowicz [20] also present a new on-line automatic x-ray fluoroscopic C-arm calibration method for intra-operative use. Their method utilizes a custom-designed calibration ring with a two-plane pattern of fiducials that attaches to the C-arm image intensifier, and an on-line calibration algorithm. The three steps of calibration algorithm compute the calibration parameter from a single x-ray image and from a spatial model of the fiducial centers. First it locates the fiducials and their patterns (U-shaped) and matches them to the model. It then computes the distortion correction and the calibration parameters.

Fichtinger and his co-workers introduced their concept on C-Arm calibration [21, 22]. This paper talks about the calibration of C-arm which may not be necessary. The study showed the error of the calibration which did not affect the result of the projection image. The result followed from the FTRAC and the virtual fluoroscopy. They prove in theory and demonstrate experimentally that intra-operative dosimetry of brachytherapy implants is feasible with an un-calibrated C-arm. They focus on the focal spot only (3 parameters). So, They fix the pixel sizes to be the constant values. Model for Reconstruction Space Transformation is described. They set up two frames which are A and B. The assumptions are: 1)  ${}^I F_A, {}^I F_B$  can be computed from the images; 2) A&B are not large in comparison to the focal length; 3)  $F_A$  and  $F_B$  are close by; 4) The quantity of interest is  ${}^A F_B = ({}^I F_A)^{-1} {}^I F_B$ . They claim that the simplest transformation will be a linear affine model.

Alternatively, Eyke et al. [23] discusses on virtual fluoroscopy. A new concept for a computer-assisted freehand navigation system that uses single intra-operatively acquired fluoroscopic images as a basis for real-time navigation of surgical tools. Optoelectronic markers are placed on surgical tools, a patient reference, and the fluoroscope to track their positions in space. Projection properties of the fluoroscope are acquired through an initial precalibration procedure using a tracked radiopaque phantom grid. Corrections are applied to compensate for both the fluoroscope's image intensifier distortions and the mechanical bending of the C-arm frame. This enables

real-time simulation of surgical tool positions simultaneously in several single-shot fluoroscopic images.

Hofstetter [24] introduces freehand navigation concept. A new concept for a computer-assisted freehand navigation system that uses single intra-operatively acquired fluoroscopic images as a basis for real-time navigation of surgical tools. Optoelectronic markers are placed on surgical tools, a patient reference, and the fluoroscope to track their positions in space. Projection properties of the fluoroscope are acquired through an initial precalibration procedure using a tracked radiopaque phantom grid. Corrections are applied to compensate for both the fluoroscope's image intensifier distortions and the mechanical bending of the C-arm frame. This enables real-time simulation of surgical tool positions simultaneously in several single-shot fluoroscopic images.

C. Neatpisarnvanit and J. Suthakorn [27] propose a new method, which is based entirely on the geometry of the IMN. It requires that the IMN outer diameter,  $dN$ , and IMN distal hole's diameter,  $dH$ , are known in order to properly estimate the IMN distal axis's orientation (or the ratio of  $dH/dN$ ). Based on this information, the distal hole axis (angle) can be estimated by measuring the opening size of the distal hole and IMN outer diameter from the fluoroscopic image. Image processing is applied to this work which is Thresholding, Sobel edge detection, Morphological, Hough Transform, and Blob analysis algorithm. Figure 2.6 shows the estimation procedure of IMN distal hole orientation.

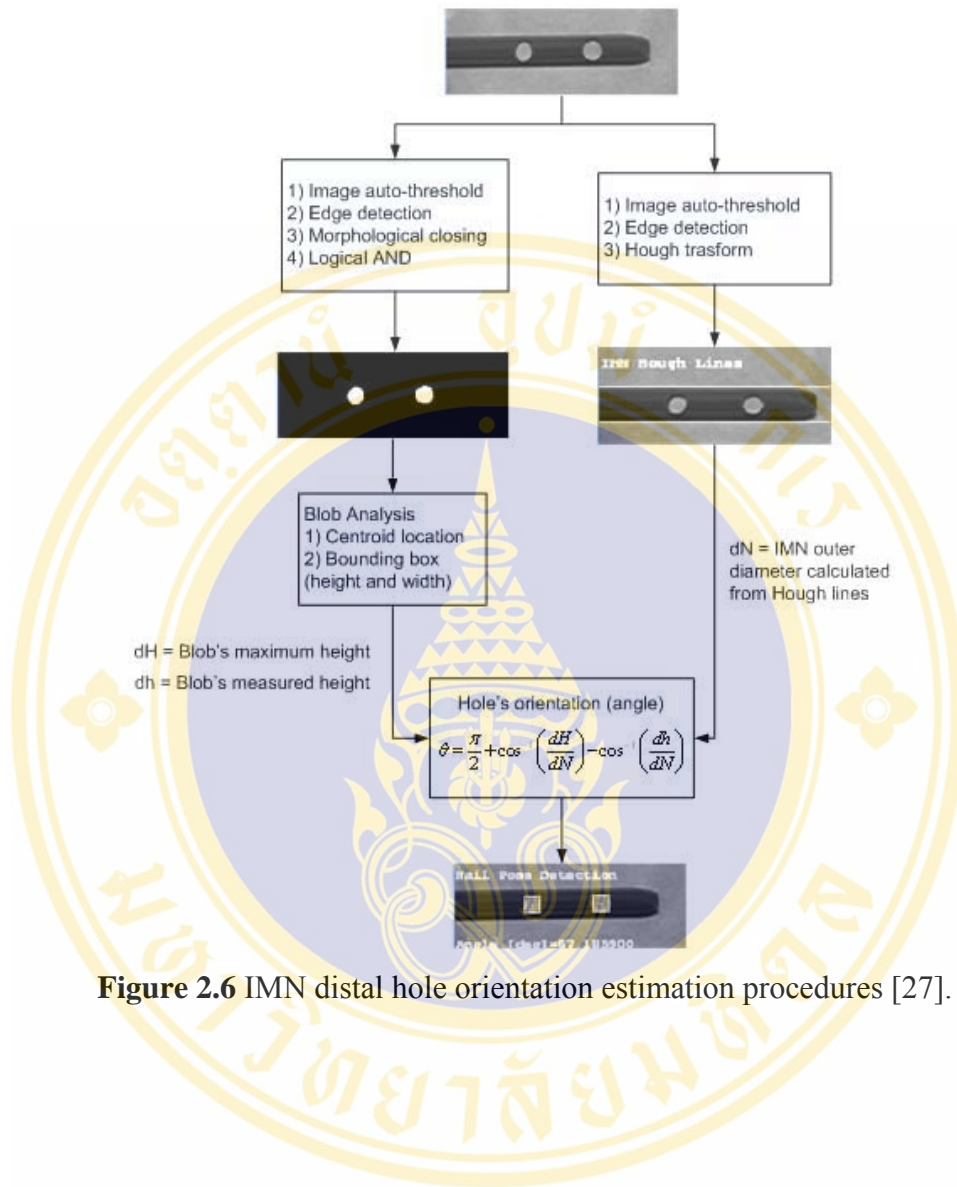


**Figure 2.6** IMN distal hole orientation estimation procedures [27].

## CHAPTER III

### METHODS

This chapter is divided into two main parts. Part I includes Theoretical reviews on Spatial Descriptions and Transformations, and Related Image Processing Techniques. Spatial descriptions and transformations include the descriptions of a position, an orientation, and a frame. Mappings, Operators, and Euler angles are included in this subsection. Mappings include mapping involving translated frames, mapping involving rotated frames, and mapping involving general frames. Operators include Translational operators, Rotational operators, and Transformation operators. Euler angles in Z-Y-X and Z-Y-Z are presented in this subsection as well. Subsection, Related Image Processing Techniques, includes Image registration, Image segmentation. Part II includes novel methods developed in this thesis research. The developed methods are: 1) Overview methods of Fluoro-Navigation for Closed Intramedullary Nailing of femur, 2) Recovery of distal holes axis using X-Y span of distal hole's projection images, 3) Recovery of distal holes axis using interested area of distal hole's projection images, and 4) Recovery of distal holes axis using additional fiducial, Fluoroscope tracking (FTRAC.)

#### **Part I: Theoretical Reviews**

### **3.1 Spatial Descriptions and Transformations**

#### **3.1.1 Introduction**

This subsection presents the descriptions of a position, an orientation, and a frame, and all these three parameters are involved and mainly used in the present works. All positions, orientations are described with respect to the universe coordinate system or with respect to other Cartesian coordinate systems which are defined

relative to the universe system. A universe coordinate system is used as a reference for everything discussed in this section.

### 3.1.2 Description of a Position

A position of any points in a coordinate system is represented with a 3 x 1 vector, called “position vector.” Many coordinate systems are defined with respect to a universe coordinate system; vectors must be tagged with information identifying which coordinate system they are defined within. The vectors are written with a leading superscript indicating the coordinate system to which they are referenced (unless it is clear from context), for example is  ${}^A P$ . This means that the components of  ${}^A P$  have numerical values which indicate distances along the axes of the coordinate system  $\{A\}$ . Each of these distances along an axis can be thought of as the result of projecting the vector onto the corresponding axis. The components of a vector are given subscripts x, y, and z [30]:

$${}^A P = \begin{bmatrix} p_x \\ p_y \\ p_z \end{bmatrix} \quad (3.1)$$

### 3.1.3 Description of an Orientation

To represent a complete location of a point in space, the orientation is needed. Thus, positions of points are described with an attached coordinate system to the point and then give a description of this coordinate system to the reference system. The coordinate system  $\{A\}$  is compared to the coordinate system  $\{B\}$  with known direction. The relation between these two coordinate systems is required to give the orientation. The unit vectors giving the principal directions of coordinate system  $\{B\}$  as  $\hat{X}_B, \hat{Y}_B,$  and  $\hat{Z}_B$ . When written in terms of coordinate system  $\{A\}$  they are called  ${}^A \hat{X}_B, {}^A \hat{Y}_B,$

and  ${}^A\hat{Z}_B$ . These three unit vectors are represented in 3 x 3 matrix, which called a “rotational matrix.” The notation of rotation matrix describes  $\{B\}$  relative to  $\{A\}$ . The rotation matrix of  $\{B\}$  relative to  $\{A\}$  can be written as:

$${}^A_B R = \begin{bmatrix} {}^A\hat{X}_B & {}^A\hat{Y}_B & {}^A\hat{Z}_B \end{bmatrix} = \begin{bmatrix} r_{11} & r_{12} & r_{13} \\ r_{21} & r_{22} & r_{23} \\ r_{31} & r_{32} & r_{33} \end{bmatrix} \quad (3.2)$$

Each component of  ${}^A_B R$  in (3.2) can be written as the dot product of a pair of unit vectors as:

$${}^A_B R = \begin{bmatrix} {}^A\hat{X}_B & {}^A\hat{Y}_B & {}^A\hat{Z}_B \end{bmatrix} = \begin{bmatrix} \hat{X}_B \cdot \hat{X}_A & \hat{Y}_B \cdot \hat{X}_A & \hat{Z}_B \cdot \hat{X}_A \\ \hat{X}_B \cdot \hat{Y}_A & \hat{Y}_B \cdot \hat{Y}_A & \hat{Z}_B \cdot \hat{Y}_A \\ \hat{X}_B \cdot \hat{Z}_A & \hat{Y}_B \cdot \hat{Z}_A & \hat{Z}_B \cdot \hat{Z}_A \end{bmatrix} \quad (3.3)$$

Since the dot product of two unit vectors yields the cosine of the angle between them, it is clear why the components of rotation matrices are often referred to as *direction cosines*. Further inspection of (3.3) shows that the rows of the matrix are unit vectors of  $\{A\}$  expressed in  $\{B\}$ ; that is,

$${}^A_B R = \begin{bmatrix} {}^A\hat{X}_B & {}^A\hat{Y}_B & {}^A\hat{Z}_B \end{bmatrix} = \begin{bmatrix} {}^B X_A^T \\ {}^B Y_A^T \\ {}^B Z_A^T \end{bmatrix} \quad (3.4)$$

Therefore,  ${}^A_B R$ , the description of frame  $\{A\}$  relative to  $\{B\}$  is given by the transpose of (3.3); which is,

$${}^A_B R = {}^A_B R^T \quad (3.5)$$

Equation (3.5), suggests that the inverse of a rotation matrix is equal to its transpose.

This can be verified by:

$${}^A R_B^T {}^A R_B = \begin{bmatrix} {}^A \hat{X}_B^T \\ {}^A \hat{Y}_B^T \\ {}^A \hat{Z}_B^T \end{bmatrix} \begin{bmatrix} {}^A \hat{X}_B & {}^A \hat{Y}_B & {}^A \hat{Z}_B \end{bmatrix} = I_3, \quad (3.6)$$

where  $I_3$  is the 3 x 3 identity matrix. The conclusion from (3.5) and (3.6) become:

$${}^A R_B = {}^A R_B^T = {}^B R_A^{-1} \quad (3.7)$$

### 3.1.4 Description of a Frame

To completely specify the location of a point, a position and orientation information is needed. Frame is a coordinate system, which is a set of four vectors giving position and orientation information:

$$\{B\} = \left\{ {}^A R_B \quad {}^A P_{BORG} \right\} \quad (3.8)$$

where  ${}^A P_{BORG}$  is the vector which locates the origin of the frame  $\{B\}$  relative to  $\{A\}$ .

### 3.1.5 Mapping involving translated frames

Mappings involve translated frames. Figure 3.1 shows the relation between  $\{A\}$  and  $\{B\}$ . In this case,  $\{B\}$  differs from  $\{A\}$  only by a translation which is given by  ${}^A P_{BORG}$ . To find the point P relative to  $\{A\}$ ,  ${}^A P$  by vector addition:

$${}^A P = {}^B P + {}^A P_{BORG} \quad (3.9)$$



Figure 3.1 The relationship between {A} and {B} in translation. [30]

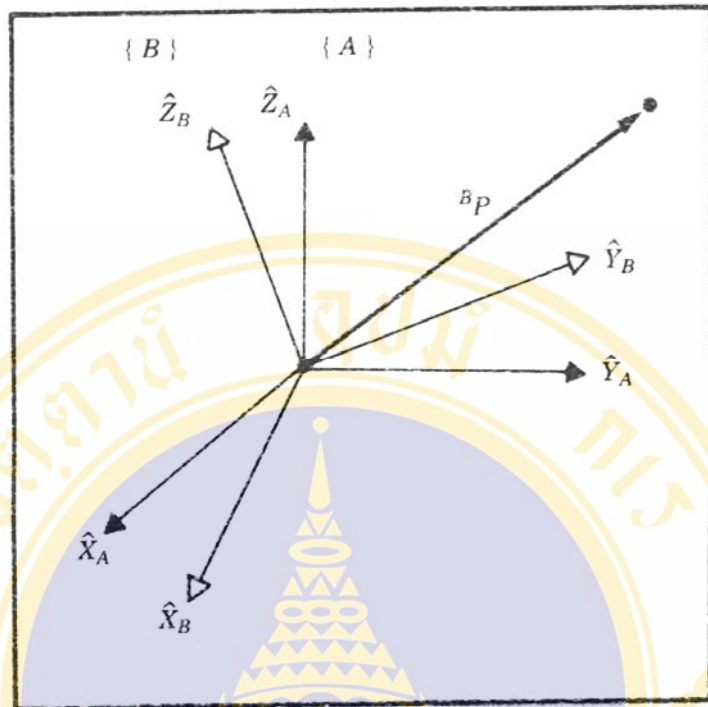
### 3.1.6 Mapping involving rotated frames

Figure 3.2 shows the relation between {A} and {B}. In this case, {B} differs from {A} only by a rotation which is given by  ${}^A_B R$  and the consequence of this is shown below:

$${}^A_B R = {}^B_A R^{-1} = {}^B_A R^T \tag{3.10}$$

Note that by the definition, the columns of a rotation matrix all have unit magnitude, and further, these unit vectors are orthogonal. So a rotation matrix can be interpreted as a set of three column's vectors or as a set of three row vectors as follows:

$${}^A_B R = \begin{bmatrix} {}^A \hat{X}_B & {}^A \hat{Y}_B & {}^A \hat{Z}_B \end{bmatrix} = \begin{bmatrix} {}^B \hat{X}_A^T \\ {}^B \hat{Y}_A^T \\ {}^B \hat{Z}_A^T \end{bmatrix} \tag{3.11}$$



**Figure 3.2** The relationship between  $\{A\}$  and  $\{B\}$  in orientation [30]

### 3.1.7 Mapping involving general frame

Figure 3.3, the general case of mapping mostly involved with both translation and rotation. The equation (3.12) describes a general transformation mapping of a vector from its description in one frame to a description in a second frame.

$${}^A P = {}^A R^B P + {}^A P_{BORG} \quad (3.12)$$

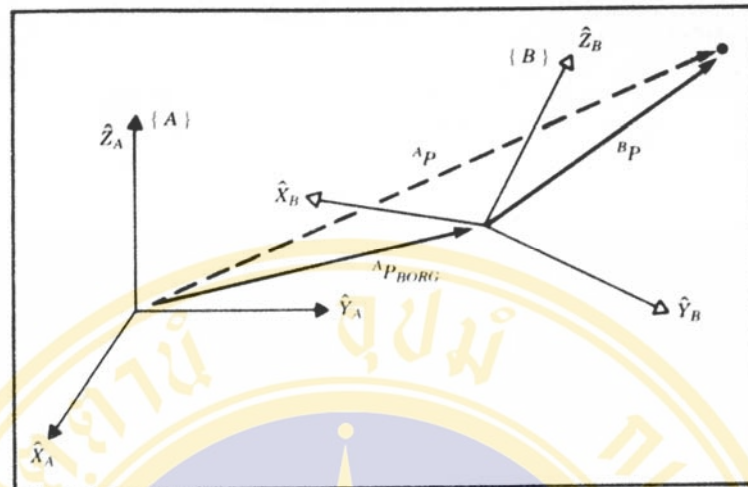


**Figure 3.3** The general case of mapping. [30]

The form of equation is not as appealing as the conceptual form,

$${}^A P = {}^A T_B {}^B P \tag{3.13}$$

Where  ${}^A T_B$  is called a Homogeneous Transform.

Homogeneous Transform defines a 4 x 4 matrix operator, and use 4 x 1 position vectors, so that the structure becomes:

$$\begin{bmatrix} {}^A P \\ 1 \end{bmatrix} = \begin{bmatrix} {}^A R_B & {}^A P_{BORG} \\ 0 & 0 & 0 & 1 \end{bmatrix} \begin{bmatrix} {}^B P \\ 1 \end{bmatrix} \tag{3.14}$$

That is,

1. A “1” is added as the last element of the 4 x 1 vectors.
2. A row “[0 0 0 1]” is added as the last row of the 4 x 4 matrix.

From Figure 3.4, one has  ${}^C P$  and wishes to find  ${}^A P$ . Combining the transformation of  ${}^C P$  into  ${}^B P$  and  ${}^B P$  into  ${}^A P$  :

$${}^A P = {}^A T_B {}^B T_C {}^C P \tag{3.15}$$

$${}^A T_C = {}^A T_B {}^B T_C \tag{3.16}$$

$${}^A T_C = \begin{bmatrix} {}^A R_B {}^B R_C R & {}^A R_B {}^B P_{CORG} + {}^A P_{BORG} \\ 0 & 0 & 0 & 1 \end{bmatrix} \tag{3.17}$$

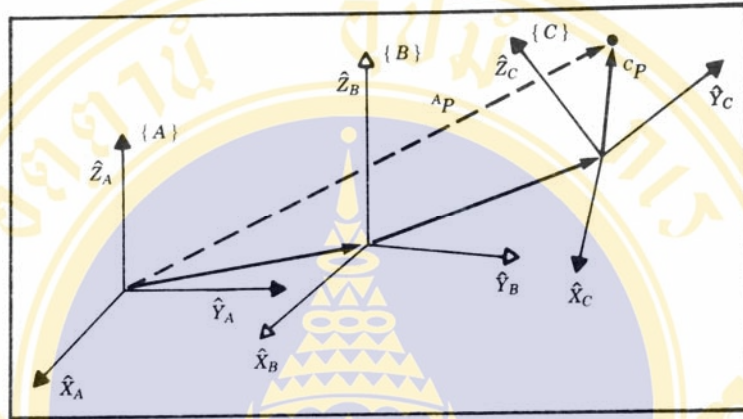


**Figure 3.4** The relationship between frame {A}, {B} and {C}. [30]

A straightforward way of calculating the inverse is to compute the inverse of the 4 x 4 homogeneous transform. To find  ${}^A T_B$  one must compute  ${}^B R_A$  and  ${}^B P_{AORG}$  from  ${}^A R_B$  and  ${}^A P_{BORG}$ .

$${}^B R_A = {}^A R_B^T \tag{3.18}$$

$${}^B ({}^A P_{BORG}) = {}^B R_A {}^A P_{BORG} + {}^B P_{AORG} \tag{3.19}$$

$${}^B P_{AORG} = -{}^B R_A {}^A P_{BORG} = -{}^A R_B^T {}^A P_{BORG} \tag{3.20}$$

$${}^B T_A = \begin{bmatrix} {}^B R_A & -{}^B R_A {}^A P_{BORG} \\ 0 & 0 & 0 & 1 \end{bmatrix} \tag{3.21}$$

Note that in the notation used:

$${}^B_A T = {}^A_B T^{-1} \quad (3.22)$$

### 3.1.8 Translational operators

The operators in mathematical forms which are used in the present works to map points between frames can be interpreted as operators which translate points, rotate vectors, or both. This section illustrates the operators applied in this works.

When a vector is moved “forward” relative to a frame, one may consider either that the vector moved “forward” or that the frame moved “backward.” The mathematics involved in the two cases is identical, only the view of the situation is different. Figure 3.5 indicates pictorially how a vector  ${}^A P_1$  is translated by a vector  ${}^A Q$ . Here the vector  ${}^A Q$  gives the information needed to perform the translation.  ${}^A P_2$  is the result of the operation between  ${}^A P_1$  and  ${}^A Q$ . The calculation of the operation is shown in equation (3.23)

$${}^A P_2 = {}^A P_1 + {}^A Q. \quad (3.23)$$

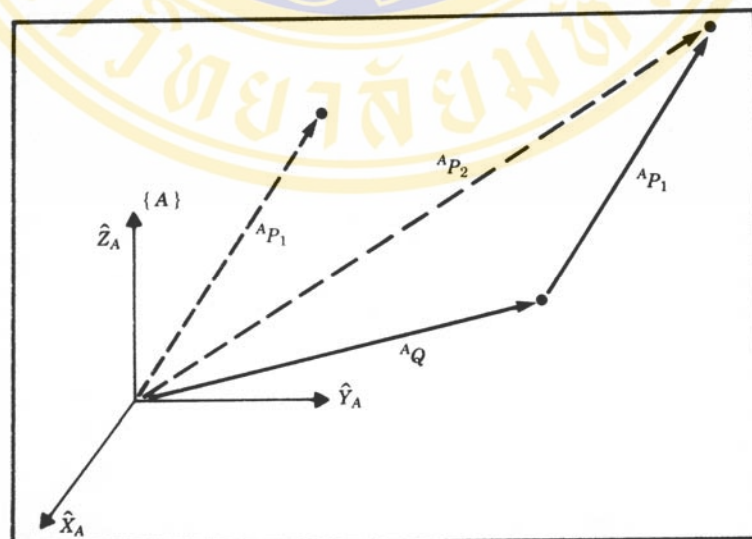


**Figure 3.5** The relation of translation vectors [30]

To write this translation operation as a matrix operator, one uses the notation

$${}^A P_2 = D_Q(q) {}^A P_1 \quad (3.24)$$

where  $q$  is the signed magnitude of the translation along the vector direction  $\hat{Q}$ .

The  $D_Q$  operator may be thought of as a homogeneous transform of the special simple form:

$$D_Q(q) = \begin{bmatrix} 1 & 0 & 0 & q_x \\ 0 & 1 & 0 & q_y \\ 0 & 0 & 1 & q_z \\ 0 & 0 & 0 & 1 \end{bmatrix} \quad (3.25)$$

where  $q_x, q_y, q_z$  are the components of the translation vector  $Q$  and

$$q = \sqrt{q_x^2 + q_y^2 + q_z^2}$$

### 3.1.9 Rotational operators

A rotational operator operates on a vector  ${}^A P_1$  and changes that vector to a new vector which is  ${}^A P_2$ . This equation is written in equation (3.26.)

$${}^A P_2 = R {}^A P_1 \quad (3.26)$$

The rotation matrix which rotates vectors through some rotation,  $R$ , is the same as the rotation matrix which describes a frame rotated by  $R$  relative to the reference frame. Another notation for a rotational operator which clearly indicates which axis is being rotated about:

$${}^A P_2 = R_K(\theta) {}^A P_1 \quad (3.27)$$

$R_K(\theta)$  is a rotational operator which performs a rotation about axis direction  $\hat{K}$  by an amount  $\theta$  degrees. The rotation matrix about  $\hat{X}$ ,  $\hat{Y}$ , and  $\hat{Z}$  are shown below:

$$R_X(\theta) = \begin{bmatrix} 1 & 0 & 0 \\ 0 & \cos \theta & -\sin \theta \\ 0 & \sin \theta & \cos \theta \end{bmatrix} \quad (3.28)$$

$$R_Y(\theta) = \begin{bmatrix} \cos \theta & 0 & \sin \theta \\ 0 & 1 & 0 \\ -\sin \theta & 0 & \cos \theta \end{bmatrix} \quad (3.29)$$

$$R_Z(\theta) = \begin{bmatrix} \cos \theta & -\sin \theta & 0 \\ \sin \theta & \cos \theta & 0 \\ 0 & 0 & 1 \end{bmatrix} \quad (3.30)$$

writing this operator as a homogeneous transform which rotates about  $\hat{Z}$  axis by  $\theta$  is shown in equation (3.28.) There is no translation so the position vector part is zero.

$$R_z(\theta) = \begin{bmatrix} \cos \theta & -\sin \theta & 0 & 0 \\ \sin \theta & \cos \theta & 0 & 0 \\ 0 & 0 & 1 & 0 \\ 0 & 0 & 0 & 1 \end{bmatrix} \quad (3.28)$$

### 3.1.10 Transformation operators

The transform with both rotates by  $R$  and translates by  $Q$  is the same as the transform which describes a frame rotated by  $R$  and translated by  $Q$  relative to the reference frame. The transformation operator is usually related to the homogeneous transform with general rotation matrix and position vector parts.

### 3.1.11 Z-Y-X Euler angles

Figure 3.6 represents rotations of the frame  $\{B\}$  related to frame  $\{A\}$ . The possible description of a frame  $\{B\}$  is as follows:

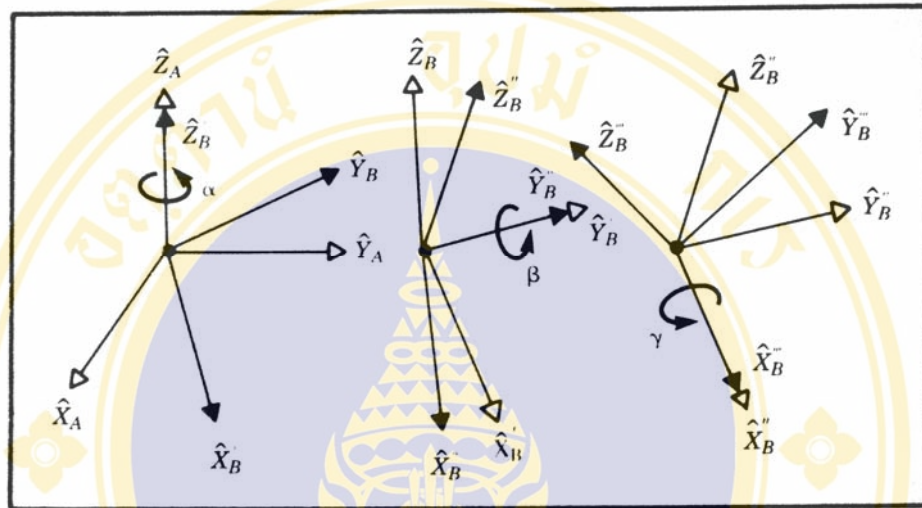


**Figure 3.6** Represents rotations of the frame  $\{B\}$  related to frame  $\{A\}$

Start with the frame coincident with a known frame  $\{A\}$ . First rotate  $\{B\}$  about  $\hat{Z}_B$  by an angle  $\alpha$ , then rotate about  $\hat{Y}_B$  by an angle  $\beta$ , and then rotate about  $\hat{X}_B$  by an angle  $\gamma$ . Each rotation is performed about an axis of the moving system  $\{B\}$ , rather than the system  $\{A\}$  which is fixed as a reference. These set of three rotations are called “Euler angles.” The order of rotations about axes is represented the *Z-Y-X Euler angles*.

An additional “prime” is added to each axis with each rotation. A rotation matrix which is parameterized by Z-Y-X Euler angles will be indicated with the notation  ${}^A R_{Z'Y'X'}(\alpha, \beta, \gamma)$ .

$$\begin{aligned}
 {}^A R_{Z'Y'X'} &= R_Z(\alpha)R_Y(\beta)R_X(\gamma) \\
 {}^A R_{Z'Y'X'} &= \begin{bmatrix} c\alpha & -s\alpha & 0 \\ s\alpha & c\alpha & 0 \\ 0 & 0 & 1 \end{bmatrix} \begin{bmatrix} c\beta & 0 & s\beta \\ 0 & 1 & 0 \\ -s\beta & 0 & c\beta \end{bmatrix} \begin{bmatrix} 1 & 0 & 0 \\ 0 & c\gamma & -s\gamma \\ 0 & s\gamma & c\gamma \end{bmatrix} \quad (3.29)
 \end{aligned}$$

where  $s\alpha = \sin \alpha$  and  $c\alpha = \cos \alpha$ , etc. Multiplying together, one obtains:

$${}^A_B R_{Z'Y'X'}(\alpha, \beta, \gamma) = \begin{bmatrix} c\alpha c\beta & c\alpha s\beta s\gamma - s\alpha c\gamma & c\alpha s\beta c\gamma + s\alpha s\gamma \\ s\alpha c\beta & s\alpha s\beta s\gamma + c\alpha c\gamma & s\alpha s\beta c\gamma - c\alpha s\gamma \\ -s\beta & c\beta s\gamma & c\beta c\gamma \end{bmatrix} \quad (3.30)$$

### 3.1.12 Z-Y-Z Euler angles

Regarding to the order of rotations about axes from section 3.1.11, the Z-Y-Z Euler angles rotation can be started with the frame coincident with a known frame  $\{A\}$ . First rotate  $\{B\}$  about  $\hat{Z}_B$  by an angle  $\alpha$ , then rotate about  $\hat{Y}_B$  by an angle  $\beta$ , and then rotate about  $\hat{Z}_B$  by an angle  $\gamma$ . Each rotation is performed about an axis of the moving system  $\{B\}$ , rather than the system  $\{A\}$  which is fixed as a reference. The equivalent rotation matrix is shown below:

$${}^A_B R_{Z'Y'Z'}(\alpha, \beta, \gamma) = \begin{bmatrix} c\alpha c\beta c\gamma - s\alpha s\gamma & -c\alpha c\beta s\gamma - s\alpha c\gamma & c\alpha s\beta \\ s\alpha c\beta c\gamma + c\alpha s\gamma & -s\alpha c\beta s\gamma + c\alpha c\gamma & s\alpha s\beta \\ -s\beta c\gamma & s\beta s\gamma & c\beta \end{bmatrix} \quad (3.31)$$

The solution for extracting Z-Y-Z Euler angles from a rotational matrix is shown below:

$${}^A_B R_{Z'Y'Z'}(\alpha, \beta, \gamma) = \begin{bmatrix} r_{11} & r_{12} & r_{13} \\ r_{21} & r_{22} & r_{23} \\ r_{31} & r_{32} & r_{33} \end{bmatrix} \quad (3.32)$$

If  $\beta \neq 0$ , then

$$\beta = A \tan 2(\sqrt{r_{31}^2 + r_{32}^2}, r_{33}),$$

$$\alpha = A \tan 2(r_{23} / s\beta, r_{13} / s\beta),$$

$$\gamma = A \tan 2(r_{32} / s\beta, -r_{31} / s\beta), \quad (3.33)$$

If  $\beta = 0.0$ , then a solution may be calculated as

$$\begin{aligned} \beta &= 0.0, \\ \alpha &= 0.0, \\ \gamma &= A \tan 2(-r_{12}, r_{11}), \end{aligned} \quad (3.34)$$

If  $\beta = 180.0^\circ$ , then the solution may be calculated as

$$\begin{aligned} \beta &= 180.0^\circ \\ \alpha &= 0.0, \\ \gamma &= A \tan 2(r_{12}, -r_{11}), \end{aligned} \quad (3.35)$$

## 3.2 Related Image Processing Techniques

### 3.2.1 Introduction

There are four main different image processing algorithms to be divided. First, Image Enhancement is to process an image and the result is suitable for a particular application. Related Image Enhancement includes Neighbors of pixel, Intensity Transformation functions, Logarithmic and Contrast-Stretching Transformations, Histogram Processing, and Linear Spatial filtering. Second, Image Registration includes Geometric Transformation and Image registration. Third, Image Segmentation is involves subdividing an image into constituent parts or isolating certain aspects of an image, including with finding lines, circles, or particular shapes in an image, and identifying the objects in an image. Related Image Segmentation includes Point Detection, Line Detection, Edge Detection. Final, Morphological image processing is the approach that offers this possibility of shape-size based image segmentation.

### 3.2.2 Related Image Enhancement

The spatial domain processes discussed in this topic are denoted by the expression [31]:

$$g(x, y) = T[f(x, y)] \quad (3.36)$$

Where  $f(x, y)$  = the input image,  
 $g(x, y)$  = the output (processed) image  
 $T$  = an operator on  $f(x, y)$

These are defined over a specified neighborhood about point  $(x, y)$ . The principal approach for defining spatial neighborhoods about a point  $(x, y)$  is to use a square or rectangular region centered at  $(x, y)$ .

- **Neighbors of Pixel**

A pixel  $p$  at the coordinates  $(x, y)$  has four horizontal and vertical neighbors whose coordinates are given by:

$$(x + 1, y), (x - 1, y), (x, y + 1), (x, y - 1) \quad (3.37)$$

This set of pixels, called the 4-neighbors of  $p$  is denoted by  $N_4(p)$ . Each pixel is a unit distance from  $(x, y)$ , and some of the neighbors of  $p$  lie outside the digital image if  $(x, y)$  is on the border of the image. The four diagonal neighbors of  $p$  have coordinate:

$$(x + 1, y + 1), (x + 1, y - 1), (x - 1, y + 1), (x - 1, y - 1) \quad (3.38)$$

and are denoted by  $N_D(p)$ . Therefore summarizing all points are called 8-neighbors of  $p$  and denoted by  $N_8(p)$ .

- **Intensity Transformation Functions**

The basic form of the transformation  $T$  is when the neighborhood is a single pixel (size  $1 \times 1$ .) In this case, the value of  $g(x, y)$  depends only on the intensity of  $f(x, y)$ , and  $T$  becomes an intensity or gray-level transformation function. These two terms are used interchangeably when dealing with monochrome (i.e., gray-scale) images. When dealing with color images, the term intensity is used to denote a color image component in certain color spaces. Because they depend only on intensity values, and not explicitly on  $(x, y)$  intensity transformation functions frequently are written in simplified form as:

$$s = T(r) \quad (3.39)$$

where  $r$  = denotes the intensity of  $f(x, y)$

$s$  = the intensity of  $g(x, y)$ .

There are four basic types of digital images. First is the binary image, each pixel is representing just only two values which are black and white. This type is one of the most popularly used in medical imaging because it is easy to process due to less complexity and needs only 1 bit per pixel. Therefore the image can be very efficient in terms of storage. Second is the grayscale image, each pixel is a shade of gray, normally from 0 to 255 while “0” represents as black and “255” represents as white color. The range means that each pixel can be represented by 8 bits, or exactly 1 byte. This is a very natural range for image file handling. Other gray scale ranges are used, but generally they are a power of 2. The third is the true color or red-green-blue image, each pixel has a particular color that color being described by the amount of red, green, and blue in it. This type is not popular in medical imaging because of the time consuming in each process. Medical imaging need less time of consuming in processing. The fourth is indexed image, most color images have only a small subset of more than 16 million possible color. The image has an associated color map, or

color palette. Each pixel has a value that does not give its color, but an index to the color in the map.

- **Logarithmic and Contrast-Stretching Transformations**

Logarithmic and contrast-stretching transformations are basic tools for naming range manipulation. Logarithm transformations are implemented using the expression:

$$g = c * \log(1 + \text{double}(f)) \quad (3.40)$$

where  $c$  = a constant value.

Contrast-stretching transformation function is shown in equation (3.41).

$$s = T(r) = \frac{1}{1 + (m/r)^E} \quad (3.41)$$

where  $r$  = the intensities of the input images.

$s$  = the corresponding intensity values in the output image.

$E$  = controls the slope of the function.

- **Histogram Processing**

Intensity transformation functions based on information extracted from image intensity histograms play a basic role in image processing, in areas such as enhancement, segmentation, and description. The histogram of a digital image with  $L$  total possible intensity levels in the range  $[0 \ G]$  is defined as the discrete function:

$$h(r_k) = n_k \quad (3.42)$$

where  $r_k$  = the  $k^{\text{th}}$  intensity level in the interval  $[0 \ G]$

$n_k$  = the number of pixels in the image whose intensity level is  $r_k$ .

Normalized histograms are usually used in general works by dividing all elements of  $h(r_k)$  by the total number of pixels in the image, which denoted by  $n$  :

$$p(r_k) = \frac{h(r_k)}{n} = \frac{n_k}{n} \quad (3.43)$$

where  $p(r_k) =$  an estimate of the probability of occurrence of intensity level  $r_k$  .

- **Linear Spatial Filtering**

The linear operations of interest in this topic consist of multiplying each pixel in the neighborhood by a corresponding coefficient and summing the results to obtain the response at each point  $(x, y)$  . If the neighborhood is of size,  $m \times n$  ,  $mn$  coefficients are required. The coefficients are arranged as a matrix called “a filter mask, mask, kernel, template, or window.” The process consists simply of moving the center of the mask  $w$  from point to point in an image,  $f$  . At each point  $(x, y)$  , the response of the filter at that point is the sum of products of the filter coefficients and the corresponding neighborhood pixels in the area spanned by the filter mask. For mask size  $m \times n$  , one assumes typically that  $m = 2a + 1$  and  $n = 2b + 1$  , where  $a$  and  $b$  are positive integers. All this says is that the principal focus on masks of odd sizes, with the smallest meaningful size being  $3 \times 3$  .

### 3.2.3 Related Image Registration

Image restoration is to locate the objects in 2D to 3D. The related topic of this section is geometric spatial transformations and image registration.

- **Geometric Spatial Transformations**

Geometric transformations modify the spatial relationship between pixels in an image. Geometric transformations are used frequently to perform image registration, a

process that takes two images of the same scene and aligns them to merge them for visualization, or for quantitative comparison.

Suppose that an image,  $f$ , defined over a  $(w, z)$  coordinate system, undergoes geometric distortion to produce an image,  $g$ , defined over an  $(x, y)$  coordinate system. This transformation may be expressed as

$$(x, y) = T\{(w, z)\} \quad (3.44)$$

One of the most commonly used forms of spatial transformations is the “affine transform.” The affine transform can be written in matrix form as

$$\begin{bmatrix} x & y & 1 \end{bmatrix} = \begin{bmatrix} w & z & 1 \end{bmatrix} T = \begin{bmatrix} w & z & 1 \end{bmatrix} \begin{bmatrix} t_{11} & t_{12} & 0 \\ t_{21} & t_{22} & 0 \\ t_{31} & t_{32} & 1 \end{bmatrix} \quad (3.45)$$

This transformation can scale, rotate, translate, or shear a set of points, depending on the values chosen for the elements of  $T$ .

- **Image Registration**

Image registration methods seek to align two images of the same scene. In any cases, combining the images or performing quantitative analysis and comparisons requires compensating for geometric aberrations caused by differences in camera viewing angle, distance and orientation.

### 3.2.4 Related Image Segmentation

Segmentation subdivides an image into its constituent regions or objects. Segmentation accuracy determines the eventual success or failure of computerized analysis procedures. Segmentation algorithms for monochrome images generally are

based on one of two basic properties of image intensity values, discontinuity and similarity.

- **Point Detection**

The detection of isolated points embedded in areas of constant or nearly constant intensity in an image is straightforward in principle. Using the mask shown in Figure 3.7, which shows an isolated point, has been detected at the location on which the mask is centered if  $|R| \geq T$ .

-1	-1	-1
-1	8	-1
-1	-1	-1

**Figure 3.7** A mask for point detection

The response,  $R$ , of the mask at any point in the image is given by:

$$R = w_1 z_1 + w_2 z_2 + \dots + w_9 z_9 = \sum_{i=1}^9 w_i z_i \tag{3.46}$$

- where  $z_i$  = the intensity of the pixel  
 $w_i$  = mask coefficient  
 $T$  = nonnegative threshold.

- **Line Detection**

Consider the masks in Figure 3.8. Moving the mask around an image, it would respond more strongly to lines (one pixel thick) oriented horizontally and vertically respectively. With a constant background, the maximum response would result when the line pass through the middle row and column of the mask respectively.

Let  $R_1, R_2, R_3$ , and  $R_4$  denote the responses of the masks in Figure 3.8. Suppose that the four masks are run separately through an image. If, at a certain point

in the image,  $|R_i| > |R_j|$ , for all  $j \neq i$ , that point is said to be more likely associated with a line in the direction of mask  $i$ .

-1	-1	-1
2	2	2
-1	-1	-1

Horizontal

-1	-1	2
-1	2	-1
2	-1	-1

+45 degrees

-1	2	-1
-1	2	-1
-1	2	-1

Vertical

2	-1	-1
-1	2	-1
-1	-1	2

-45 degrees

**Figure 3.8** The masks for line detection

- **Edge Detection**

Although, point and line detection certainly are important in any direction, edge detection is by far the most common approach for detecting meaningful discontinuities in intensity values. Such values are detected by first-and second-order derivatives. The first-order derivative of choice in image processing is the gradient. The gradient function,  $\nabla f(x, y)$ , is denoted as the vector

$$\nabla f = \begin{bmatrix} G_x \\ G_y \end{bmatrix} = \begin{bmatrix} \frac{\partial f}{\partial x} \\ \frac{\partial f}{\partial y} \end{bmatrix} \quad (3.47)$$

The magnitude of this vector is

$$\nabla f = \text{mag}(\nabla f) = [G_x^2 + G_y^2]^{1/2} \quad (3.48)$$

$$= [(\partial f / \partial x)^2 + (\partial f / \partial y)^2]^{1/2} \quad (3.49)$$

To simplify computation, this quantity is approximated sometimes by omitting the square-root operation,

$$\nabla f \approx G_x^2 + G_y^2 \quad (3.50)$$

Or by using absolute values,

$$\nabla f \approx |G_x| + |G_y| \quad (3.51)$$

These approximations still behave as derivatives; that is, they are zero in areas of constant intensity and their values are proportional to the degree of intensity change in areas whose pixel values are variable.

A fundamental property of the gradient vector is that it points in the direction of the maximum rate of change of  $f$  at coordinates  $(x, y)$ . The angle which this maximum rate of change occurs is

$$\alpha(x, y) = \tan^{-1}\left(\frac{G_y}{G_x}\right) \quad (3.52)$$

Second derivatives in image processing are generally computed using the Laplacian.

The 2-D function  $f(x, y)$  is formed second-order derivatives, as follows:

$$\nabla^2 f(x, y) = \frac{\partial^2 f(x, y)}{\partial x^2} + \frac{\partial^2 f(x, y)}{\partial y^2} \quad (3.53)$$

The Laplacian is rarely used by itself for edge detection because, as a second-order derivatives, it is unacceptably sensitive to noise, its magnitude produces double edges, and it is unable to detect edge direction. The basic concept of edge detection is to find places in an image where the intensity changes rapidly by using one of two general criteria; First, find places where the first derivative of the intensity is greater in magnitude than a specified threshold. Second, find places where the second derivative of the intensity has a zero crossing. There are many edge detectors such as Sobel, Prewitt, Laplacian of a Gaussian, Canny, and etc. Canny edge detector is applied in

this work. Canny edge detector is the most powerful edge detector. The method can be summarized as follows:

1. The image is smoothed by using a Gaussian filter with a specified standard deviation,  $\sigma$ , to reduce noise.
2. The local gradient,  $g(x, y) = [G_x^2 + G_y^2]^{1/2}$ , and edge direction,  $\alpha(x, y) = \tan^{-1}(\frac{G_y}{G_x})$ , are computed at each point. An edge point is defined to be a point whose strength is locally maximum in the direction of the gradient.
3. The edge points determined in (2) give rise to ridges in the gradient magnitude image. The algorithm then tracks along the top of these ridges and sets to zero all pixels that are not actually on the ridge top so as to give a thin line in the output, a process known as nonmaximal suppression. The ridge pixels are then thresholded using two thresholds,  $T_1$  and  $T_2$ , with  $T_1 < T_2$ . Ridge pixels with values greater than  $T_2$  are said to be strong edge pixel. Ridge pixels with value between  $T_1$  and  $T_2$  are said to be weak edge pixels.
4. Finally the algorithm performs edge linking by incorporating the weak pixels that are 8- connected to the strong pixels.

### 3.2.5 Morphological Image Processing

Morphological image analysis [26, 27] is the approach that offers this possibility of shape-size based image segmentation. This generally involves ‘operating’ the image with a kernel known as ‘structuring element’. The structuring element is chosen similar to the shape and size of the object sought in the image. The operation performed depends on the morphological operator chosen. The two most basic operations are *erosion* and *dilation*; two other widely used operations, which are derived from the basic ones, are those of *opening* and *closing*. The effect of applying these operations is illustrated in Figure 3.9.

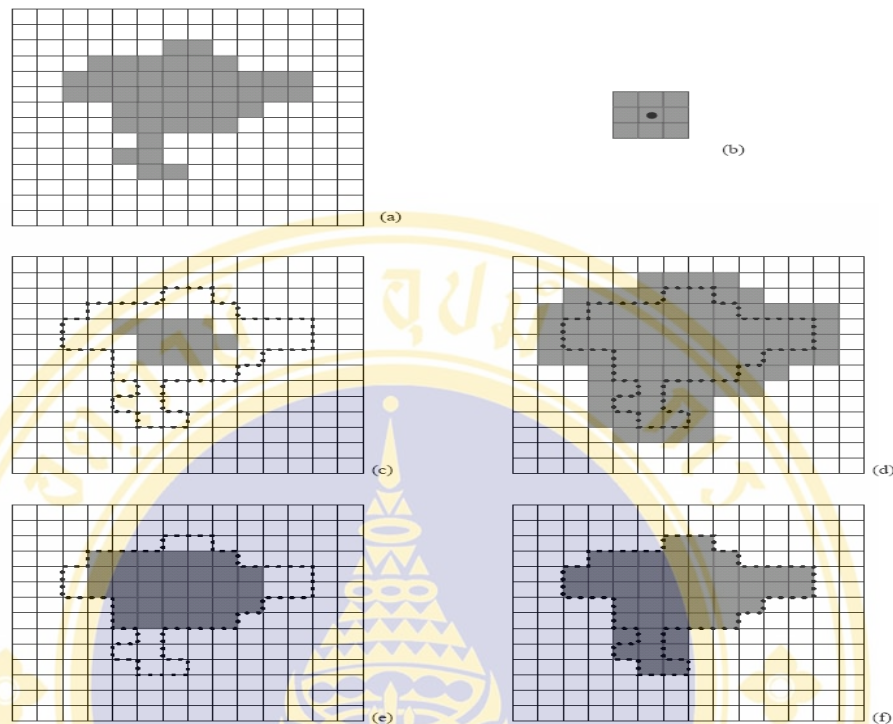


**Figure 3.9** Illustration of basic morphological operations: a) Original set; b) Structuring element: square of side 3, reference pixel is at center; c) erosion; d) dilation; e) opening; f) closing. *Source: Chapter 5, Image Analysis for the Biological Sciences - Glasbey, C.A. and Horgan, G.W. (published by Wiley in 1995, but now out of press).*

Many complex operations can be achieved by combining these two basic operations. One very important operator in this context for our usage is *top-hat* transform (Refer to Figure 3.10). The *top-hat* transform is used for extracting small/narrow, bright or dark features in an image, which in our case are implanted seeds. The *top-hat* transform involves the subtraction of *opened (or closed)* image from the original image to extract bright (or dark) objects by using a structuring element which has the similar shape as the object and size greater than object such that it completely encloses the object inside itself. This is because the *opening (or closing)* will have eliminated them and they will become apparent when the *opened (or closed)* image will be subtracted from original image.

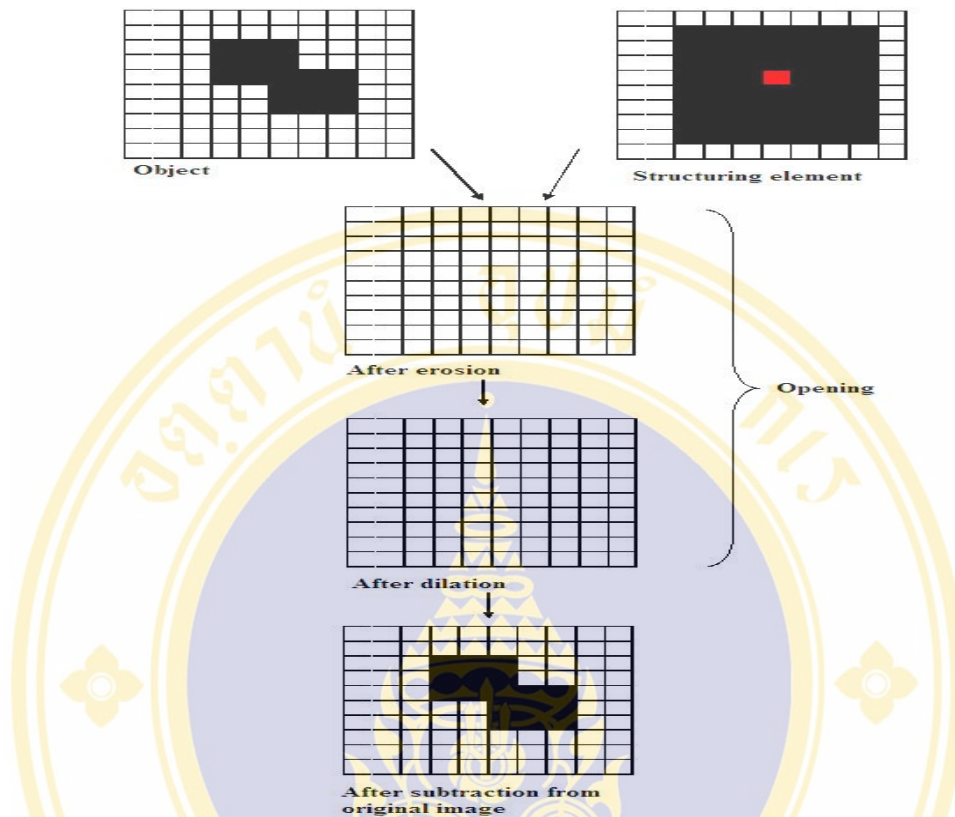


**Figure 3.10** Illustration of morphological *top-hat* transform.

## Part II: Developed Methods

### 3.3 Overview methods of Fluoro-Navigation for Closed Intramedullary Nailing of Femur

The overview methods are shown in Figure 3.11. The operation starts after the surgeon inserts an IMN into the femur canal and sets the fractured bone into the desired position [28]. Two markers are attached to the patient in the location that can be seen from both fluoroscopic and optical stereoscopic imaging systems. The attaching procedure is done by attaching each marker directly to the distal and proximal part of the fractured bone through the skin (one marker for each position.)

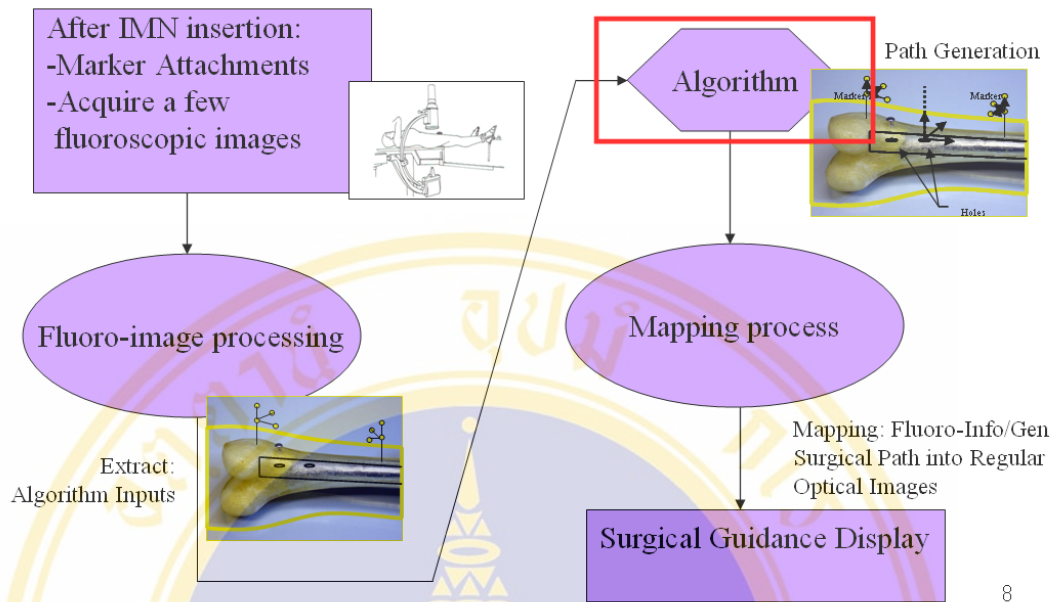


**Figure 3.11** The overview methods

Then, two X-ray images are taken by the fluoroscopic (C-Arm) system from different angles. The image processing and pattern recognition methods are used to generate (1) the frames attached to the markers, (2) the axis of the IMN and its perimeter, and (3) the screwing holes' location and orientation (pose) on the IMN. Note that in most cases, the shape of screwing holes viewed on X-ray images are elliptical as shown in Figure 3.12, and a set of diagrams comparing between optical stereoscopic and fluoroscopic images is shown in Figure 3.13.

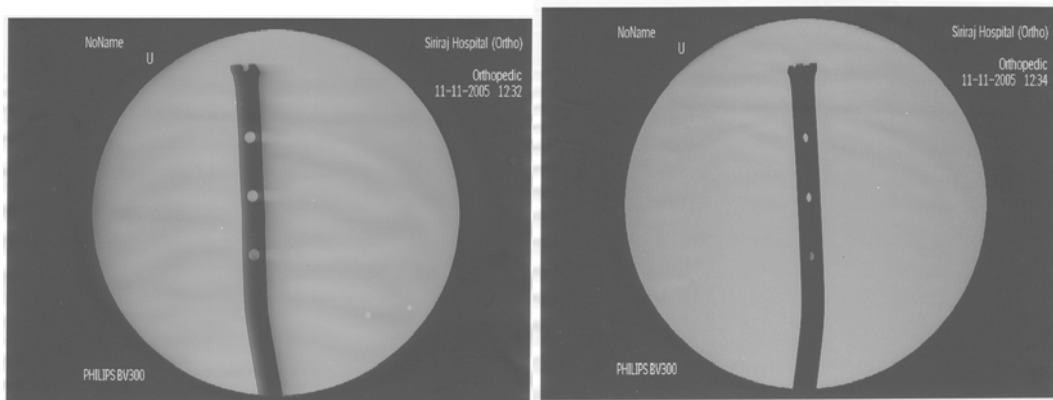


**Figure 3.12** X-ray images of an IMN in the difference of viewing from the C-arm.

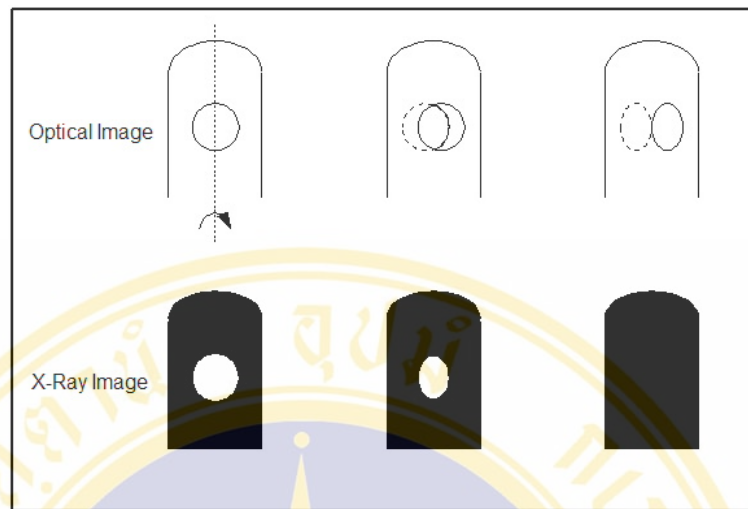


**Figure 3.13** IMN diagram comparing images as seen from the optical stereoscopic (upper) and fluoroscopic (lower) systems.

Simultaneously, the optical stereoscopic imaging system is capturing and generating the frames attached to the same markers. A computer algorithm registers generated frames from both systems thus producing an insertion path which aids surgeon to navigate during the screw inserting procedure. Because the marker is fixed rigidly to the bone and visible on the optical stereoscopic images, the computer software uses this information to construct and track the insertion path, regardless of the patient's movement. During the screw insertion procedure, the proposed system requires only real-time images from the optical stereoscopic system which can be taken continuously and without risk of radiation exposure. The pre-registered insertion path generated from the algorithm is mapped onto the real-time optical images. The real-time images are shown on the monitors from two different views and angles so that the surgeon can use this guiding path to aid the surgical navigation.

The interested part of this project is the algorithm to recover the distal hole's axis. This stage consists of fluoroscopic image processing, mathematical modeling and information processing, surgical planning, image mapping and monitoring. Fluoroscopic image processing is to extract distal hole figures from an X-ray image. The mathematical modeling and information processing are to retrieve distal hole position and orientation using information from X-ray images. Surgical planning is to generate a guiding path for physician to follow. Image mapping is to map generated guiding path and other information from X-ray images onto optical images from an

optical stereoscopic system. Monitoring is to display and interface between navigation system and surgeon. Each subsystem is to be developed separately and integrated in the next stage. Due to the complexity of current research problems, this project focuses on how to determine the axis of the IMN, and the screwing holes' locations (using a 2-D fluoroscopic image) without trying to relate the IMN axes and IMN hole pose to the frames of reference generated using the markers.

Also, to further simplify the problem, it is assumed that the IMN translational movement is allowed in the X and Y directions (as shown in Figure 3.14), whereas the IMN rotational movement is allowed in the X axis.

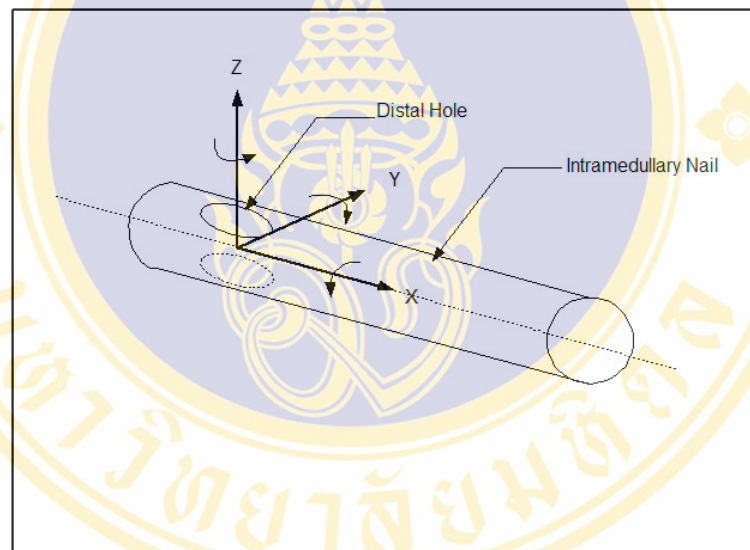


**Figure 3.14** Distal hole axes.

The estimation of IMN distal hole axis can be divided into two major algorithm of tasks, which are Recovery of distal holes axis using X-Y span of distal hole's projection images, and Recovery of distal holes axis using interested area of distal hole's projection images. This overview method supports only sections 3.4 and 3.5. Section 3.6 talks about the new method using a fiducial called "Fluoroscope Tracking or FTRAC."

### 3.4 Recovery of distal holes axis using X-Y span of distal hole's projection images

The approach starts with generating database of nail's projection images. These images are generated to simulate all possible X-ray images of nail during the operation. All images are to be extracted four sets of informative parameters which are 1) the length of line between intersection points of upper and lower distal holes (denoted as "a", or "H"), which is the longest line in the ellipse, 2) the slope of the same line (denoted as "theta", 3) the maximum width of crossed distal holes (denoted as "b" or "V"), and 4) slope of nail edges' slopes. The equations for determining the parameters are shown below:

$$\|V\|_n = [(x_2 - x_1)^2 + (y_2 - y_1)^2]^{1/2} \quad (3.54)$$

$$\|H\|_n = 2 * [R^2 - (R - (\|V\|/2))^2]^{1/2} \quad (3.55)$$

$$\theta = \tan^{-1} \left( \frac{y}{x} \right) \quad (3.56)$$

where  $\|V\|$  = magnitude of the vertical line or line "b."

$\|H\|$  = magnitude of the horizontal line or line "a."

$R$  = radius of the distal hole, which is a known parameter.

$n$  = the order of collected data.

$\theta$  = slope of line "a", which is a known parameter from the simulation.

Next is to store rotation angles ( about X-, Y- and Z-Axes) and four parameter sets into the database system. The distal hole's axis recovering algorithm is working by matching the result from X-ray image to the stored database information. The overall approach can be illustrated in the diagram of Figure 3.16. (See Figure 3.15 for

all notations.) In order to test the algorithm, simulations were done in stages. The simulation started with pure rotation about X-axis, pure rotation about Y-axis, combination of X-Y rotations, and combination of X-Y-Z rotations. Figure 3.17 shows the example of a simulation rotation about x-axis.

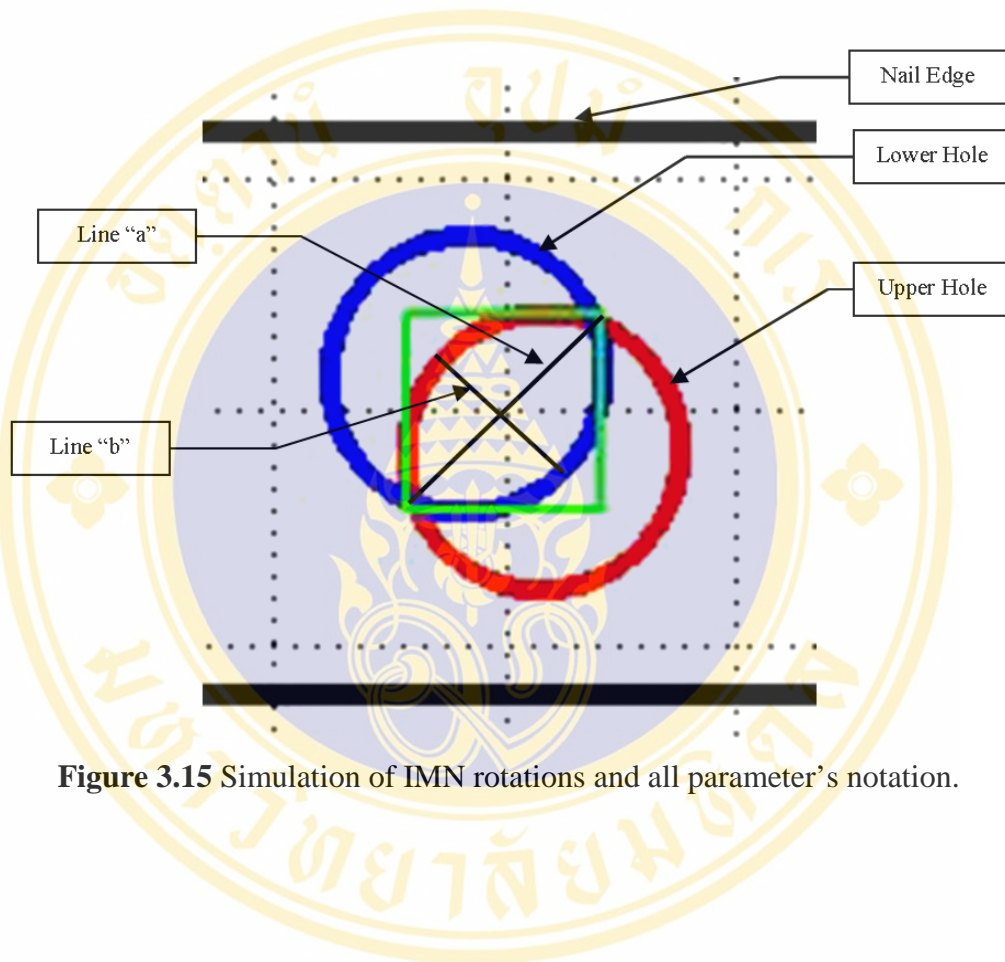


**Figure 3.15** Simulation of IMN rotations and all parameter's notation.

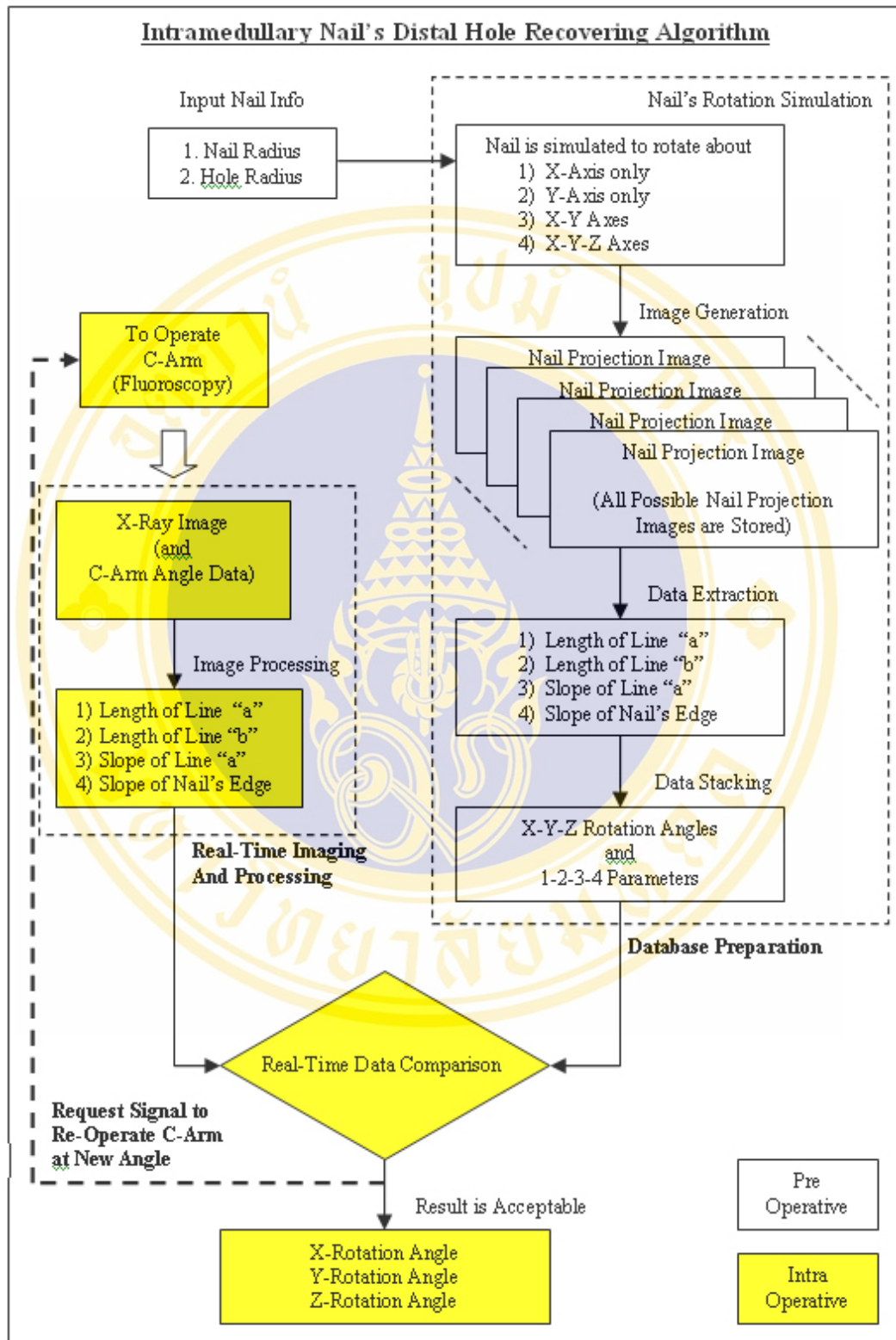


**Figure 3.16** Diagram of the Proposed Algorithm to Recover Intramedullary Nail's Distal Hole Axis

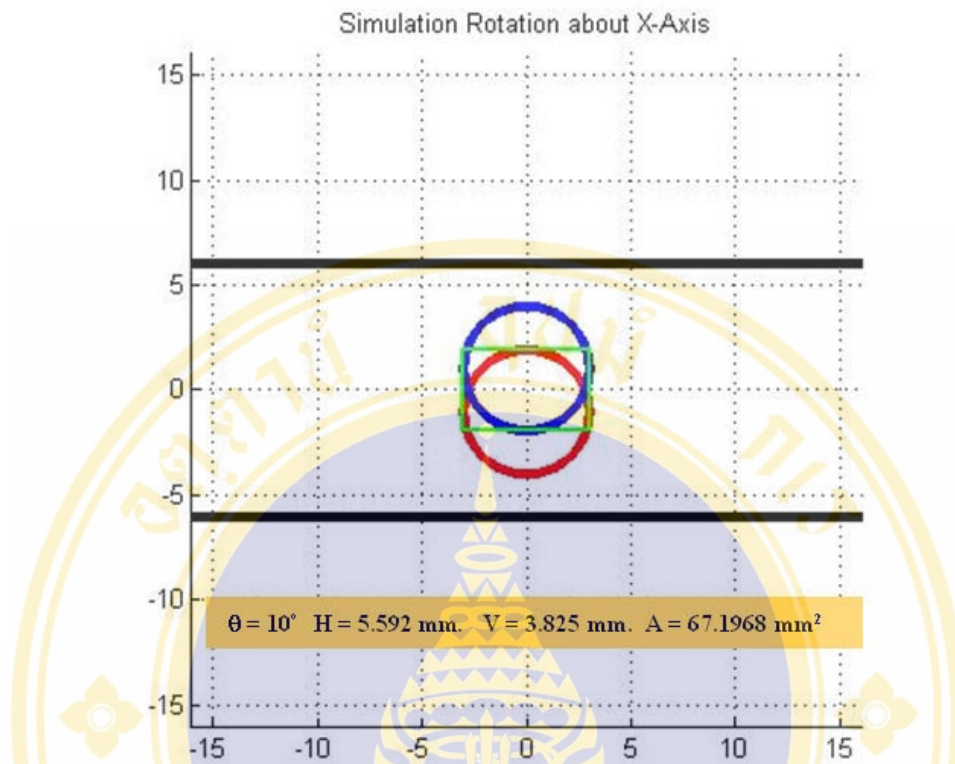


**Figure 3.17** Simulation Rotation of the IMN about X-Axis

### 3.5 Recovery of distal holes axis using interested area of distal hole's projection images

This method is continued from the first method which uses the X-Y span of distal hole's projection images. In order to prove the proposed algorithm, an implementation is done by using an experimental set up. The assumptions in the implementation are: 1) nail rotates about its axis only; 2) nail is in a cylindrical shape; 3) the distal holes are in circular shapes and 4) diameters of nail and its distal holes are known. The overview of this algorithm is shown in Figure 3.18.

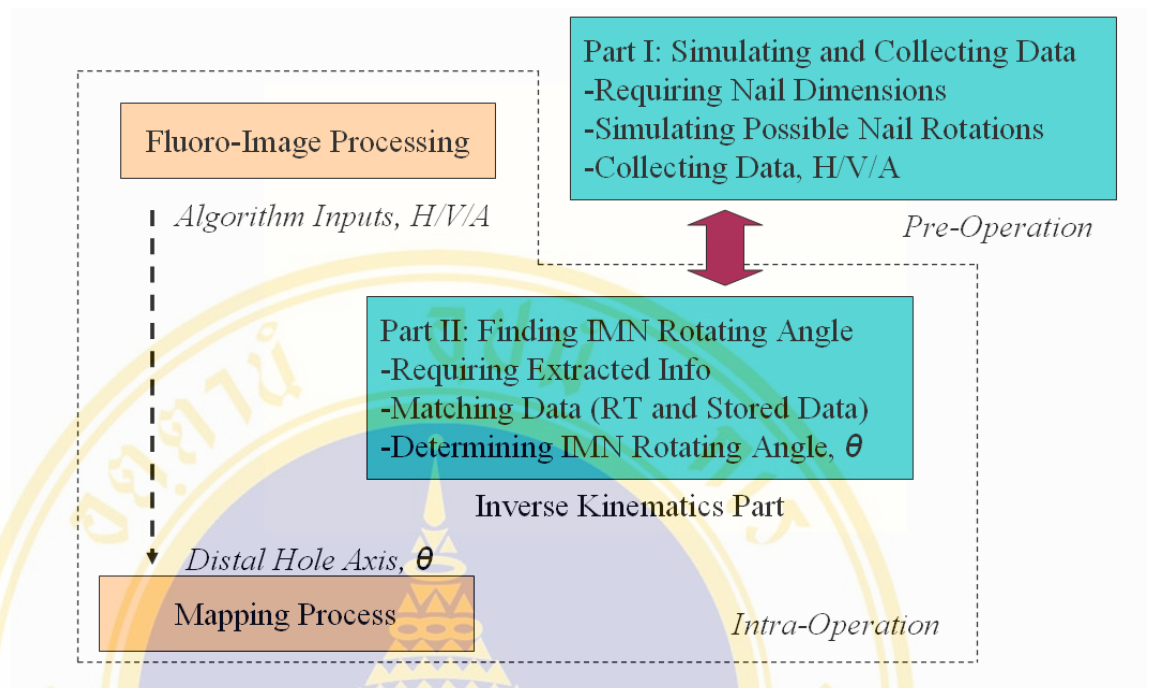


**Figure 3.18** Overall algorithm using the area of the distal hole's projection images

#### *Part I: Collecting Data*

Part I can be divided into two main steps, image preparation and distal hole detecting processes. Image preparation is started with RGB distal hole imaging. The test images were generated using a CCD camera. An IMN was arranged so that it could be rotated around the X-axis. The test images were taken on a white and illuminated background to mimic a fluoroscopic image. The IMN was rotated (around the X-axis) in steps of 0, 5, 10, 15 and 20 degrees clockwise and counter clockwise. All images are converted to be grayscale images.

The second step is to detect the distal hole area. Image cropping technique is applied to detect only interesting part of image. The areas of distal holes are calculated as shown in equation 3.57 and stored during the second step. The data of area vs. angle are plotted on a graph. A fitting curve technique is then applied to find the best fit to the data. The curve, called the "Tool Curve," is used to be the key to reversely determine rotating angle of the IMN. Tool Curve is plotted by applying the quadratic equation. The equation is shown as followed:

$$A = \mathbf{H} \times \mathbf{V} \quad (3.57)$$

$$\theta = ax^2 + bx + c \quad (3.58)$$

where  $a$ ,  $b$  and  $c$  = are constant values.  
 $x$  = the input which is the computed area of an unknown image.  
 $\theta$  = is the output which is the rotation angle in degree.

### *Part II: Determining the IMN rotating angle*

This part is to simulate during the intra-operation process. Images acquired from fluoroscopic system are instantly processed to determine the area of distal hole's projected image. Therefore, matching process of a real-time area data to the Tool Curve is to reversely recover the rotational angle of IMN. This is the same axis which can be used to represent the orientation of distal hole. The experiment set up and result are discussed in chapter 4.

### **3.6 Recovery of distal holes axis using additional fiducial, Fluoroscope Tracking (FTRAC.)**

Fiducial Fluoroscope Tracking (FTRAC) [21, 22] was applied to this work. The approach is to recover the distal hole's axis with the use of FTRAC. To simplify the problem of the movement of bone and soft tissue, the FTRAC is assumed to be attached rigidly to the IMN as shown in Figure 3.19, which is the overview diagram of this method. Data protocol for pose recovery of the FTRAC is shown in Figure 3.20 as well.

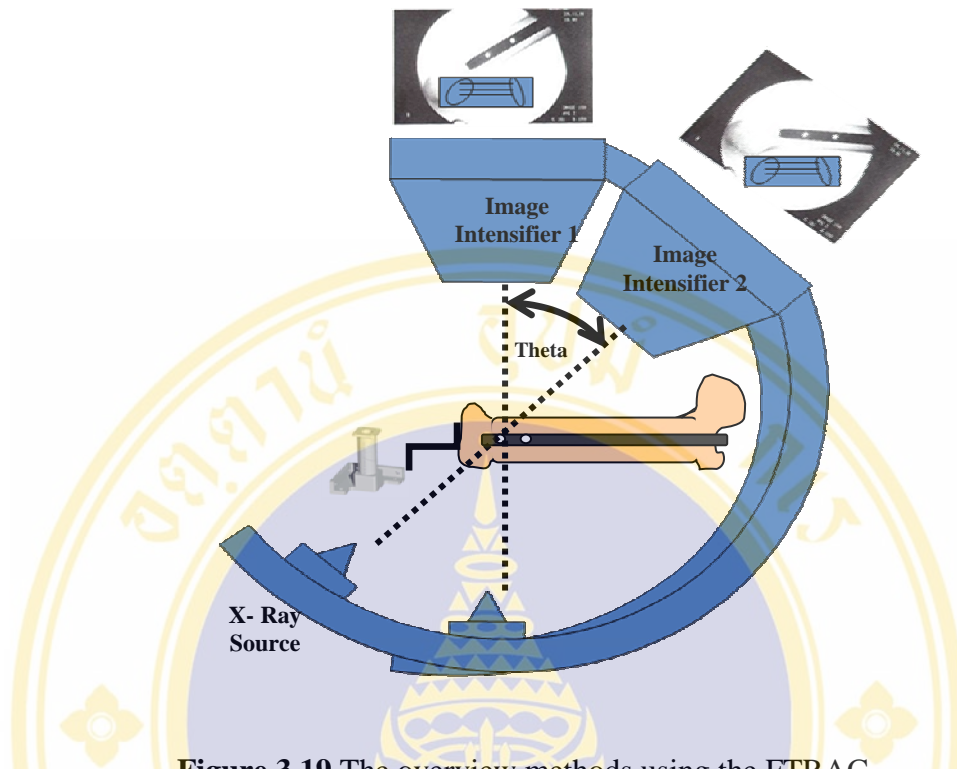
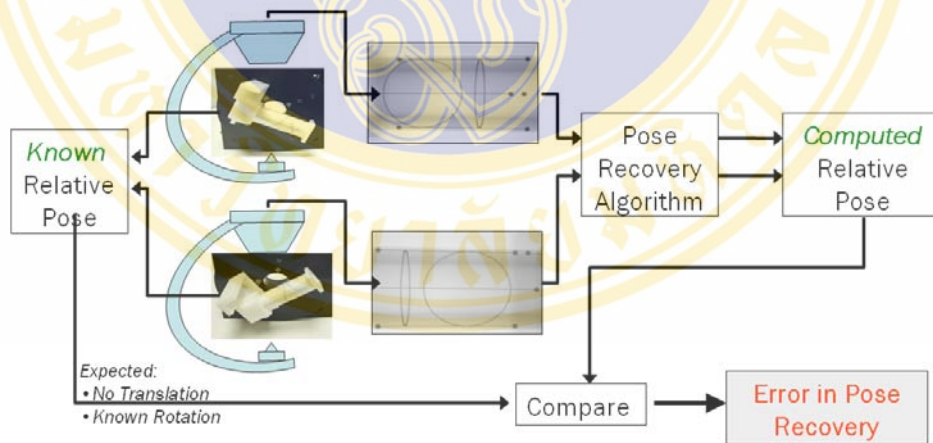


**Figure 3.19** The overview methods using the FTRAC



Courtesy of Ameet Jain

**Figure 3.20** Data protocol for pose recovery of the FTRAC

Major concerned in this method is the image processing especially segmentation of the FTRAC. The benefit of applying the FTRAC to this work is because of its design (the design of FTRAC is shown in Figure 3.21), which is based on mathematical model [21, 22] Basic conceptual designs of the FTRAC are:

- Non-obtrusive small size; need not be close to the anatomy.
- 2 ellipses (along with lines & points.) Both ellipses are rotate at 60 degrees position to each other.
- Ellipses projected as ellipses (robust segmentation.)
- Each pose produces a unique image (encoding 6DOF pose.)

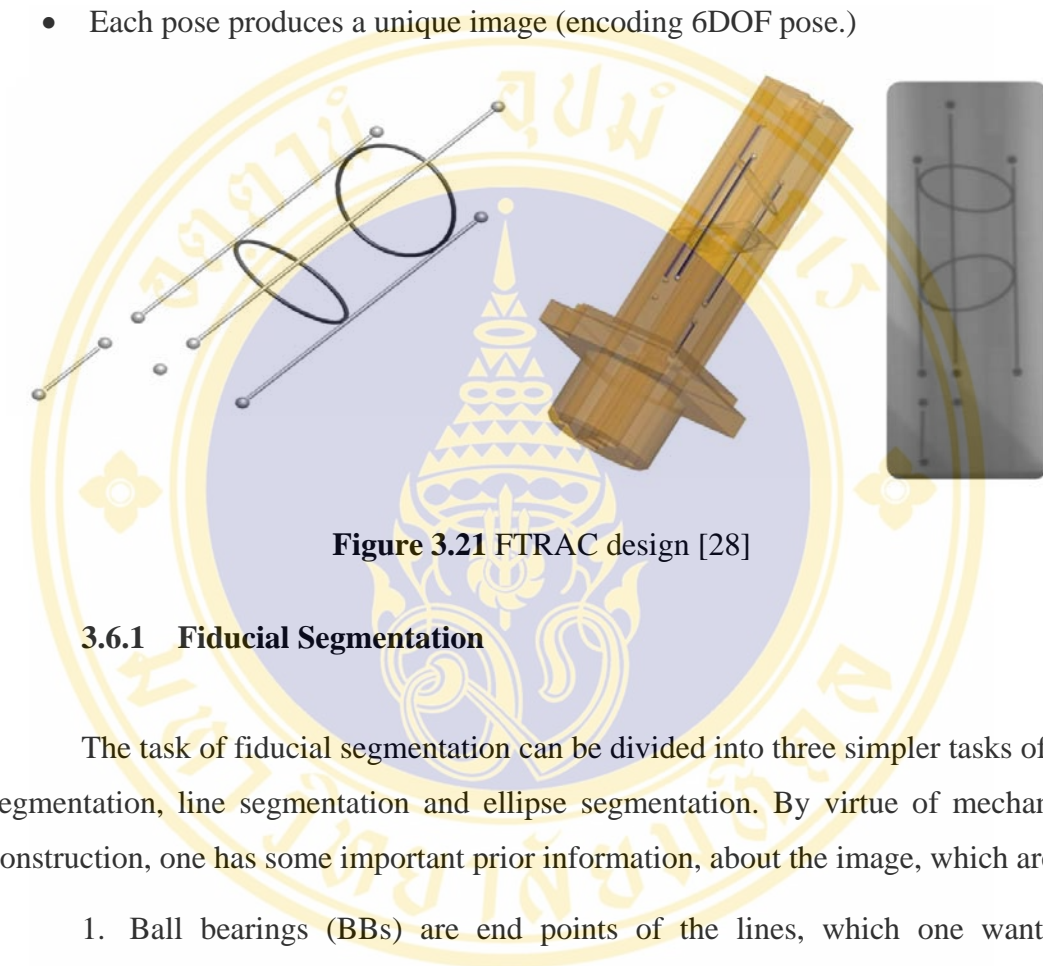


**Figure 3.21** FTRAC design [28]

### 3.6.1 Fiducial Segmentation

The task of fiducial segmentation can be divided into three simpler tasks of BB segmentation, line segmentation and ellipse segmentation. By virtue of mechanical construction, one has some important prior information, about the image, which are:

1. Ball bearings (BBs) are end points of the lines, which one wants to segment.
2. The three lines are parallel to each other; differentiated by the number of BBs they intercept in the lower half of the fiducial.
3. There are two ellipses in the image.

These information are incorporated in the algorithm at various stages. The Flow chart of fiducial segmentation is shown in Figure 3.22. The input and output of this method are:

**Input:** Image buffer of the region of interest containing the fiducial.

**Output:** BB Locations in form  $[CG_x \ CG_y]$ , Line Equations, Ellipse parameters and points (CG is Center of Gravity).

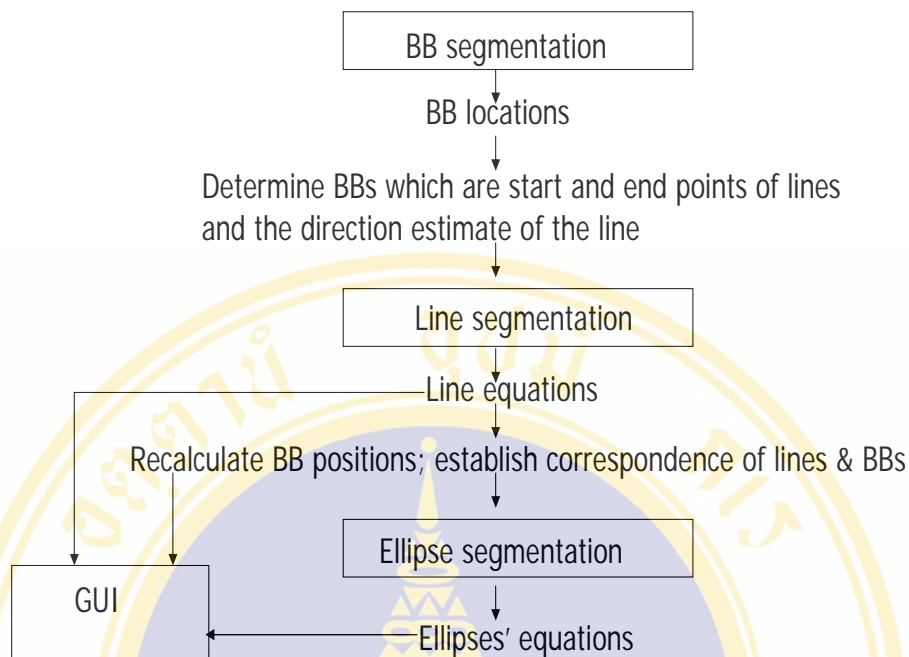


**Figure 3.22** Flow chart of fiducial segmentation.

### 3.6.2 Algorithmic steps involved

- A BB segmentation: Perform BB segmentation using morphological processing (*top-hat transform*).
- A.I Perform gray level morphological *opening* with structuring element, ball of radius 3 and height 1, to obtain another image.
- Note: Since one is looking for a ball bearing in the image, the structuring element should have the shape and size similar to it. However, since the image also contains ellipses & lines, which consist of elements of shape similar to structuring element and smaller size, so after subtraction, those are also segmented out.
- A.II Subtract the image obtained after step A.I from the original image to get another image.
- Note: The image obtained after this step is a gray level image containing only the regions that are identified as BBs or something

that looks like a BB & fits inside the structuring element; which as discussed above will be elements of ellipse and lines.

A.III Perform gray level morphological *opening* with structuring element, 3 by 3 square, to obtain another image.

- Note: Since the element is small it will only lead to segmentation of elements of lines and ellipses, and will leave out BBs

A.IV Subtract the image obtained after step A.III from the original image to get another image.

- Note: The image obtained after step A.IV contains elements of ellipses and lines and some noise, while the image obtained after step A.III contains all these and BBs.

A.V Subtract image obtained after step A.IV from the image obtained after step A.II, to obtain another image, which consists of only BBs and some noise.

A.VI Threshold the image.

- Note: Currently, one uses a threshold value of 22 based on the previous findings [21]. Empirically, it is checked further after labeling the image if the number of BBs fall below 6, then a lower threshold is used.

A.VII Clear border associated noise.

A.VIII Eliminate other small noise, by morphological *area opening* operation. This eliminates any noise left due to some bright bone structures, which might have come out in morphological processed image.

- Note: One eliminates all regions with less than 10 pixel area on the assumption that BB, when segmented, will have more than 10 pixel area.

A.IX Label the image.

A.X Find centroids and record them in the output array (BBLocations).

Line segmentation: One makes assumption that the lines in the image are ‘nearly’ vertical i.e. within  $+45$  to  $-45$  to image’s vertical axis. One use results obtained from step 1 about BB locations as prior information that BBs lie on lines, to get a rough estimate of the start and end points of the lines. If both start and end points of any of the lines are visible, then one has a better estimate of the line direction. The information about the rough start point is essential for the algorithm that follows and expected direction of the line, if available, is a very good heuristic for the algorithm. The algorithm called *A-algorithm* [29], based on graph theory, and is originally an edge-tracking algorithm developed for tracking objects like rivers, roads, curves in satellite imagery. It considers the edge image as a connected and oriented graph. The border detection process is transformed into a search for the optimal path in the weighted graph. Figure 3.23 illustrates this representation.

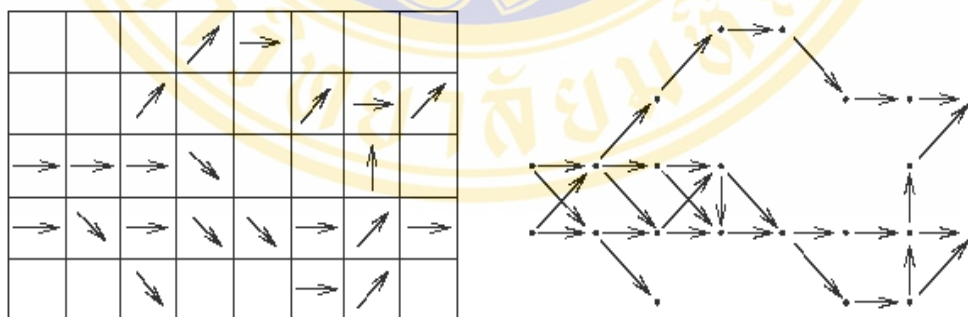


**Figure 3.23** Graph representation of edge image; a) Edge directions; b) corresponding graph. (Source: *Image processing, analysis and machine Vision, Milan Sonka [29]*).

The algorithm is used when the start point and the approximate orientation of the edge to be tracked are known. As a passing remark, the assumption about line being nearly vertical will be gotten rid in near future, by first estimating the projection direction,

then rotating the image such that lines become vertical, then, the same algorithm which is being applied now will be applicable there too.

A.XI Form an edge image by running a 2x2 kernel over the image and performing the derivative magnitude operation.

A.XII Estimate lines starting and ending points from corresponding BB locations (determined earlier from results of Step B.I and the knowledge of physical construction of the fiducial.

- Note: By start point one means the BB from which line starts by looking in image in direction bottom to up and end point where the line ends. For some line only BB may be visible i.e. segmented out, immaterial whether it is a 'start' point or 'end' point, still the following algorithm will be able to perform line segmentation as long as there is at least one point available on the line. It is also important to note that in the array *BBLocations*, and hence in the results obtained after performing this step, one still does not have actually good points on the line, these are the BB centers, and in edge image, these points do not have connectivity to line directly. However, from these points, new points that lie on the lines can be estimated.

A.XIII Calculate closer initial direction estimate if both start and end points of a particular line is known.

- Note: Since the lines are parallel physically, and owing to distortion, they still will be almost parallel in image, so one estimate of line direction of any of the lines is enough.

A.XIV Find edge image threshold. For each line perform these steps:

A.XIV.1 Locate actual start and end point on the line, from given BB points, obtained after step B.II, by fitting a connectivity

mask and choosing a point, which has a high directional connectivity.

A.XIV.2 Extract connected line points by '*A-algorithm*' [29] as graph searching, finding a minimum cost connected path from start point to the end point.

- Note: Since this algorithm operates on very noisy edge image, and also the line is quite thick, the connected points obtained may not be completely straight and accurate. So further processing is required to smooth out the line. One can safely say that after this step one has a very good guess of where to look for the actual line.

A.XIV.3 From the points determined, find 'consistent' line segments of the line by looking in steps of 15 pixels. By consistent it is meant that if a segment has too much of y-variation, then it likely to be noise, so one would rather discard it. Collect all the consistent segments as one list of points.

A.XIV.4 For each point in the list of points available after step B.IV.3, locate a 'good' point. By good point we mean it is the highest intensity point in 1 pixel neighborhood on either side of the point in question.

- Note: This is done because the line is quite thick, and one wants to choose central line, i.e. center point at each point on line. Since the central point is going to be the highest intensity point, it explains the purpose of the step. Additionally, to make sure one does not hit on noise, one chooses to process only those points, for which, there is only one signal peak in 1 pixel window on either side.

A.XIV.5 Accumulate all the 'good' points obtained by step B.IV.4, and using these points to perform least squares line fitting to obtain the line equation.

A.XV Recalculate BB centers and establish correspondence. Since line equations have been obtained, one can now recalculate the BB centers by projecting the BB centers initially located on the line, then looking along the line for a minimum (or maximum) intensity point along the line by doing interpolation. Correspondence of lines is arrived at by looking at the number of BB centers that lie on a particular line.

B Ellipse segmentation: First the noise is removed from the image by morphological processing, so that the image is left with only ellipse segments. Then, one uses the ellipse segments in an ingenious variation of Hough transform to perform ellipse segmentation.

B.I Perform morphological processing (*top-hat*) transform with a structuring element of disk shape and radius 1, followed by *area-opening* to get rid of most of the noise, to obtain a new image.

- Note: The description of the *top-hat* and *area-opening* transforms has been previously provided. Now one will have an image, which contains only lines, ellipses and some noise, everything else will be eliminated.

B.II Since line equations are known at this stage, one can get rid of the lines as well. Now one is left with the image, which consists of only ellipse segments.

B.III Perform morphological closing, which may or may not result in connecting the ellipse segments, which are close to each other. Call this as morphologically reduced image.

B.IV Label the image.

B.V Find strongest ellipse and the segments contributing to it.

- B.V.1 Take 2 segments/regions at a time; get an ellipse equation using least squares fitting.
- B.V.2 Determine the center of ellipse; see if the center lies close to any other center found earlier, and if the lengths of major axis and minor axis are comparable to that ellipse. If yes, add vote strength to that 'center-containing-region'. If no, declare a new region around the center found.
- B.V.3 Do step C.V.1-C.V.2 for all possible 2-segment combinations.
- B.V.4 Determine the region with the highest vote and for all the centers that lie within the region, record the segments responsible.
- B.V.5 From the segments obtained, fit an ellipse. Record it.
- B.VI Eliminate all the segments obtained above from the morphologically reduce image obtained after step C.III.
- B.VII Re-label the image obtained after step C.VI.
- B.VIII Perform step C.V, obtain 2<sup>nd</sup> ellipse.
- B.IX Establish correspondence of the ellipse by looking at their centers.

### 3.6.3 Applying to the proposed

Since the main key of this method is the FTRAC, The result from the FTRAC is the position and orientation of the FTRAC with respect to the C-arm. Applying the

knowledge from 3.1.10 to recover the distal hole pose with respect to the FTRAC and C-arm as shown in Figure 3.24. Error checking of the FTRAC (size 20 mm), the experimental setup, and results are shown in Chapter 4.

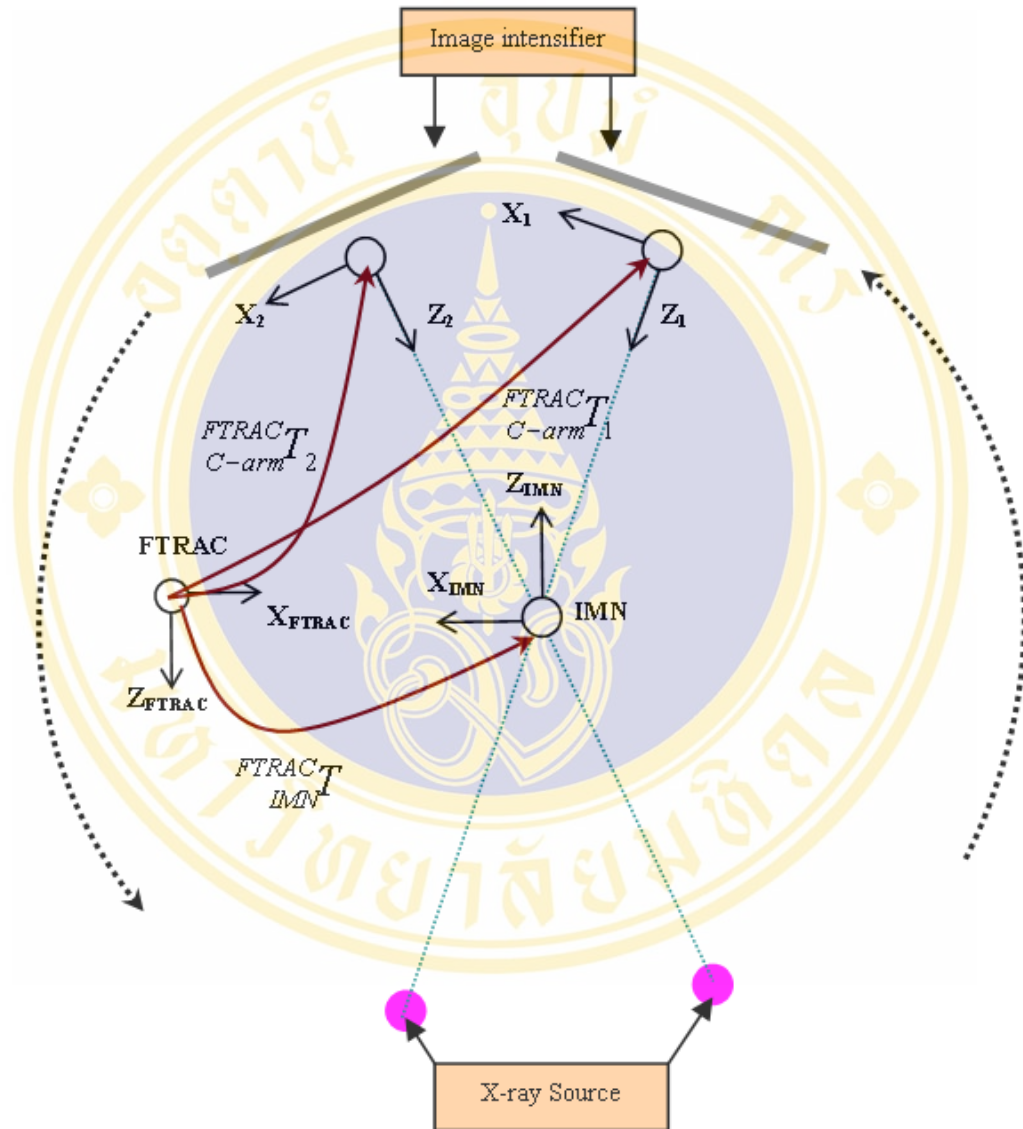


**Figure 3.24** Diagram of the Spatial Transformation

### 3.7 Chapter summary

This chapter discusses related theoretical reviews and methods developed in this Master thesis. Methods in sections 3.4 – 3.6 will show experiments and their results in Chapter 4.

## CHAPTER IV

### EXPERIMENTAL RESULTS

There are three main methods presented in the previous chapter, which are 1) Recovery of distal holes axis using X-Y span of distal hole's projection images, 2) Recovery of distal holes axis using interested area of distal hole's projection images, and 3) Recovery of distal holes axis using additional fiducial, Fluoroscope tracking (FTRAC.) The experiment and results are included in this chapter. The assumptions made are as followed:

- Nail rotates about X-axis only.
- Nail has a cylindrical shape.
- The distal-holes are in circular shape.
- Diameters of the nail and the distal-holes are previously known to have the IMN diameter of about 12 mm, with the length of 380 mm, and the distal hole diameter of about 5-6 mm.

#### **4.1 Recovery of Distal holes axis using X-Y span of distal hole's projection images**

In order to test the algorithm, simulations were done in stages. The simulation started with pure rotation about X-axis, pure rotation about Y-axis, combination of X-Y rotations, and combination of X-Y-Z rotations. In this case the diameter of the IMN of about 12 mm, and the distal hole of about 6 mm. To simplify the problem of the IMN's shape, the assumption is that the IMN is in a circular shape. Simulations and collecting the interested data related to the rotation angles " $\theta$ ", were done for all stages.

#### 4.1.1 Rotation about X-Axis

In this subsection, a set of simulation results for pure rotation about X-axis is illustrated in Figure 4.1. Figure 4.1 shows four cases of pure X-rotation angle:

- 1)  $X = 19^\circ$  2)  $X = -6^\circ$  3)  $X = -19^\circ$  and 4)  $X = 10^\circ$ .

#### 4.1.2 Rotation about Y-Axis

In this subsection, a set of simulation results for pure rotation about Y-axis is illustrated in Figure 4.2. Figure 4.2 shows four cases of pure Y-rotation angle:

- 1)  $Y = -24^\circ$  2)  $Y = -21^\circ$  3)  $Y = -8^\circ$  and 4)  $Y = 13^\circ$ .

#### 4.1.3 Rotations about X- and Y-Axes

In this subsection, a set of simulation results for rotations about X- and Y-axes is illustrated in Figure 4.3. Figure 4.3 shows four cases of X-Y Euler rotation angles:

- 1)  $X = 0^\circ$   $Y = 0^\circ$   $Z = 0^\circ$  2)  $X = -15^\circ$   $Y = -15^\circ$   $Z = 0^\circ$   
3)  $X = -8^\circ$   $Y = -8^\circ$   $Z = 0^\circ$  and 4)  $X = 8^\circ$   $Y = 8^\circ$   $Z = 0^\circ$ .

#### 4.1.4 Rotations about X-, Y- and Z-Axes

In this subsection, a set of simulation results for rotations about X-, Y-, and Z-axes is illustrated in Figure 4.4. Figure 4.4 shows four cases of X-Y-Z Euler rotation angles:

- 1)  $X = 6^\circ$   $Y = -16^\circ$   $Z = -30^\circ$  2)  $X = 21^\circ$   $Y = -2^\circ$   $Z = -30^\circ$   
3)  $X = 11^\circ$   $Y = 3^\circ$   $Z = -30^\circ$  and 4)  $X = 12^\circ$   $Y = -5^\circ$   $Z = -30^\circ$ .

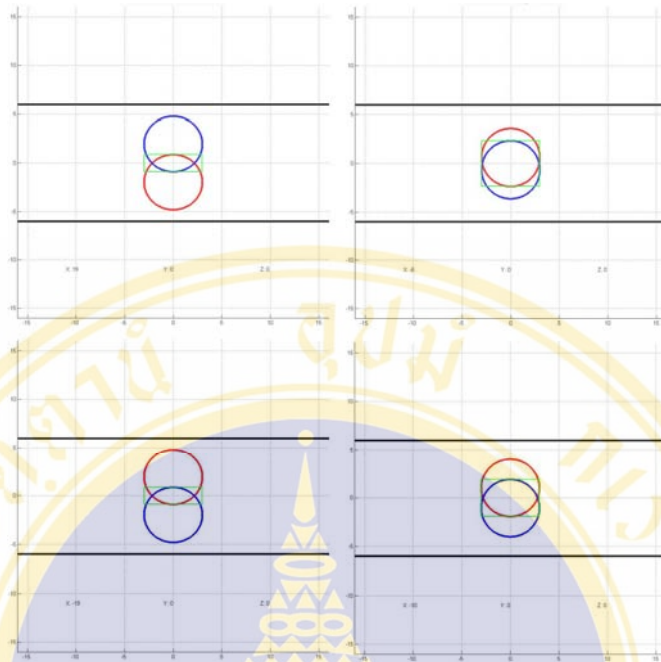


**Figure 4.1** Simulation Results for Rotation about X.

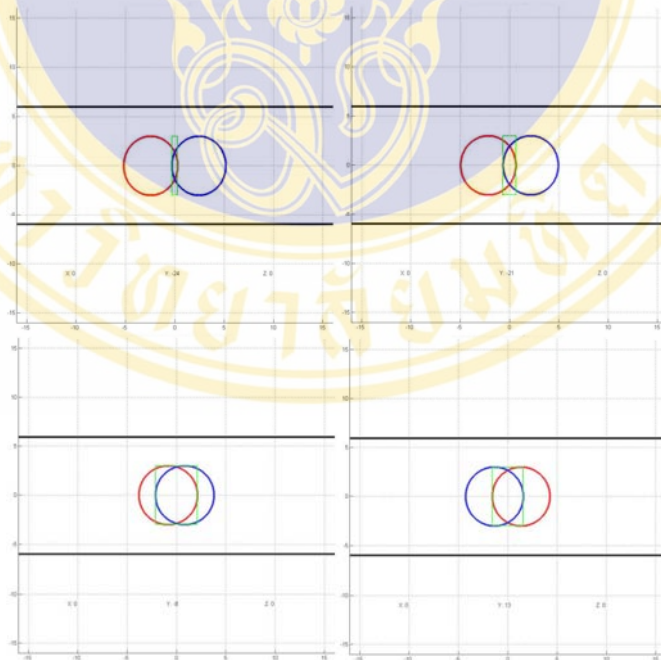


**Figure 4.2** Simulation Results for Rotation about Y.

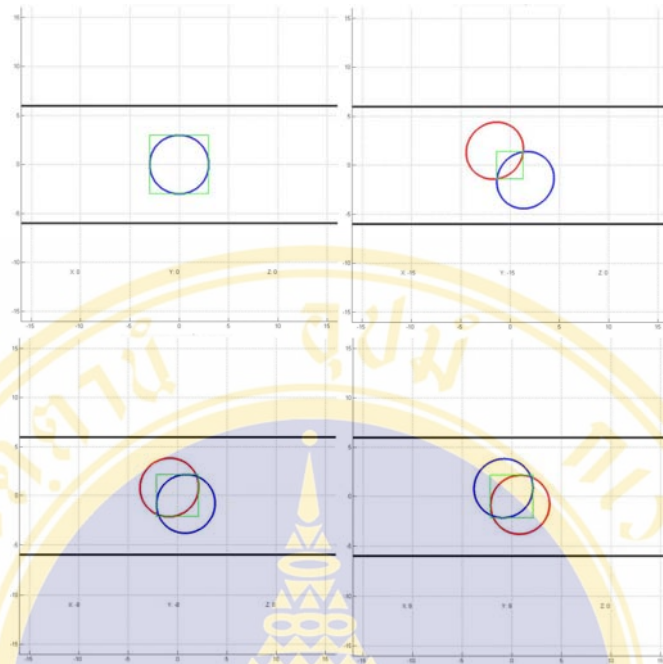


**Figure 4.3** Simulation Results for Rotation about X-Y.

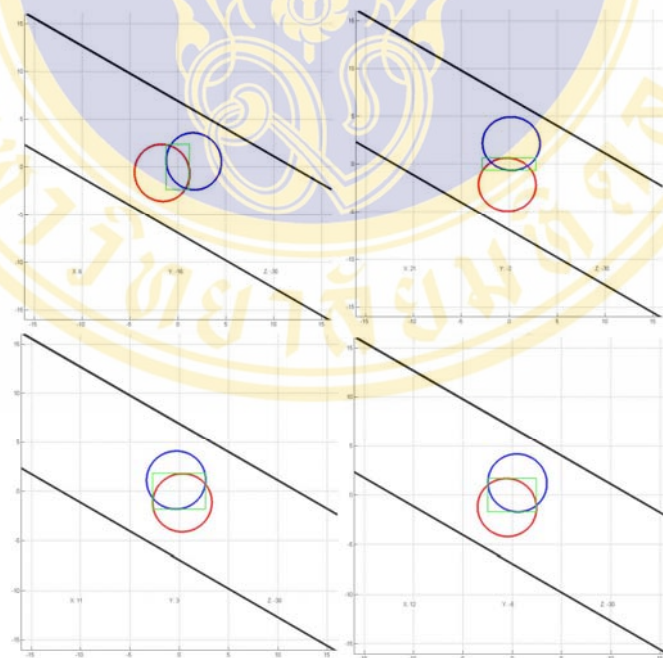


**Figure 4.4** Simulation Results for Rotation about X-Y-Z axes.

### Experimental Result of the simulation

The result from the simulation is the possibility of the nail rotation in each axis. The simulations show that for the pure axis rotation, the IMN can rotate from -25 to 25 degrees. If one combines X-Y-Z rotation (3 axes rotation), one can see the crossed section area of the IMN to be from -19 to 19 degrees. This information is applied to the next method.

#### 4.2 Recovery of distal holes axis using interested area of distal hole's projection images

Conventional closed nailing by rotating the fluoroscope (C-arm) system. There is no reality system available for producing images as in the case of closed intramedullary femoral nailing. Therefore, one proposes to rotate the intramedullary nail instead of the camera (manual C-arm fluoroscope) as illustrated in Figure 3.16; the digital compact camera is on the top view (z-axis) and the product of the successive imaging system is shown in Figure 4.5 (b). The experiment setup is shown in Figure 4.6.



**Figure 4.5** a) Fluoroscope (X-ray) imaging and b) Image taken by a digital camera.

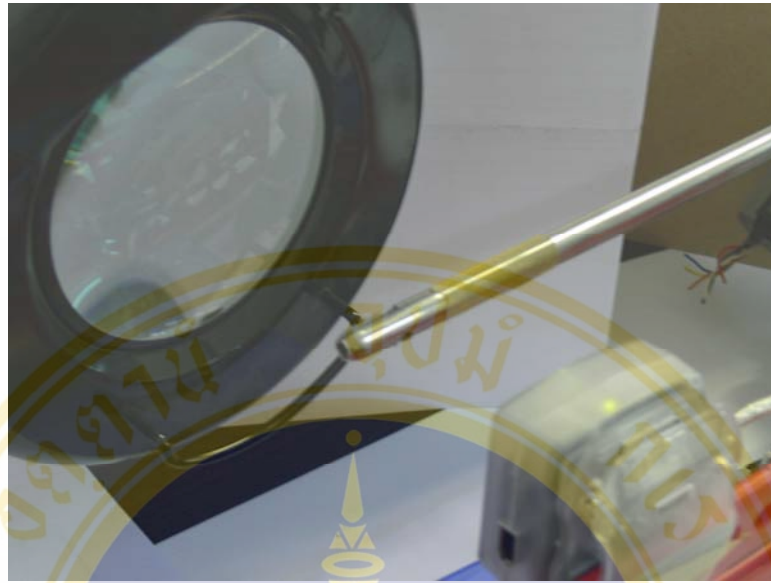


**Figure 4.6** The experiment setup for this method.

The experimental set up can be separated into 2 steps.

*Step I: Image preparation*

- To prepare database for Part I: Images of IMN rotation at 0, 5, 10, 15 and 20 degrees are taken for 10 data sets. This information is to generate the “Tool Curve.”
- To prepare database for Part II: Images of IMN rotation at 2, 4, 6, 8, 12, 14, 16 and 18 degrees are taken for 15 data sets. This information is used to determine the errors of the proposed algorithm.

*Step II: Data analysis*

Compute average areas of the distal hole’s images using MATLAB. Construct the Tool Curve by plotting graph of area vs. rotational angle. It has been found that quadratic curve fitting technique is a proper selection. The equation is shown as follows:

$$\theta = ax^2 + bx + c,$$

where  $a$ ,  $b$  and  $c$  are constant values.

$x$  is the input which is the computed area of an unknown image

$\theta$  is the output which is the rotation angle in degree.

Figures 4.7 (a), (b) and (c) show examples of a series of image processing steps during the distal hole’s area determining process.

Average computed areas at different angles are plotted in a graph of area vs. rotational angle. The “Tool Curve” is generated as shown in Figure 4.8. Table 4.1 shows experimental results from the algorithm used.

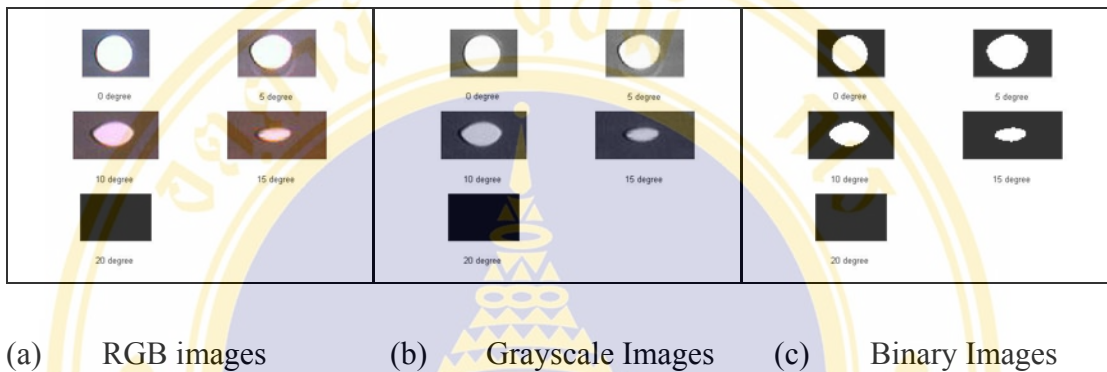


**Figure 4.7** One data set of distal hole images at 0, 5, 10, 15 and 20 degrees

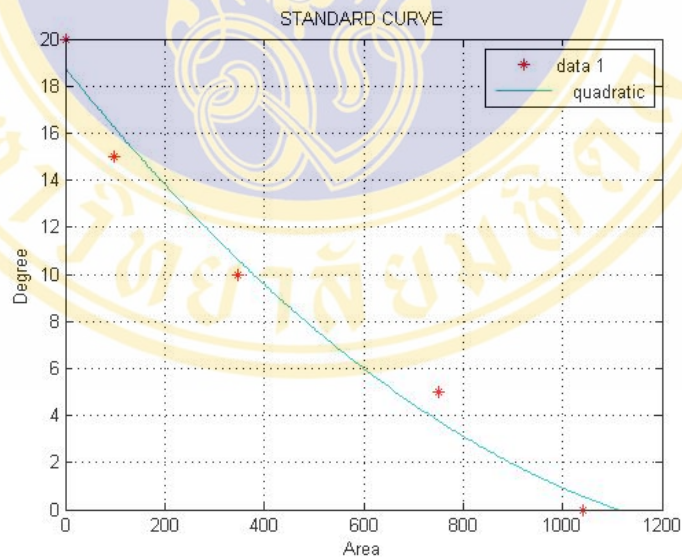


**Figure 4.8** Tool Curve

**Table 4.1** Distal hole's rotational angle recovered from proposed algorithm.

<b>Expected Rotational Angle</b>	<b>Average Predicted Angle</b>
2°	2.2854
4°	4.1335
6°	6.2041
8°	8.5826
12°	12.8454
14°	14.9214
16°	16.1414
18°	18.2370

### **Experimental Result**

This part discusses an implementation on recovering of IMN distal hole's orientation using a new algorithm which uses the area of distal hole's projected images. Only two to three x-ray images are required during the hole's orientation recovery. In order to demonstrate the algorithm, a set of implementations is done by using MATLAB in an experimental setup to simulate acquiring x-ray images. The experimental results shows the positive potential of the new algorithm to be used in a real operation. The analyzed error of prediction is approximately 5.48% in average. According to the first method, the simulation gives the limitation of the IMN rotation (In case one needs to see the crossed section area of the distal hole.) This information helps the implementation of the experimental setup. Table 4.1 shows the result of the rotation angle from the proposed algorithm compared to the known information from experiment setup. One rotates the IMN with known parameters which are IMN's and distal hole's diameters, and the rotation angle.

### 4.3 Recovery of distal holes axis using additional fiducial, Fluoroscope Tracking (FTRAC)

The experiment is divided into two parts which are the error checking of the FTRAC diameter 20mm and the pose recovery of the distal hole axis. These two parts follow the step on the Graphic User Interface (GUI.)

#### 4.3.1 Instruments

##### 1) C-arm fluoroscope

OEC 9600. Donated by GE. Main use as shown in Figure 4.9.



**Figure 4.9** C-arm models OCE 9600

##### 2) Tracking systems

FTRAC diameter size is 20 mm as shown in Figure 4.10.

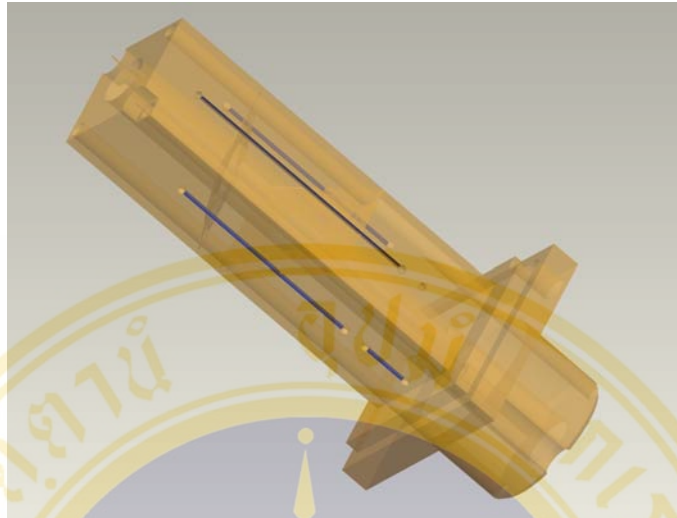


**Figure 4.10** Fiducial “FTRAC” with the diameter of 20 mm

3) Image acquisition

- a) Download from C-arm interface to floppy. Available: OEC 9600 only. (Best image quality but slow)
- b) Capture with Firewire frame grabber. This method is not available.
- c) Capture with USB frame grabber. Available: OEC 9600, good image quality but not as good as floppy drive, and faster than floppy drive as shown in Figure 4.11



**Figure 4.11** Hauppauge WinTV USB, Frame grabber

- 4) Calibration phantom: Designed by Iulian Iordachita and Goutami [Johns Hopkins University] as shown in Figure 4.12.

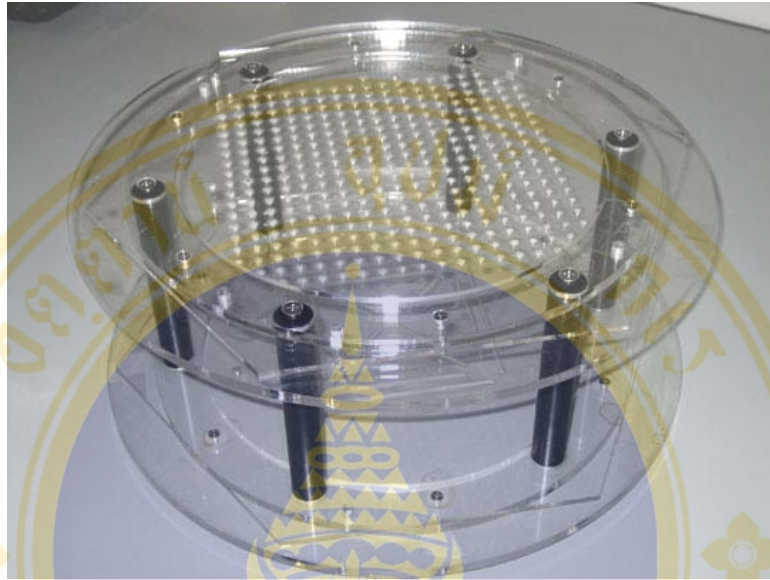


**Figure 4.12** Calibration Phantom made by Iulian, designed by Gouthami

- 5) Dressing and batch: during the experiment one needs to wear the lead suit and clip the batch with has one's name on it. The Radiation Department has to bring it back and check the exposure rate of each batch every month. Figure 4.13 shows the lead suit and Figure 4.14 shows the batch.
- 6) Rotary Positioning Stage: Manually driven for rotating the FTRAC as shown in Figure 4.15.



**Figure 4.13** Lead Apron Radiation Protection and Thyroid Collar.

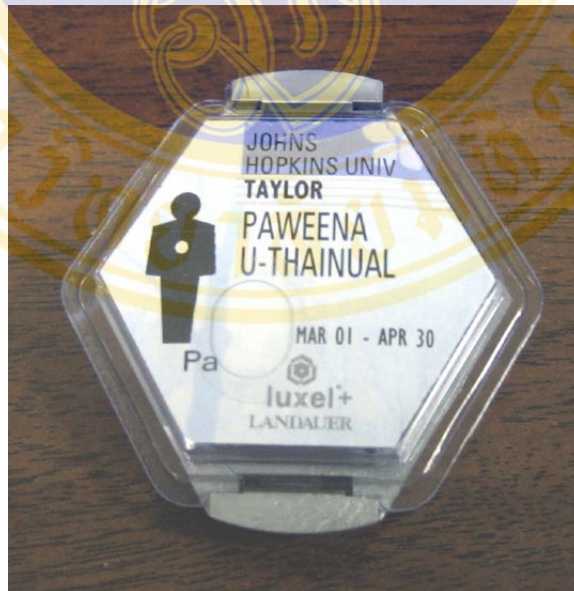


**Figure 4.14** The batch for measuring the x-ray exposure. This batch will be changed every month.

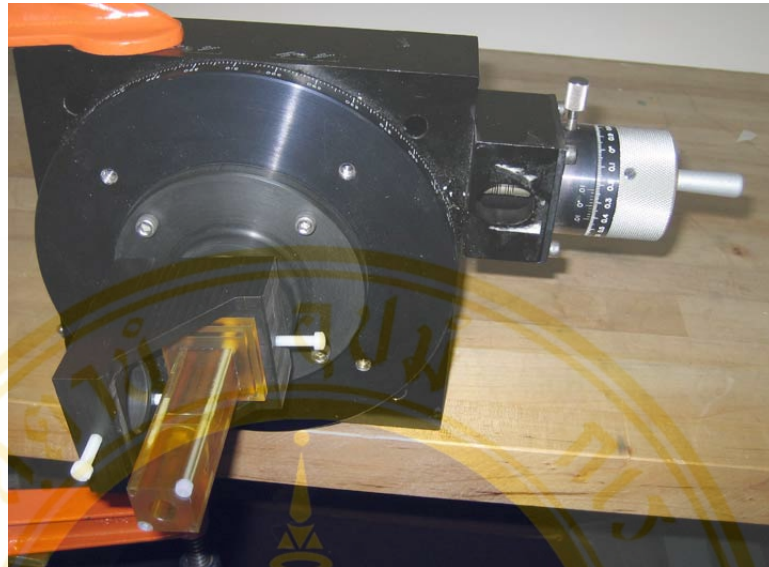


**Figure 4.15** Manual Rotary stage

### **4.3.2 FTRAC residual error checking**

#### **4.3.2.1 Procedure**

- 1) Taking the images
  - Wear the lead apron radiation protection before using the x-ray machine.
  - Put the batch on the suit for measuring of the x-ray exposure to the user.
  - Turn on the C-arm and annotate the name.
  - Put the FTRAC in the rotary positioning stage as shown in Figure 4.16. Make sure that FTRAC and the rotary stage are fixed rigidly to each other.

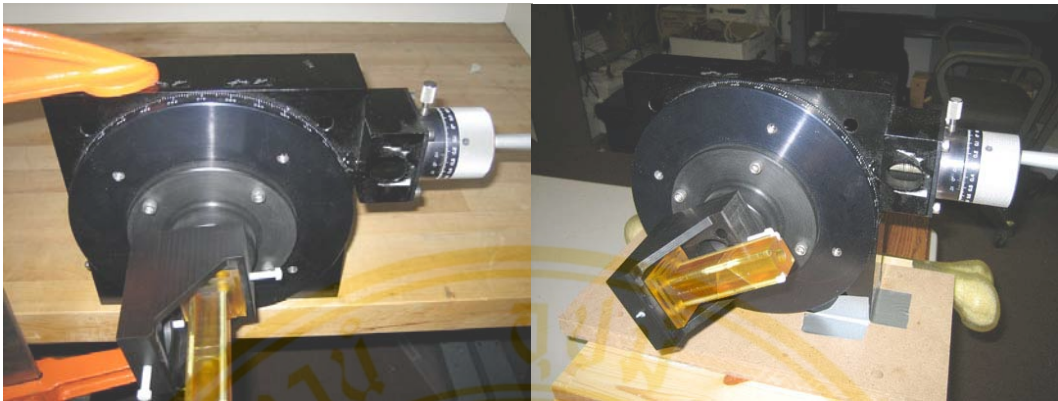


**Figure 4.16** FTRAC 20 mm on the Rotary Positioning stage

- Taking the x-ray image of the FTRAC every 5 degrees as shown in the table below. The calibration image will be taken after or before one rotates the FTRAC in each axis (Y-Z) (one needs just only 1 image from each axis). The example of the x-ray images in Y-, and Z-axis are shown in Figure 4.17 and 4.18 respectively.

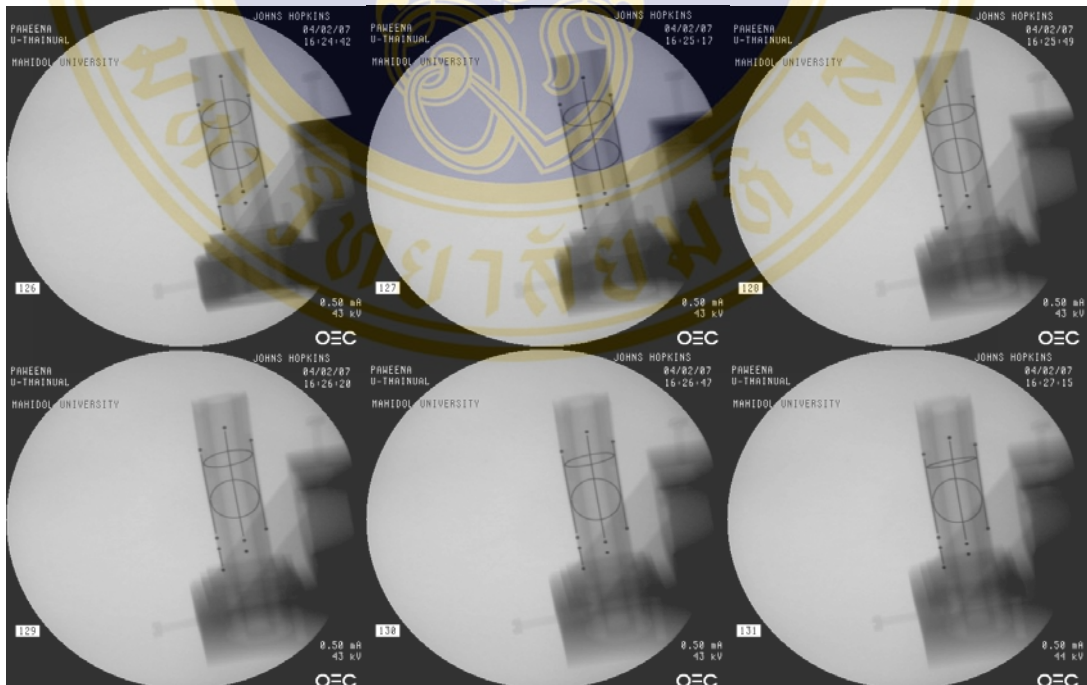


**Figure 4.17** The x-ray images of FTRAC rotating about Y-axis



**Figure 4.18** The x-ray images of FTRAC rotating about Z-axis

## 2) Calibration

- Attach the calibration phantom to the Image intensifier on the C-arm and taking the image as shown in Figure 4.20.
- The calibration image is shown in Figure 4.19.

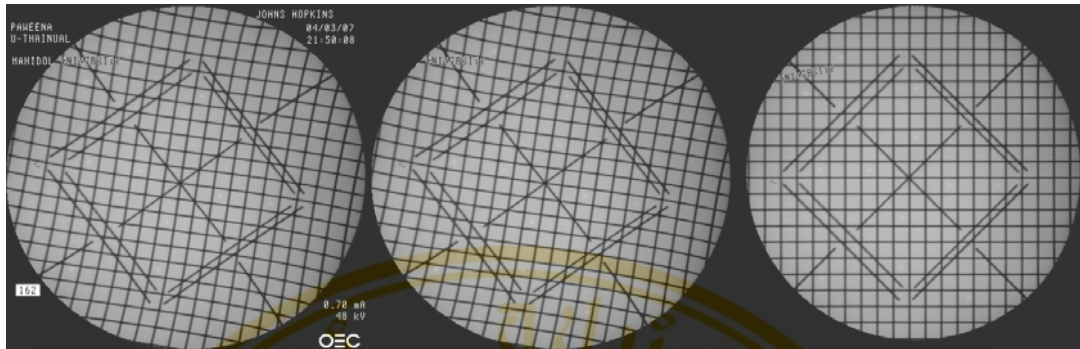


**Figure 4.19** a) Calibration image before dewarping, b) Clean image before dewarping, c) Dewarped image

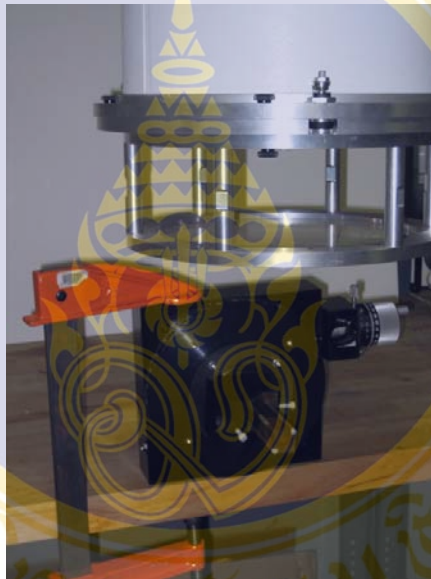


**Figure 4.20** C-arm with Calibration phantom.

### 3) Image Processing

- Process the calibration image with MATLAB command
  - i. Load the image from file.
  - ii. Remove OEC and others label from image (It's applicable if using floppy-disk transfer, if not using the oval mask, the image is captured with the frame grabber.)
  - iii. Load the dewarps grid geometry to memory (assuming the following script is included in the MATLAB path.)
  - iv. Define the parameters of the dewarp function and sampling.

- v. Dewarp the calibration image and obtain the dewarp parameters, which are the focal length and the origin of the image.
- vi. The output of the image size is [480 480] and output in mm/pixel is [0.45 0.45].
- vii. Apply the output parameters from dewarping the calibration image to all the images in (i.) The dewarped image is compared with the original image is shown in the Figure 4.21.

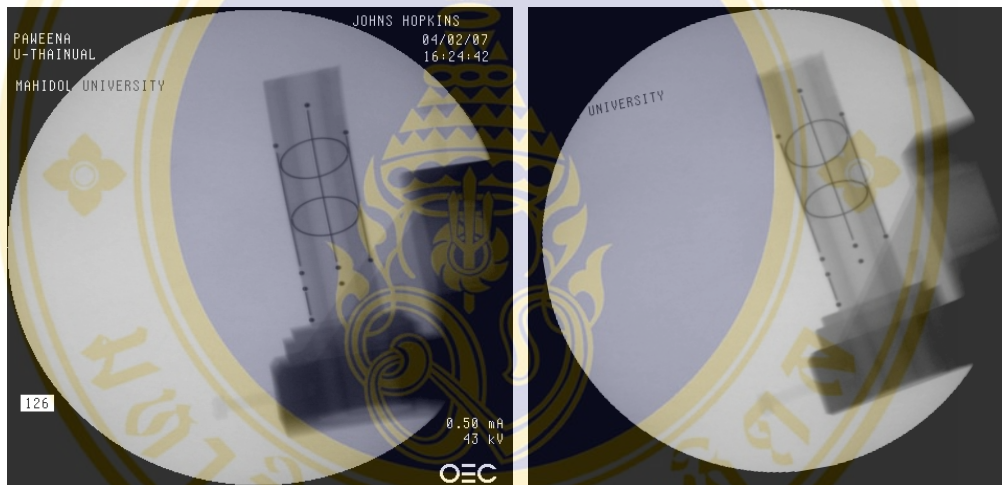


**Figure 4.21** Comparing the original image from C-arm and the dewarped image

#### 4) Finding the residual error using the MATLAB program

- Create the folder for using Graphic User Interface (GUI.) This GUI is developed by Anton Duet, Ameet Jain. The difference of the GUI in use is put in the equation of the FTRAC because the FTRAC used has some part of the design changed. The algorithm thus used to determine the points, lines and curves has to change as well.
- Create the folder in drive C as followed:
  - i. “C:\devel\ruf\data\calibrations\yyyy-mm-dd-name\generated-data”
  - ii. “C:\devel\ruf\data\calibrations\yyyy-mm-dd-name\raw-data”

- iii. *“C:\devel\ruf\data\patients\yyyy-mm-dd-name\processed-data\intra-op\fluoro\video\batch-nnn”*
- iv. *“C:\devel\ruf\data\patients\yyyy-mm-dd-name\raw-data\intra-op\fluoro\video\batch-nnn”*
- v. Open MATLAB program and open existing GUI as followed:

*“P:\Research\ruf\matlab>Main\_GUI\rufMainGUI.fig”*

- Follow the step of the GUI through the FTRAC button, which are Calibration, Image acquisition, Mask and dewarp image, Segmentation the FTRAC as shown in Figure 4.22. The results are the pose of the FTRAC with respect to the C-arm and the residual error of the FTRAC. The residual error is calculated by finding the norm of the distance, which is the difference from pose of the FTRAC in 3-D and pose of the FTRAC from the algorithm.

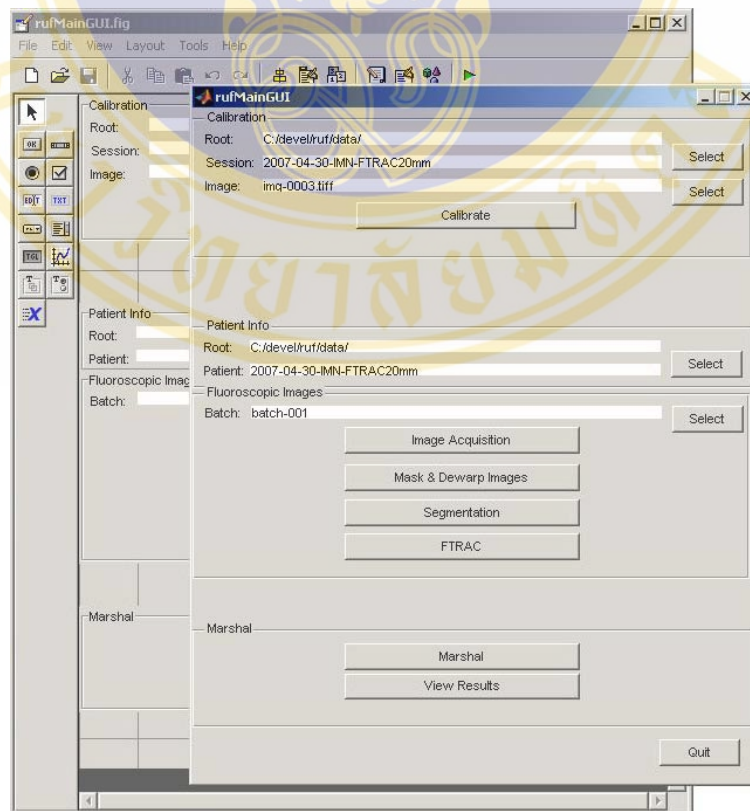


**Figure 4.22** GUI for determining the FTRAC pose with respect to C-arm

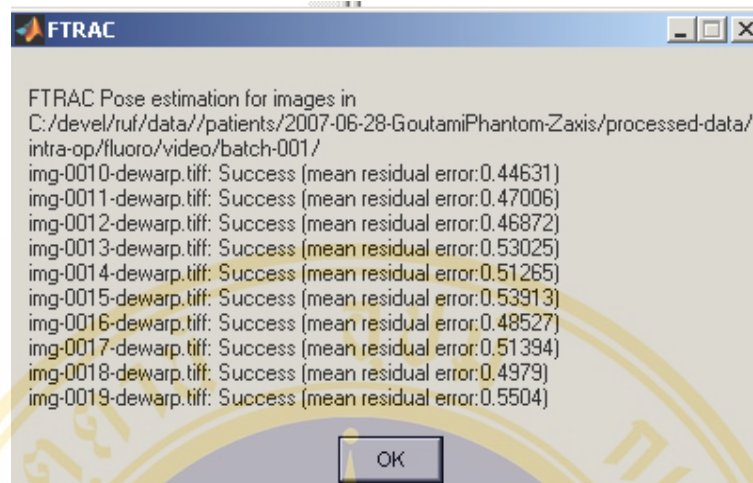


**Figure 4.23** GUI shows the residual error of the FTRAC

### 4.3.3 Apply the FTRAC to find the distal hole's axis

To simplify the problem, the FTRAC is assumed to be fixed rigidly to the IMN. The experiment setup is shown in Figure 4.24. Put the FTRAC on the rotary stage and fix to the table. The IMN is fixed to the table. During the experiment, FTRAC and IMN are fixed rigidly and to be unmovable.

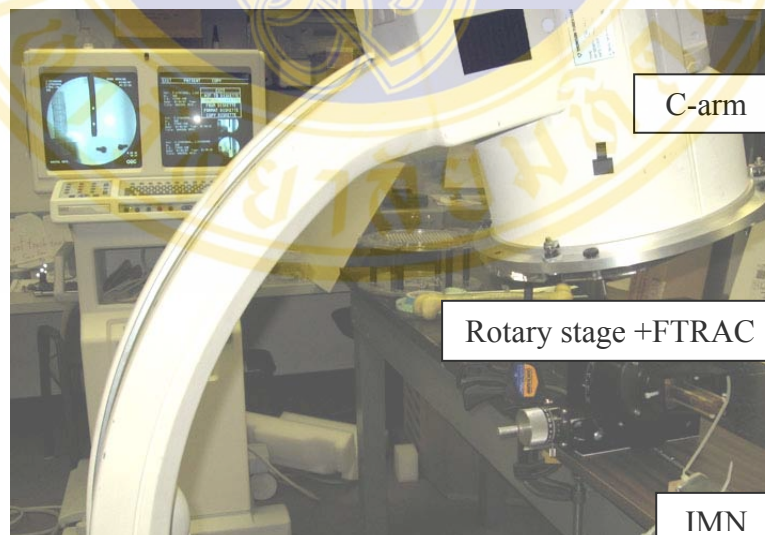


**Figure 4.24** Experiment Setup

#### 4.3.3.1 Procedure

- 1) Put the FTRAC on the rotary stage.

- 2) Fix the IMN to the table near to the FTRAC which known distance.
- 3) Set up the C-arm which are annotating the name and set the position of the C-arm to be closed to the FTRAC and IMN. Make sure that one can see both FTRAC and C-arm in the x-ray image.
- 4) Connect the C-arm to the PC with the winTV encoder as shown in Figure 4.26. The winTV (Figure 4.11) is connected to the PC and C-arm controlling part. The picture from C-arm will appear in the monitor of PC as well as shown in Figure 4.25.
- 5) Rotate the C-arm to follow the Path in Figure 4.27, with the (X,Y, FTRAC) representing the rotation angle in each axis. The C-arm rotates about X-, Y- axes. The FTRAC rotates about Z-axis. The results of the example of x-ray images in difference viewing of the C-arm are shown in Figure 4.28



**Figure 4.25** Connect the C-arm to the computer with the TV encoder



**Figure 4.26** a) The TV encoder is connected to the PC monitor, which makes less time for saving the images from C-arm b) the TV encoder is connected to the C-arm.

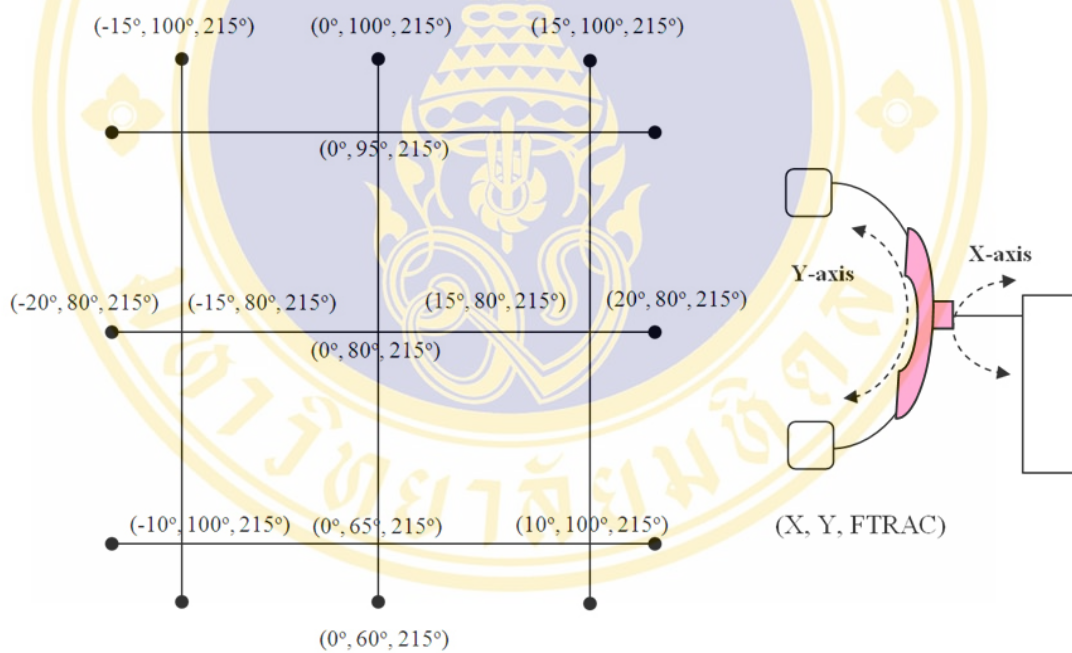


**Figure 4.27** Diagram of rotating path of the C-arm during the experiment.

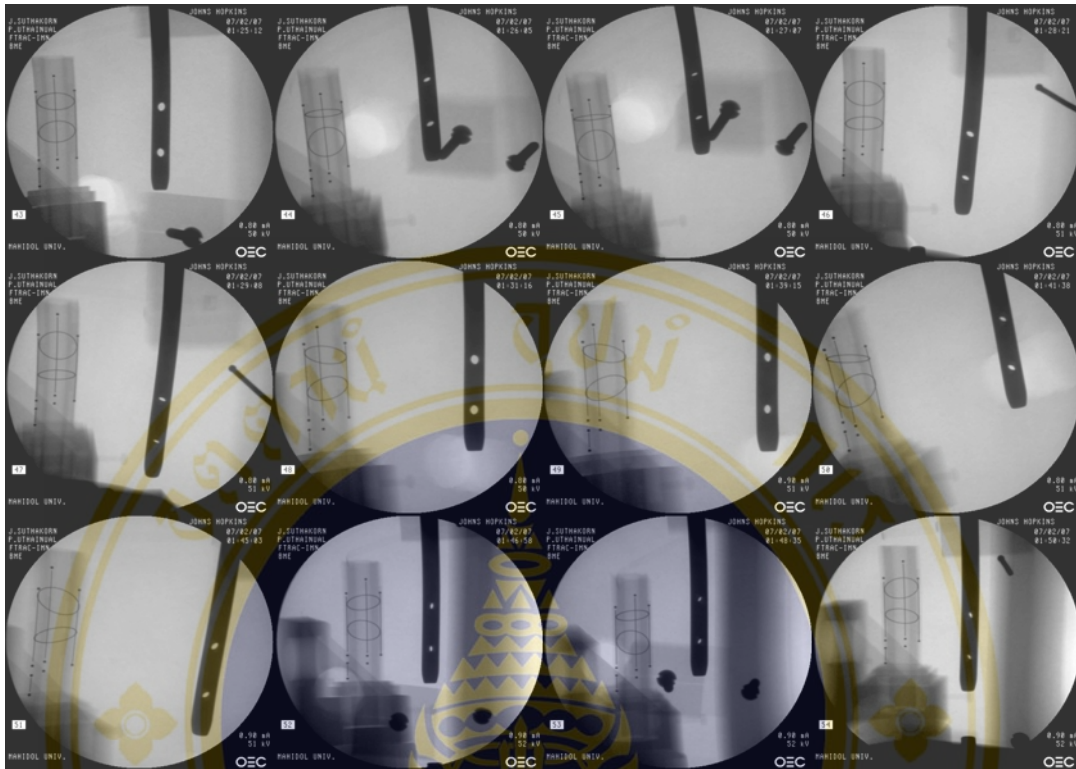


**Figure 4.28** A dataset of x-ray images in the difference viewing of the C-arm. The FTRAC and IMN are fixed without moving.

- 6) Then follow the procedure in subsection 4.3.2 to find the pose of the FTRAC with respect to C-arm. The steps from GUI are shown in figure 4.29 to 4.32
- 7) Apply the information of the FTRAC pose to determine the pose of the distal hole axis. This step requires image processing.
- 8) The image processing requires at least 2 images to find the Transformation of the FTRAC with respect to the projection image of the distal hole.

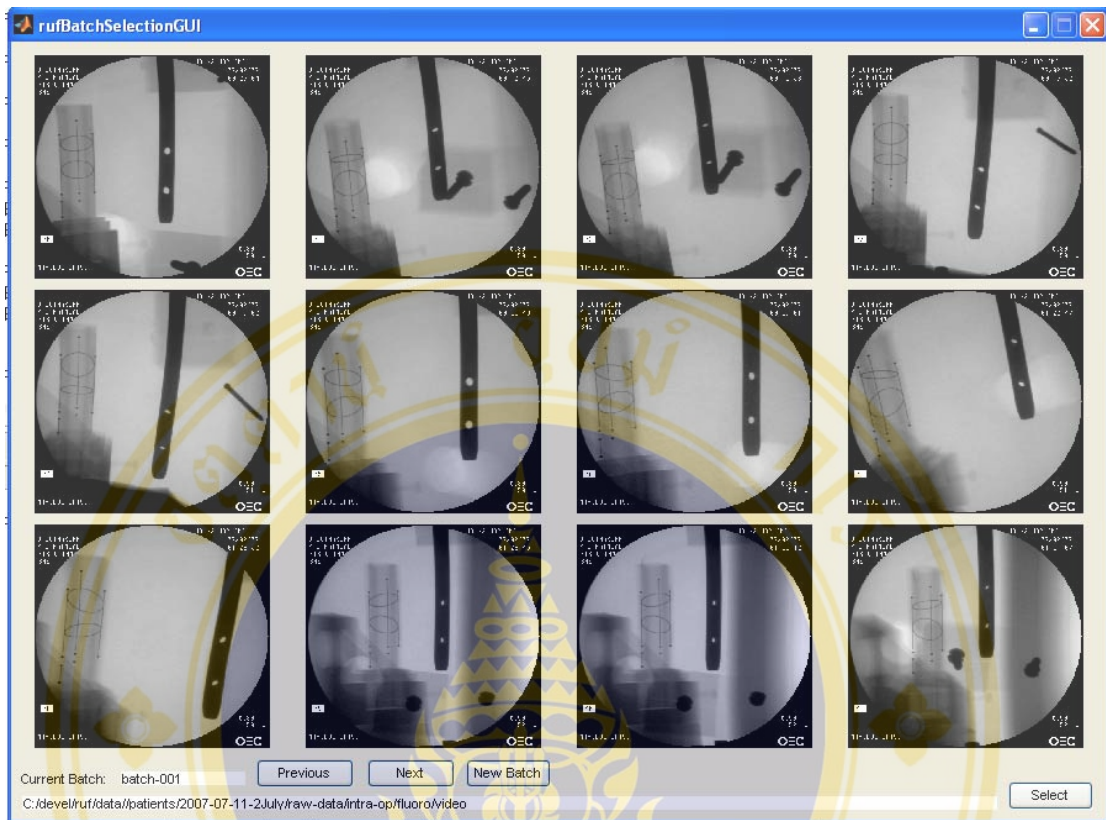


Figure 4.29 Acquiring the images and selecting the images from the C-arm

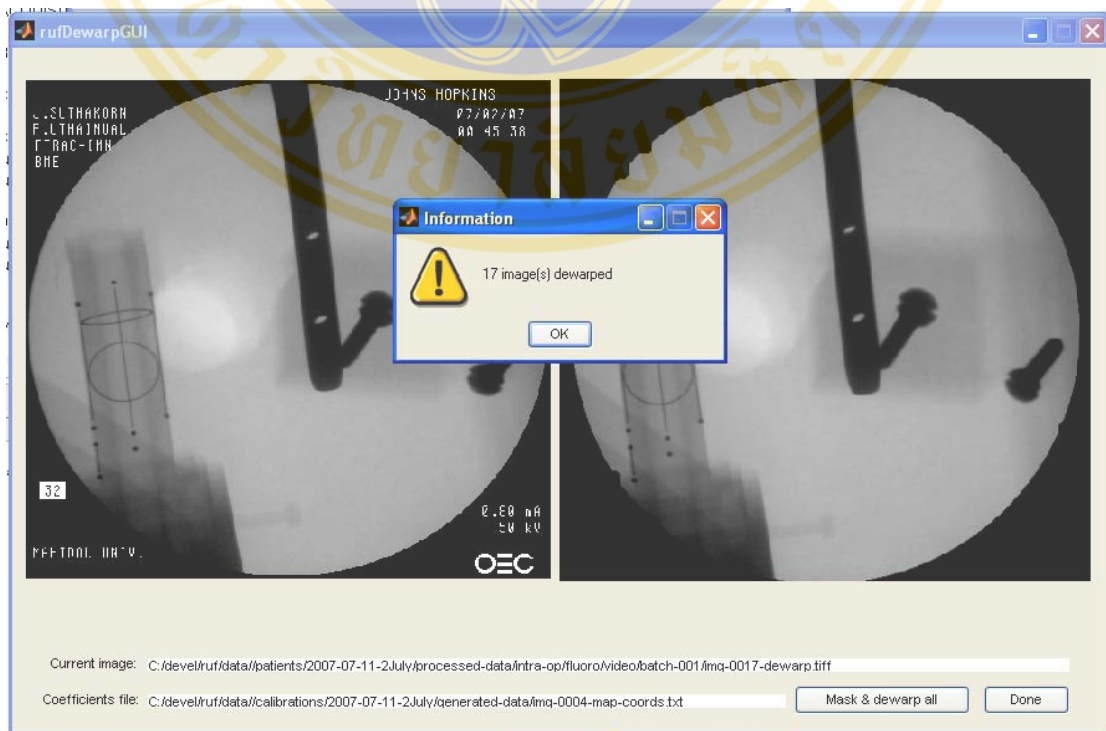


Figure 4.30 Dewarping the images

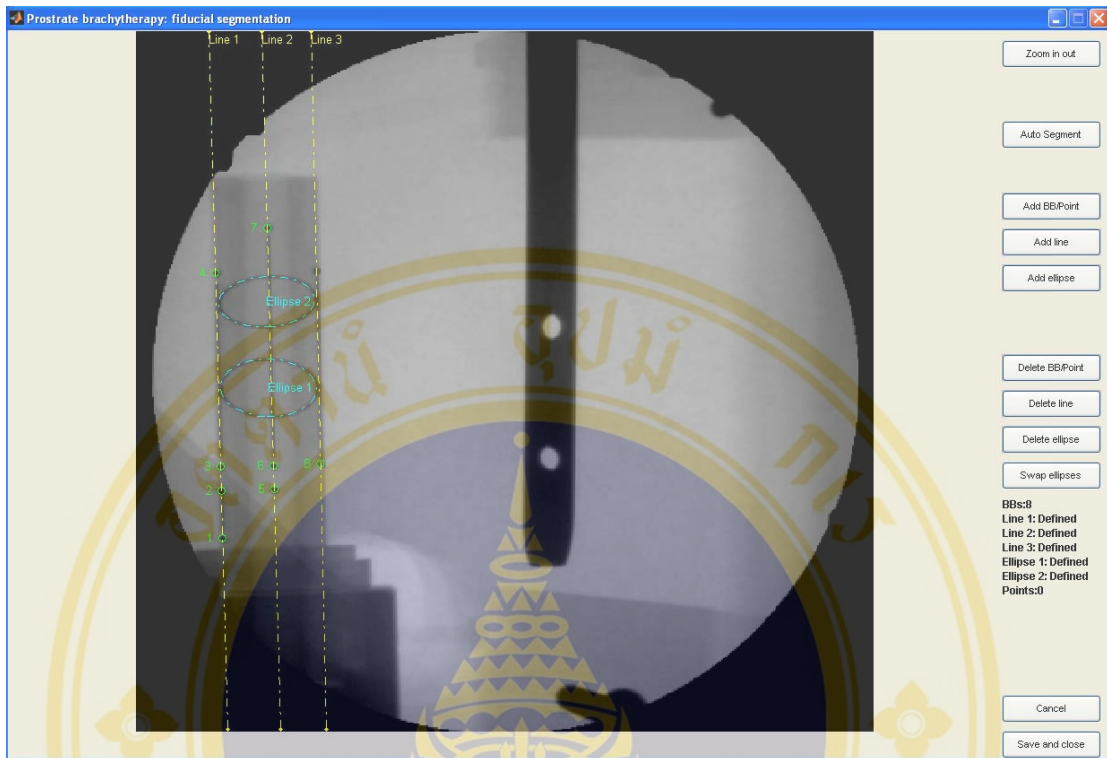


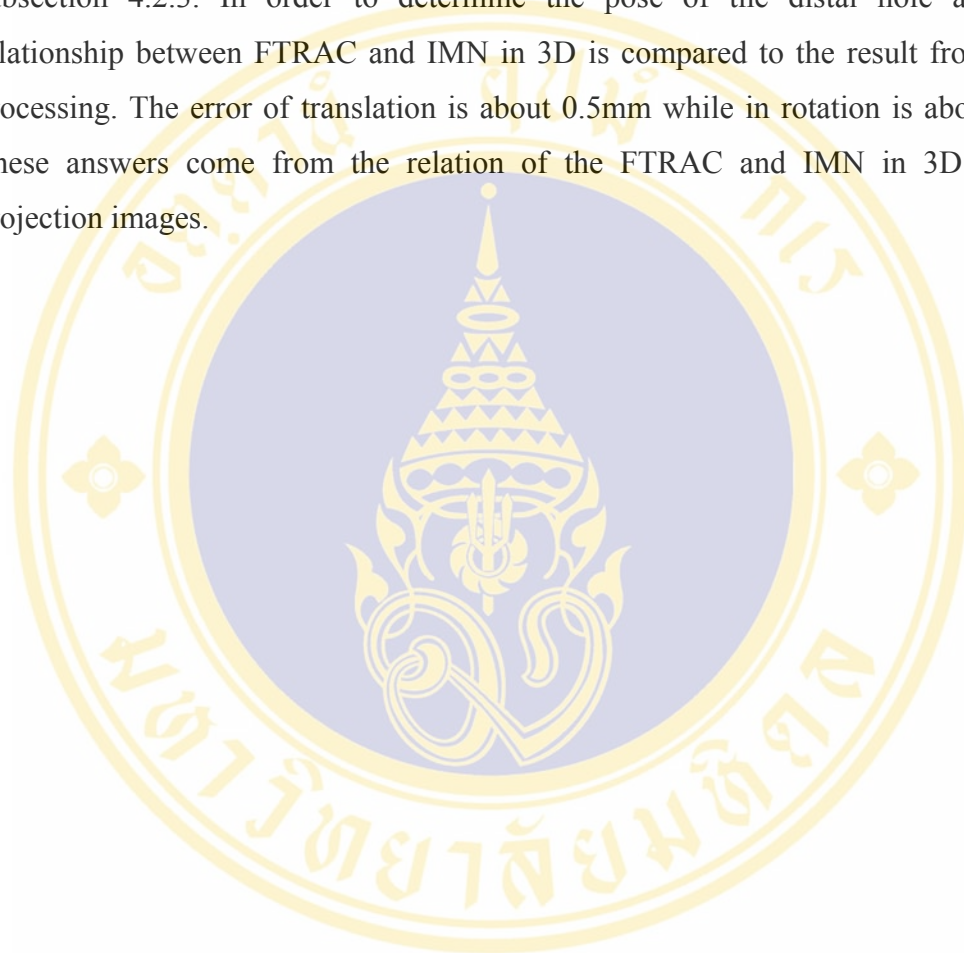
Figure 4.31 Segmentation of the FTRAC lines, points, and ellipses.

File	Edit	Format	View	Help
Pose_img-0001-dewarp - Notepad				
<pre> -5.7631902e-002 -1.5934423e-002 -9.9821073e-001 2.6617415e+001 8.9895752e-001 -4.3572379e-001 -4.4946045e-002 -3.8863359e+001 -4.3422798e-001 -8.9989377e-001 3.9435900e-002 8.6589151e+002 0.0000000e+000 0.0000000e+000 0.0000000e+000 1.0000000e+000                     </pre>				
Pose_img-0002-dewarp - Notepad				
<pre> -6.0344655e-002 -1.8728301e-002 -9.9800189e-001 2.6586944e+001 9.3561380e-001 -3.4845905e-001 -5.0014573e-002 -3.8800512e+001 -3.4782410e-001 -9.3676445e-001 3.8610480e-002 8.6781569e+002 0.0000000e+000 0.0000000e+000 0.0000000e+000 1.0000000e+000                     </pre>				
Pose_img-0003-dewarp - Notepad				
<pre> -5.9932565e-002 -2.1474850e-002 -9.9797140e-001 2.6552394e+001 9.6945285e-001 -2.3946833e-001 -5.3066900e-002 -3.8840133e+001 -2.3784294e-001 -9.7066665e-001 3.5170803e-002 8.7332409e+002 0.0000000e+000 0.0000000e+000 0.0000000e+000 1.0000000e+000                     </pre>				
Pose_img-0004-dewarp - Notepad				
<pre> -5.4950639e-002 -3.0176693e-002 -9.9803296e-001 2.6572697e+001 9.9072554e-001 -1.2605025e-001 -5.0737023e-002 -3.8997478e+001 -1.2427123e-001 -9.9156477e-001 3.6823362e-002 8.7556031e+002 0.0000000e+000 0.0000000e+000 0.0000000e+000 1.0000000e+000                     </pre>				
Pose_img-0005-dewarp - Notepad				
<pre> -5.082548e-002 -2.7614124e-002 -9.9832571e-001 2.6581921e+001 9.9865762e-001 -1.1399993e-001 -5.0527117e-002 -3.8995623e+001 -9.9856441e-001 -9.991365e-001 2.8156457e-002 8.8036643e+002 0.0000000e+000 0.0000000e+000 0.0000000e+000 1.0000000e+000                     </pre>				
Pose_img-0006-dewarp - Notepad				
<pre> -4.9394295e-002 -4.1226290e-002 -9.9792815e-001 2.6478723e+001 9.9149085e-001 1.1846177e-001 -5.3969348e-002 -3.8610201e+001 1.2044139e-001 -9.9210242e-001 3.5024154e-002 8.7771890e+002 0.0000000e+000 0.0000000e+000 0.0000000e+000 1.0000000e+000                     </pre>				
Pose_img-0007-dewarp - Notepad				
<pre> -4.8125803e-002 -3.7769921e-002 -9.9812692e-001 2.6614124e+001 9.7448636e-001 2.1754837e-001 -5.5218151e-002 -3.8666259e+001 2.1922647e-001 -9.7531848e-001 2.6336582e-002 8.7906751e+002 0.0000000e+000 0.0000000e+000 0.0000000e+000 1.0000000e+000                     </pre>				
Pose_img-0008-dewarp - Notepad				
<pre> -3.4674526e-002 -5.4140794e-002 -9.9793109e-001 2.6481376e+001 9.9999999e-001 1.0757319e-002 -3.8406746e+001 0.0000000e+000 0.0000000e+000 1.0000000e+000 1.0000000e+000                     </pre>				
Pose_img-0009-dewarp - Notepad				
<pre> -5.5837377e-002 1.9005013e-002 -9.9825898e-001 2.7668752e+001 9.0168712e-001 4.3032063e-001 -4.2243140e-002 -3.8706695e+001 4.2876861e-001 -9.4274602e-001 -4.1164551e-002 8.7217773e+002 0.0000000e+000 0.0000000e+000 0.0000000e+000 1.0000000e+000                     </pre>				
Pose_img-0010-dewarp - Notepad				
<pre> -2.7216241e-002 -4.6178053e-002 -9.9856240e-001 2.6634589e+001 8.5720891e-001 5.1281236e-001 -4.7078360e-002 -3.8219828e+001 5.1424913e-001 -8.3725789e-001 2.5627413e-002 8.7120821e+002 0.0000000e+000 0.0000000e+000 0.0000000e+000 1.0000000e+000                     </pre>				
Pose_img-0011-dewarp - Notepad				
<pre> -2.525597e-002 -4.6371277e-002 -9.9860496e-001 2.6589903e+001 7.9974746e-001 5.9841343e-001 -4.8014277e-002 -3.8014716e+001 5.9980510e-001 -7.9984441e-001 2.1972022e-002 8.6789477e+002 0.0000000e+000 0.0000000e+000 0.0000000e+000 1.0000000e+000                     </pre>				
Pose_img-0012-dewarp - Notepad				
<pre> -1.9724058e-002 -4.6030666e-002 -9.9874528e-001 2.6642621e+001 7.4723317e-001 6.6301523e-001 -4.5314360e-002 -3.7649263e+001 6.6426918e-001 -7.4718939e-001 2.1318290e-002 8.5903138e+002 0.0000000e+000 0.0000000e+000 0.0000000e+000 1.0000000e+000                     </pre>				

Figure 4.32 The pose of the FTRAC with respect to the C-arm in each view.

## Experimental Results

The results from error checking in 4.3.2 show that the average residual error of the FTRAC (size 20mm) is about 0.50 - 0.55 mm. This information is applied to subsection 4.2.3. In order to determine the pose of the distal hole axis. The relationship between FTRAC and IMN in 3D is compared to the result from image processing. The error of translation is about 0.5mm while in rotation is about  $0.33^\circ$ . These answers come from the relation of the FTRAC and IMN in 3D and the projection images.



## CHAPTER V

### DISCUSSIONS

This chapter discusses the approach to recover distal hole's axis in intramedullary nail chapter 3 and chapter 4. The approach divided into three parts which are 1) Recovery of distal holes axis using X-Y span of distal hole's projection images, 2) Recovery of distal holes axis using interested area of distal hole's projection images, and 3) Recovery of distal holes axis using additional fiducial, Fluoroscope tracking (FTRAC.) The experimental results are discussed in this chapter. Our approach is to further implement in Orthopaedic surgery at Faculty of Medicine Siriraj Hospital, Mahidol University, Thailand.

#### **5.1 Recovery of Distal holes axis using X-Y span of distal hole's projection images**

This approach simulates the IMN rotation and uses the X-Y span to represent the distal hole axis. This method is relying on the collected data from the simulation. The result from this method can be used as a preliminary assumption for the second approach, which is the limitation of IMN rotation in term of requiring the crossed section area of the distal hole to determine the distal hole axis. Three x-ray images are required to find the distal hole axis. The other requirement is that the first image will be counted after one see the cross-section area of the upper and lower distal holes from the simulation. The error of this method can be compared to the second method. The result shows that the limitation of rotating the IMN is around -28 to 28 degrees which is higher than the other two methods. Due to the simulating is depend on the IMN shape which one assumes it to be a perfectly cylindrical shape while in reality the IMN is not totally in a cylindrical shape.

However, the algorithm has not been implemented or tested in any physical experiments. The author suggests realizing the algorithm in an experiment set up for testing the accuracy and robustness in future works.

## **5.2 Recovery of distal holes axis using interested area of distal hole's projection images**

Second algorithm, simulation of IMN rotation has been developed and implemented with the image processing. Anyway the second algorithm is still based on collecting the data during the experiment. This algorithm builds upon the previous method by adding more information to make it more accurately. Both algorithms from the first and second methods make significant improvements over existing works and make new contributions. The approach is to break down the complex problem into small tractable steps. The advantage of these two methods is no requirement of the additional device and tools. These two methods do not need any additional tools or devices to attach to the patient. The main concern of the surgeon is the safety to the patient and the workspace area during the operation.

## **5.3 Recovery of distal holes axis using additional fiducial, Fluoroscope Tracking (FTRAC)**

This method adds a device called "FTRAC." This is a fiducial for fluoroscope tracking. In this part, the proposed approach does not depend on the pre-generated database. An important improvement of this approach is that it accounts for the variability within an image and across images by taking a statistical approach rather than predetermined one. Since the previous works mostly deal with simulated images, where it is hard to simulate with a real setup, not much attention is given to this real problem.

The fiducial segmentation algorithm developed is essentially a set of three algorithms, one each for BB, line and ellipse segmentation, feeding on one another in

consequential manner. To determine the pose of the distal hole, the image processing takes an important role to this step. BB segmentation was done using morphological techniques. Lines were segmented using Hough transform. But the accuracy of the results of Hough transform depends extensively on how the parameter space is quantized, which is an optimization problem in itself. The error by combining the mathematical model of points, lines, and ellipses effected directly to the pose of the distal hole axis. So, the concerning of this method is the residual error of the FTRAC.



## CHAPTER VI

### CONCLUSION AND FUTURE WORKS

This study proposes the methods to investigate a new algorithm to recover the 3-D pose (position and orientation) of distal holes in the intramedullary nail by using no more than four x-ray imaging projections and to implement the recovering of IMN distal hole's orientation using a new algorithm.

To obtain accurate results in each method, a bunch of experimentation was done. First method is relying on the simulation. In order to test the algorithm, simulations were done in stages. The simulation was started with pure rotation about X-axis, and followed by pure rotation about Y-axis, combination of X-Y rotations, and combination of X-Y-Z rotations, which are all possible cases of nail rotation.

Second method is developed from the first method. In order to test the algorithm, collecting a bunch of dataset were done in stages. Collecting data by taking the image of IMN rotation starting at 2 degrees and increasingly by 2 degrees until 20 degrees, totally 300 images were taken. To validate the data one needed to find the optimal equation and the tool curve was plotted as shown in chapter 4.

Third method is applying a device to our approach which is a fluoroscope tracking (FTRAC) fiducial. The reason of using FTRAC is the size of the FTRAC which is a small fiducial, and the FTRAC does not need to be attached to the patient one therefore does not need to concern about biocompatibility. To obtain accurate results, the x-ray images of the FTRAC and the IMN in many possible rotation of the C-arm were taken. There are 14 data set of the C-arm rotating about the FTRAC and IMN (FTRAC and IMN are fixed steadily). In each data set consists of 13 viewing images of the C-arm as shown in Figure 4.27. In each data set, FTRAC will be rotated to another 5 degrees by the rotary stages. So, one needs to rotate totally 14 times of the FTRAC and take the x-ray image of the IMN and FTRAC with the C-arm viewing

approximately 180 images. The limitation of this method is the complexity of the calibration process. To ignore this process [21] one needs to make the IMN and FTRAC appear in the middle of the image as much as one can. To reduce the error from the distortion at the edge of the images, that work was done by A. Jain *et al.*

The future work in this topic is to reduce the error of the algorithm which determine the optimal tool curve for the second method and solve the problem of the calibration procedure. Although this problem was dealt by A. Jain *et al.*, but there is the errors from the distortion at the edge of the images. To avoid this problem, surgeon needs to set the C-arm viewing axis directly to the FTARC and IMN to make the position of the FTRAC and IMN at the middle of the image, which is difficult for the surgeon during the operation and in the limit of working area.

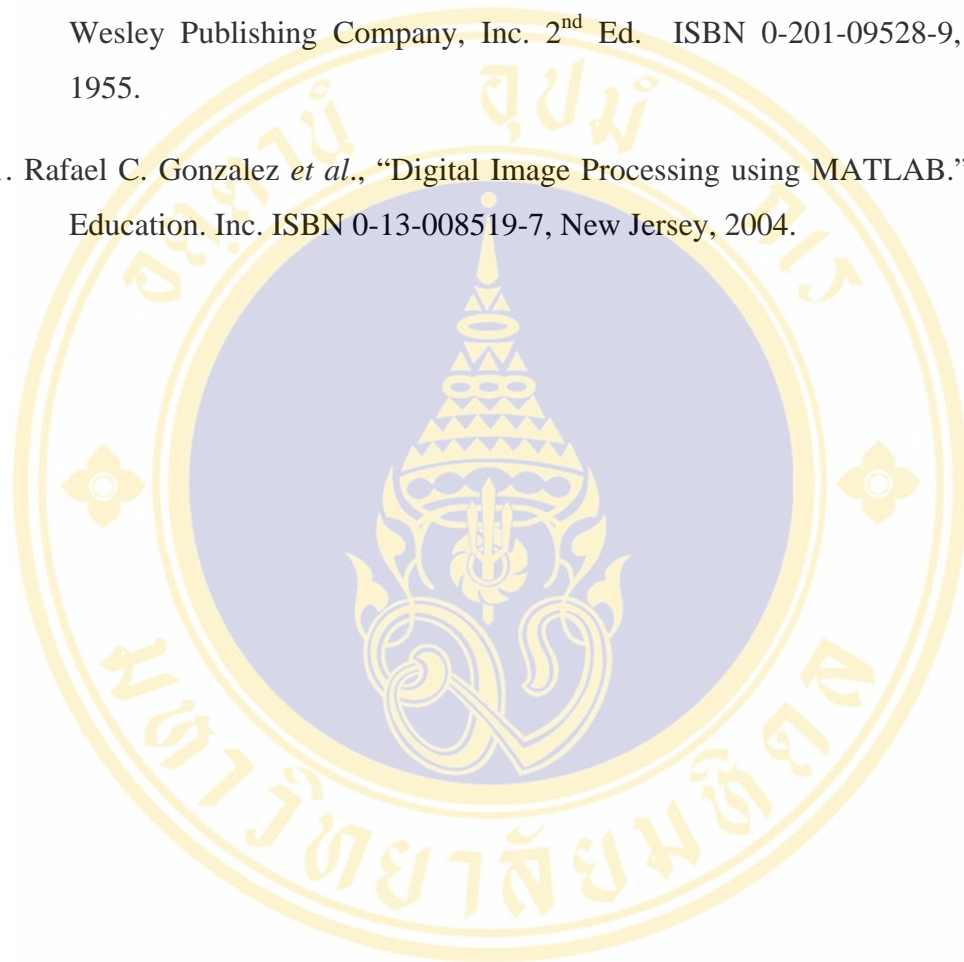
## REFERENCES

1. Banchong Mahaisavariya, M.D. Minimal Invasive Orthopaedic Surgery. *Siriraj Med Journal*, Vol. 58: p. 1227-1228, 2006.
2. Mahaisavariya B. *et.al.*, “การยึดตรึงกระดูกหักด้วยแกนตามกระดูก” Ruenkaew Published, First Edition, 1999.
3. Leo Joskowicz, Ph.D. Fluoroscopy-Based Navigation in Computer-Aided Orthopaedic Surgery. *IFAC 2000*.
4. Leo Joskowicz and Russell H.Taylor. “Computers in Imaging and Guided Surgery.” *Computing science and engineering*. September/October 2001 (Vol. 3, No. 5) pp. 65-72
5. Russell H.Taylor. *et al.*, “An Image-Directed Robotic System for Precise Orthopaedic Surgery.” *IEEE Transactions on robotics and automation*. Vol. 10, No.3, June 1994.
6. S. David Stulber, Thomas C.Kienzle III. Computer-and Robot-Assisted Orthopaedic Surgery. *Computer-Integrated Surgery*, Chp.27, p.373-378.
7. Stephane Lavallee, Richard Szeliski, Lionel Brunie. Anatomy-Based Registration of Three-Dimensional Medical Images, Range Images, X-Ray Projections, and Three-Dimensional Models Using Octree-Splines. *Computer-Integrated Surgery*, Chp.7, p.115-143.
8. L.Tockus, L.Joskowicz, A,Simkin, and C.Milgrom. “Computer-Aided Image-Guided Bone Fracture Surgery: modeling, Visualization, and Preoperative Planning.” *MICCAI’98, LNCS 1496*, pp. 29-38, springer 1998.
9. Sanford L. Meeks., *et al.* “Image localization for frameless stereotactic radiotherapy.” *Int J.Radiation Oncology Biol.Phys.*, Vol.46, No.5, pp. 1291-1299, 2000.
10. David M.Kahler, MD. “ Image Guidance: Fluoroscopic Navigation.” *Clinical Orthopedics and related research*, Number 421, pp.70-76

11. Eric J.Hazan, Leo Joskowicz. "Computer-Assisted Image-Guided Intramedullary Nailing of Femoral Shaft Fractures." *Techniques in Orthopedic*, Vol. 18, No.2, 2003.
12. Niels Schep. "Validation of computer assisted anteversion and length control in closed nailing of femoral shaft fracture."
13. Oliver Tonet, Giuseppe Megali, Paolo Dario, Maria Chiara Carrozza, Maurilio Marcacci, Pier Francesco La Palombara. A Novel Navigation System for Computer Assisted Orthopedic Surgery. *Proceeding of the 22<sup>nd</sup> Annual EMBS International Conference*, July 23-28, 2000 Chicago IL.
14. Y.Zhu, R.Phillips, J.G. Griffiths, W. Viant, A.Mohsen, M. Bielby. Recovery of Distal Hole Axis in Intramedullary Nail Trajectory Planning. *Proceeding of the 2001 IEEE*.
15. Ziv Yaniv, Leo Joskowicz. Robot-Assisted Distal Locking of Long Bone Intramedullary Nails: Localization, Registration, and In Vitro Experiments. In *Proc. Medical Image Computing and Computer-Assisted Intervention–MICCAI*, Part II: 58-65, 2004
16. T. Wang, W. Liu and L. Hu. BPOR: A Fluoroscopy-Based Robot Navigating System for Distal Locking of Intramedullary Nails. *Proc of 2004 IEEE/RSJ International Conference on Intelligent Robots and Systems*, Page(s): 3321-3326, 2004.
17. G. Zheng, X. Zhang, D. Haschtmann, P. Gedet and L.-P. Nolte. Accurate and robust recovery of distal locking holes in computer-assisted intramedullary nailing of femoral shaft fractures. *Proc of CAOS 2006, Montreal, Canada*, p. 599-602, 2006.
18. G. Zheng, X. Zhang and L.-P. Nolte. Automatic pose recovery of the distal locking holes from single calibrated fluoroscopic image for computer-assisted intramedullary nailing of femoral shaft fractures. *MIAR 2006, Third International Workshop on Medical Imaging and Augmented Reality*, vol. LNCS 4091, p. 195-202, 2006.
19. Th. Leloup, W. El Kazzi, O. Debeir, F. Schuind and N. Warzee. Automatic fluoroscopic Image Calibration for Traumatology Intervention Guidance.

- Computer as a Tool, 2005. EUROCON 2005. The International Conference on*, page(s): 374- 377, 2005
20. H. Livyatan, Z. Yaniv and L. Joskowicz. Robust Automatic C-arm Calibration for Fluoroscopy-based Navigation: a Practical Approach. *Proc. 5th Int. Conf. on Medical Image Computing and Computer-Aided Intervention, MICCAI 2002*, October 2002, Tokyo, Japan. Lecture Notes in Computer Science 2488. Dohi, T. and Kikinis, R. editors, Berlin: Springer, 2002. Vol. 2. pp. 60-68.
  21. A. Jain, T. Mustafa, Y. Zhou, C. Burdette, G. S. Chirikjian and G. Fichtinger. FTRAC—A robust fluoroscope tracking fiducial. *Medical Physics*, Volume 32, Issue 10, pp. 3185-3198, October 2005.
  22. A. Jain, R. Kon, Y. Zhou and G. Fichtinger. C-arm Calibration- Is it Really Necessary?. *Eighth International Conference on Medical Image Computing and Computer-Assisted Intervention -- MICCAI 2005, Proceedings in Lecture Notes in Computer Science* Vol. 3749, pp 639-646, Springer, 2005.
  23. J. Christopher Eyke, J. E. Ricciardi, W. Roesch and T. S. Whitecloud III. Computer-Assisted Virtual Fluoroscopy. *The University of Pennsylvania Orthopaedic Journal*, Vol. 15: 53–59, 2002.
  24. R. Hofstetter, M. Slomczykowski, M. Sati and L.-P. Nolte. Fluoroscopy as an Imaging Means for Computer-Assisted Surgical Navigation. *Journal of image guided surgery, Computer Aided Surgery*, 4: 65-76, 1999.
  25. J Serra, *Image analysis and mathematical morphology*, London, England: Academic Press 1982.
  26. P. Soille, *Morphological Image Analysis: Principles and applications*. Berlin, Germany, Springer 1999.
  27. C. Neatpisarnvanit, and J. Suthakorn, “Intramedullary Nail Distal Hole Axis Estimation Using Blob Analysis and Hough Transform,” in *Proc. of The 2006 International Conference on Robotics, Automation and Mechatronics (RAM2006)*, Bangkok, Thailand, 7-9 June, 2006.
  28. A. Jain, I. Iordachita, G. Fichtinger. “A small size fluoroscope tracking (FTRAC) fiducial,” *CAOS 2005*, p.235-238.

29. Milan Sonka, Vaclav Hlavac, and Roger Boyle, “Image processing, analysis, and machine vision”, 2<sup>nd</sup> Ed. ISBN 053495393X, Pacific Grove, CA : PWS Pub., c1999.
30. John J. Craig. “Introduction to Robotics Mechanics and Control.” Addison-Wesley Publishing Company, Inc. 2<sup>nd</sup> Ed. ISBN 0-201-09528-9, Canada, 1955.
31. Rafael C. Gonzalez *et al.*, “Digital Image Processing using MATLAB.” Pearson Education. Inc. ISBN 0-13-008519-7, New Jersey, 2004.





# AN EFFICIENT ALGORITHM FOR RECOVERING DISTAL HOLES' AXES IN INTRAMEDULLARY NAIL

Paweena U-Thainual<sup>1</sup>, Jackrit Suthakorn<sup>2</sup>

<sup>1,2</sup>Applied Research Labs of Biomedical and Robotics Technology,

<sup>1</sup>Biomedical Engineering Program

<sup>2</sup>Department of Mechanical Engineering,

Mahidol University,

Nakorn Pathom 73170, THAILAND

[egist@mahidol.ac.th](mailto:egist@mahidol.ac.th)

## ABSTRACT

Computer-Integrated Surgery (CIS) is currently gaining its popularity among biomedical engineering researchers. Medical navigation and Robot-Assisted Surgery are major subdivisions of the CIS. Even though 3D imaging machines, such as MRI or CT are widely used for these days but they are useful only for pre-operation stage. In the intra-operation stage, most surgeons have performed operations depending on standard 2D X-ray images. Therefore, highly skilled surgeons are required in most complicated operation. Important reasons to develop surgical robots are to augment surgeons in long-period or highly radiating exposed operation. However, the robot is required trajectory paths to be followed which, in this case, they are generated by a medical navigation system.

Our study is to develop a navigation system for aiding surgeon and guiding a surgical robot for orthopedic applications. An orthopedic operation, called "Closed Intramedullary Nailing of Femur (Closed Nailing)," is one of the frequent cases of orthopedic surgery. This surgery also requires accurate positioning and orientating of the implant, and an important effort is to find the pose of two distal holes on the intramedullary nail after being inserted into intramedullary canal. During the conventional closed nailing surgery, surgeons require high experience, and a number of trial-and-error adjustments to correct the path for inserting the screws through those distal holes. The process can be done by gradually adjusting the shooting angle until the projection of the two distal holes is seen as circular as possible on the X-ray image. Therefore, both surgeon and patient are continuously exposed by a great amount of X-ray exposure from the fluoroscopic imaging system.

This paper describes a new algorithm to recover the pose (position and orientation) of distal holes in the intramedullary nail by using only two X-ray imaging projections, such as, AP (anterior/posterior) and lateral views. The algorithm is based on inverse kinematics approach. The paper includes mathematical modeling, algorithm formulations, simulation and experimental results and conclusion of the algorithm performance.

**Keywords**— Navigation, Medical Navigation, Computer-Integrated Surgery, Closed Intramedullary

Nailing, Inverse Kinematics, Orthopedic Surgical Technique.

## 1. INTRODUCTION

Numerous orthopedic operations require locating of implants and internal organs such as bone. Currently, this procedure requires x-ray exposure during the surgery to allow the surgeon to indicate the position and orientation of the patient's internal organs and medical inserting devices. An orthopedic operation, called "Closed Intramedullary Nailing of Femur (Closed Nailing)," is one of the frequent cases among orthopedic surgeries. This surgery also requires accurate positioning and orientating of the implant. One of the most difficult tasks for surgeons is to identify the position and orientation of the screwing holes (typically in circular shape) at both ends of the intramedullary nail (IMN) after being inserted into a patient's femoral canal. The distal hole locations may be shifted by external forces and torques applied to the IMN during the insertion procedure resulting in the IMN to deform.

In the conventional closed nailing surgery, surgeons require high experience, and a number of trial-and-error adjustments to correct the path for inserting the screws through those distal holes. Figure 1 and 2 illustrate the Closed Nailing of Femur and how healthcare personals would be exposed by X-Ray during the operation. The process can be done by gradually adjusting the shooting angle until the projection of the two distal holes is seen as circular as possible on the x-ray image. Therefore, both surgeon and patient are continuously exposed by a great amount of x-ray exposure from the fluoroscopic imaging system. This could harm the surgeon and patient for their long term health. This study investigates a new algorithm to recover the 3-D pose (position and orientation) of distal holes in the intramedullary nail by using only three x-ray imaging projections, such as, AP (anterior/posterior) and lateral views. The algorithm is based on inverse kinematics approach. A mathematical model and an algorithm are developed and described using group theory. The study includes mathematical modeling, algorithm formulations, simulation and experimental results and conclusion of the algorithm performance.

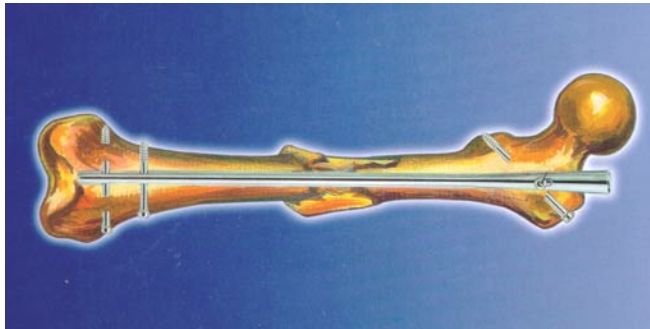


Figure 1: Intramedullary Closed Nailing of Femur.



Figure 2: Image shows a number of healthcare personals who are exposed by X-Ray during a Close Nailing Surgery.

## 2. PREVIOUS WORKS

Minimally invasive surgery (MIS) is currently popular because of its advantages especially the patient recovery period which can be reduced tremendously. Computer-integrated surgery (CIS) gains more interest from biomedical researchers [1-4], because it can reduce complexity in MIS procedures. Closed nailing surgery is also a frequent orthopedic MIS case. This surgery requires accurate positioning and orientating of medical inserting devices (e.g. nail) with respect to the internal organs (e.g. femoral fractures). During the conventional closed nailing surgery, both surgeon and patient are continuous exposed by a great amount of X-ray exposure from the fluoroscopic imaging system. Long term X-ray exposure could harm both the surgeon and patient.

Thus, a new approach was previously proposed [5] to aid surgeons in recovering the position and orientation of an intramedullary nail after being inserted into a patient's femoral canal. This approach utilizes both fluoroscopic and optical stereoscopic systems with a computer-integrated method. The method includes using a 3-D tracking system with markers, and mapping coordinate frames and axes received from fluoroscopic images into real-time optical images on a computing system. A mathematical model and an algorithm are developed to generate a guiding path for the surgery guidance system. Neatpisarnvanit and Suthakorn preliminarily implemented

the 1-D path-generating algorithm using Blob analysis and Hough transform [6]. Zhu et al. presented a similar approach to derive the 3-D position and orientation of the distal hole axis using two radiation images [7].

## 3. OVERALL OF NAVIGATION RESEARCH AT MAHIDOL UNIVERSITY

Research in development of surgical navigation system for orthopedic surgery at Mahidol University can be described in stages as follow:

### 3.1. Medical Information Retrieval Stage

The first stage is to collect medical information and physician's requirements. This also includes a series of surgery observations. The stage results create a set of constraints and directions in conducting the following research.

### 3.2. Methods and Algorithm Development Stage

This stage consists of fluoroscopic image processing, mathematical modeling and information processing, surgical planning, image mapping and monitoring. Fluoroscopic image processing is to extract distal hole figures from an X-ray image. The mathematical modeling and information processing are to retrieve distal hole position and orientation using information from X-ray images. Surgical planning is to generate a guiding path for physician to follow. Image mapping is to map generated guiding path and other information from X-ray images onto optical images from an optical stereoscopic system. Monitoring is to display and interface between navigation system and surgeon. Each subsystem is to develop separately and to be integrated in the next stage.

### 3.3. Instrumentation and Development Stage

This stage is to utilize all knowledge and subsystems from previous stages to develop a prototype set of navigation system. This is to prepare for physical and clinical trials in the next stages.

### 3.4. Stage of Physical Experiment in Lab Set Up

This experiment stage is to test and improve the system which performs in a lab with environmental set up. The end of this stage is to systemic test in artificial bones or cadavers.

### 3.5. Clinical Trial Stage

This stage will not be started until physicians and ethic board would give us a permission to perform the clinical trials. This stage is purpose to demonstrate and micro-adjust a prototyped surgical navigation system. A full

surgical navigation system is depicted and shown in Figure 3.

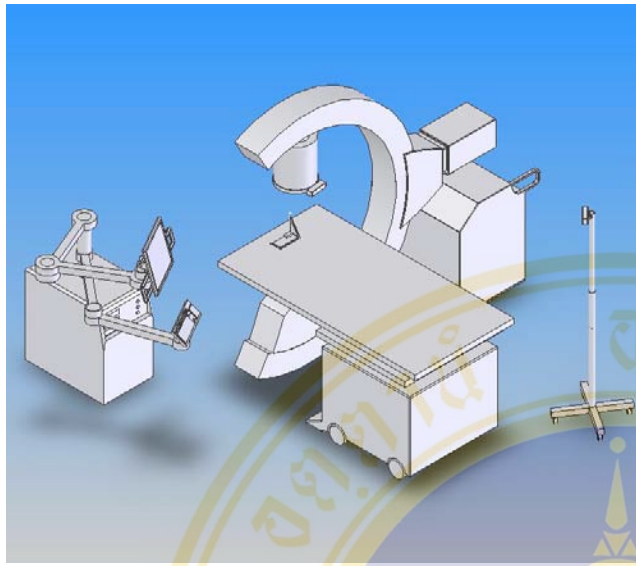


Figure 3: Image depicts a full surgical navigation system in navigation research at Mahidol University.

#### 4. PROBLEM STATEMENT

In a closed nailing surgery, one of the most difficult tasks for surgeons is to identify the position and orientation of the screwing holes (typically in circular shape) at both ends of the intramedullary nail after being inserted into a patient's femoral canal. The hole location may be shifted by external forces and torques applied to the IMN during the insertion procedure resulting in the IMN to deform. To recover the position and orientation (or "pose") of the screwing holes in the conventional operation, surgeons require high degree of experience, and a number of trial-and-error adjustments to correct the path for inserting the screws. This can be done by gradually adjusting the shooting angle until the projection of the two screwing holes is seen as circular as possible on the X-ray image. The concept of the proposed approach is to utilize a hybrid system of a fluoroscopic system and an optical stereoscopic system to quickly recover the screwing holes on the IMN, and to reduce the number of trial-and-error adjustments.

The operation starts after the surgeon inserts an IMN into the femur canal and sets the fractured bone into a desired position [5]. Two markers are attached to the patient in the location that can be seen from both fluoroscopic and optical stereoscopic imaging systems. The attaching procedure is done by attaching each marker directly to the distal and proximal part of the fractured bone through the skin (one marker for each position.)

Then, two X-ray images are taken by the fluoroscopic (C-Arm) system from different angles. The image processing and pattern recognition methods are used to generate (1) the frames attached to the markers, (2) the axis of the IMN and its perimeter, and (3) the screwing holes' location and orientation (pose) on the IMN. Note that in most cases, the shape of screwing holes viewed on

X-ray images are in elliptical shape as shown in Figure 4, and a set of diagram comparing between images from optical stereoscopic and fluoroscopic is shown in Figure 5.

Due to the complexity of current research problems, this paper focuses on how to determine the axis of the IMN and IMN rotations about Axes X and Y. Also, to further simplify the problem, it is assumed that the IMN translational movement is allowed in the X and Y directions (as shown in Figure 6), whereas the IMN rotational movement is allowed in the X and Y axes.

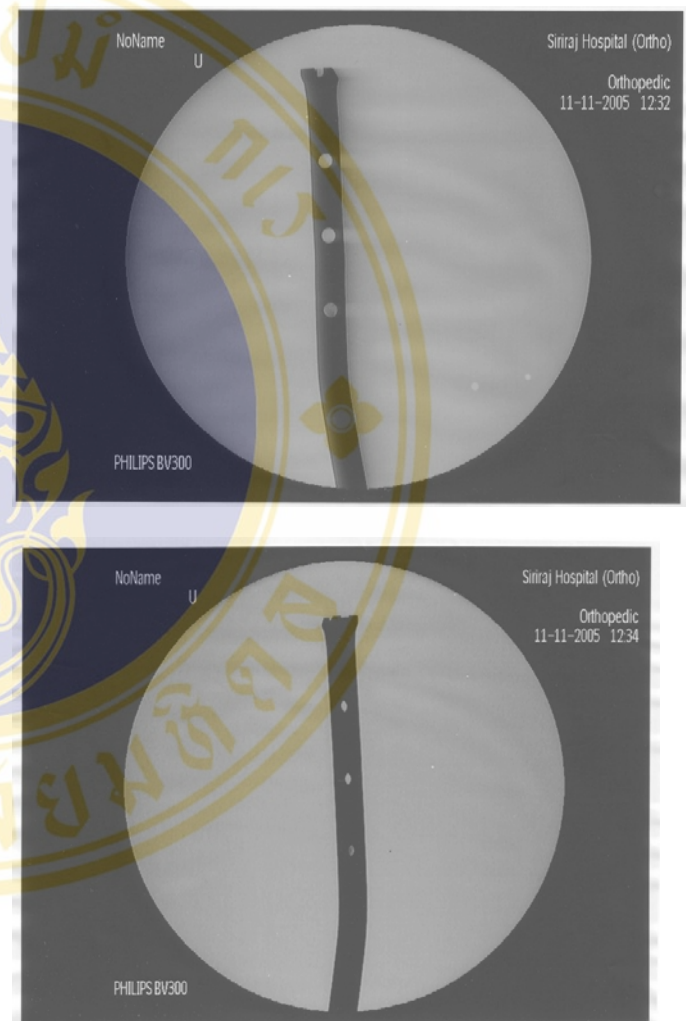


Figure 4: IMN distal holes are shown at different angles of view. Top image shows the distal holes while their axes are perpendicular to the Fluoroscopic image plane, and Bottom image shows the distal holes at a rotated angle.

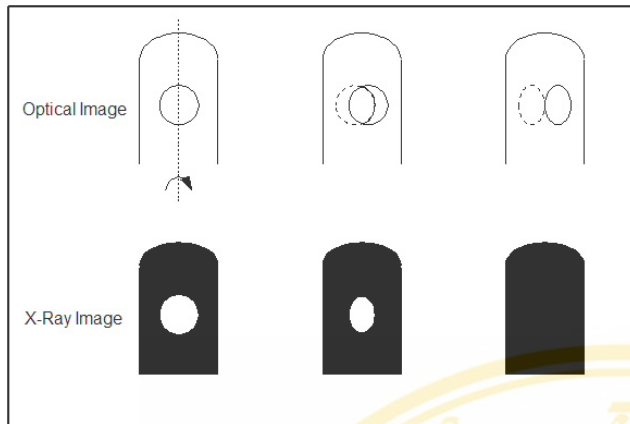


Figure 5: IMN diagram comparing images as seen from the optical stereoscopic (upper) and fluoroscopic (lower) systems.

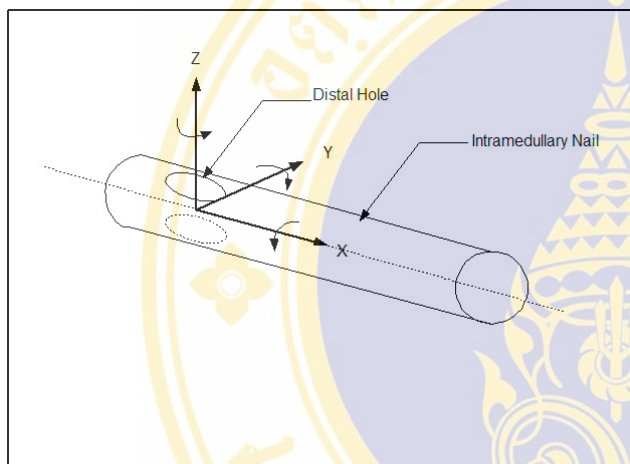


Figure 6: Distal Hole Axes.

### 5. METHOD

The approach is starting with generating database of nail's projection images. These images are generated to simulate all possible X-ray images of nail during the operation. All images are to be extracted four set of informative parameters which are 1) the length of line between intersection points of upper and lower distal holes (denoted as "a"), 2) the slope of the same line (denoted as "theta", 3) the maximum width of crossed distal holes (denoted as "b"), and slope of nail edges' slopes.

Next is to store rotation angles (X-, Y- and Z-Axes) and four parameter sets into the database system. The distal hole's axis recovering algorithm is working by matching the result from X-ray image to the stored database information. The overall approach can be illustrated in diagram as Figure 7. (See image 8 for all notations.)

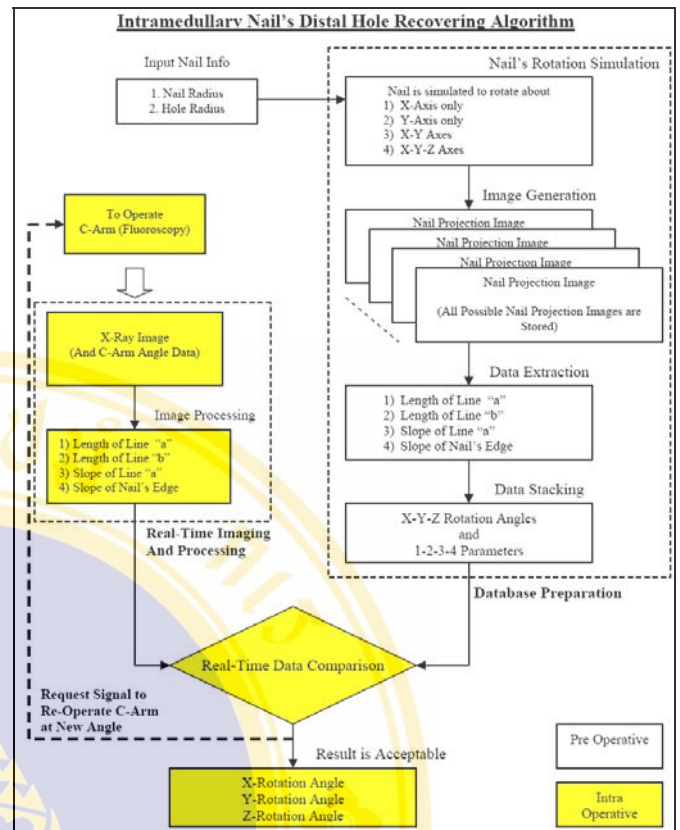


Figure 7: Diagram of the Propose Algorithm to Recover Intramedullary Nail's Distal Hole Axis.

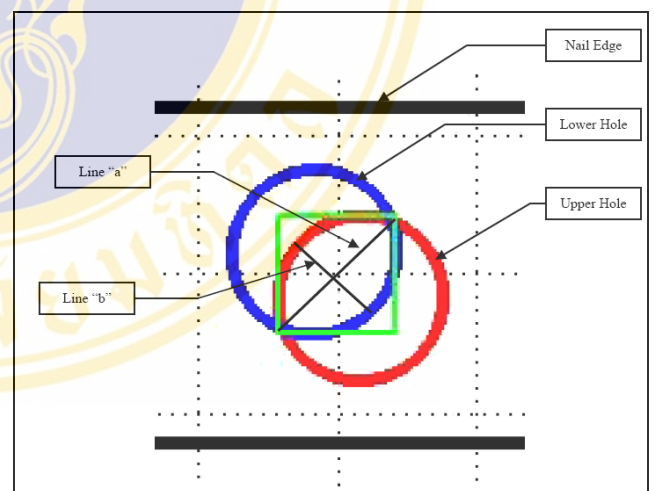


Figure 8: Generated Projection View of Rotated Nail with All Notations

### 6. SIMULATIONS AND RESULTS

In order to test the algorithm, simulations were done in stages. The simulation started with pure rotation about X-axis, pure rotation about Y-axis, combination of X-Y rotations, and combination of X-Y-Z rotations.

#### 6.1. Rotation about X-Axis

In this subsection, a set of simulation results for pure rotation about X-axis is illustrated in Figure 9(a). Figure 9(a) shows four cases of pure Y-rotation angle:

- 1)  $X = 19^\circ$  2)  $X = -6^\circ$  3)  $X = -19^\circ$  and 4)  $X = 10^\circ$ .

**6.2. Rotation about Y-Axis**

In this subsection, a set of simulation results for pure rotation about Y-axis is illustrated in Figure 10. Figure 10 shows four cases of pure Y-rotation angle:

- 1)  $Y = -24^\circ$  2)  $Y = -21^\circ$  3)  $Y = -8^\circ$  and 4)  $Y = 13^\circ$ .

**6.3. Rotations about X- and Y-Axes**

In this subsection, a set of simulation results for rotations about X- and Y-axes is illustrated in Figure 11. Figure 11 shows four cases of X-Y Euler rotation angles:

- 1)  $X = 0^\circ$   $Y = 0^\circ$   $Z = 0^\circ$  2)  $X = -15^\circ$   $Y = -15^\circ$   $Z = 0^\circ$   
 3)  $X = -8^\circ$   $Y = -8^\circ$   $Z = 0^\circ$  and 4)  $X = 8^\circ$   $Y = 8^\circ$   $Z = 0^\circ$ .

**6.4. Rotations about X-, Y- and Z-Axes**

In this subsection, a set of simulation results for rotations about X-, Y-, and Z-axes is illustrated in Figure 12. Figure 12 shows four cases of X-Y-Z Euler rotation angles:

- 1)  $X = 6^\circ$   $Y = -16^\circ$   $Z = -30^\circ$  2)  $X = 21^\circ$   $Y = -2^\circ$   $Z = -30^\circ$   
 3)  $X = 11^\circ$   $Y = 3^\circ$   $Z = -30^\circ$  and 4)  $X = 12^\circ$   $Y = -5^\circ$   $Z = -30^\circ$ .

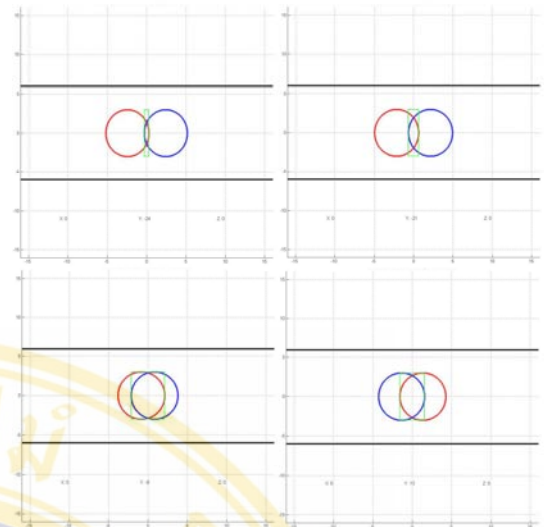


Figure 10: Simulation Results for Rotation about Y.

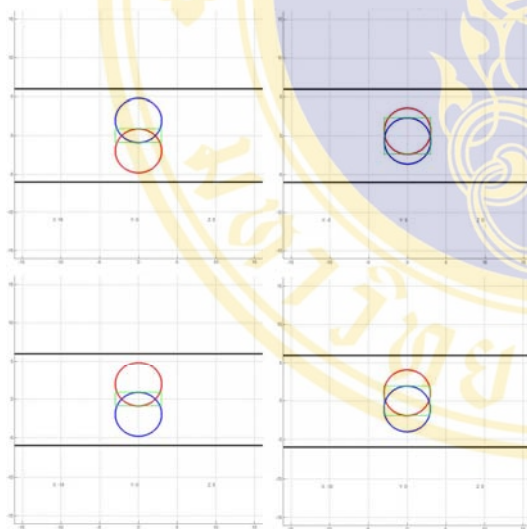


Figure 9: Simulation Results for Rotation about X.

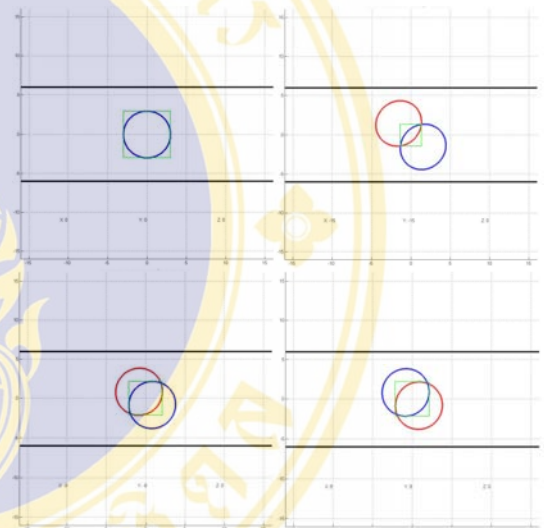


Figure 11: Simulation Results for Rotation about X-Y.

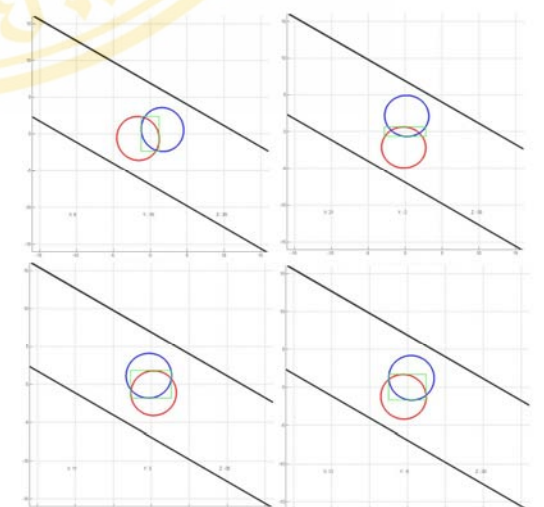


Figure 12: Simulation Results for Rotation about X-Y-Z.

## 7. DISCUSSION

This paper discussed a preliminary approach to recover distal hole's axis in intramedullary nail. The approach was using inverse kinematics algorithm. The algorithm was implemented in stages; 1) X-rotation only, 2) Y-rotation only, 3) X/Y-rotation, and 4) X/Y/Z-rotation. The results were satisfied.

However, the algorithm has not been implemented or tested in any physical experiments. The author has a plan to realize the algorithm in an experiment set up for testing the accuracy and robustness.

## 8. ACKNOWLEDGMENT

This project is partially supported by the National Electronics and Computer Technology Center of Thailand. The author wish to thank Prof. Dr. Banchong Mahaisavariya of Siriraj hospital school of medicine, Mahidol University, for his invaluable helps. The author also would like to thank all researchers in Biomedical and Robotics Lab (BART Lab), Mahidol University for assistances and suggestions.

## 9. REFERENCES

- [1] D. Stoianovici, L. L. Whitcomb, J. H. Anderson, R. H. Taylor, and L. R. Kovassi, "A Modular Surgical Robotic System for Image Guided Percutaneous Procedures," in *Proc. of the Int'l Conf. on Medical Image*, Trento, Italy, 1990.
- [2] R. H. Taylor, P. Jensen, L. L. Whitcomb, A. Barnes, R. Kumar, D. Stoianovici, P. Gupta, Z. Wang, E. de Juan, and L. R. Kavoussi, "A Steady-Hand Robotic System for Microsurgical Augmentation," *Journal of Robotics Research*, 1999.
- [3] H. Kang, and J. T. Wen, "Robotic Assistants Aid Surgeons during Minimally Invasive Procedures," *IEEE Engineering in Medicine and Biology*, Jan – Feb 2001.
- [4] G. Fichtinger, "Surgical Navigation, Registration, and Tracking," Available: <http://cisstweb.cs.jhu.edu/people/gab/or/Cs-600.145/Lectures/RegTrack.pdf>
- [5] J. Suthakorn, I. Chuckpaiwong, and B. Mahaisavariya, "A Novel Surgical Guidance System Utilizing Hybrid Fluoro-Stereoscope Navigation For An Orthopedic Surgery," in *Proc. of The 8th International Research/Expert Conference (TMT2004)*, Neum, Bosnia and Herzegovina, 15-19 September, 2004.
- [6] C. Neatpisarnvanit, and J. Suthakorn, "Intramedullary Nail Distal Hole Axis Estimation Using Blob Analysis and Hough Transform," in *Proc. of The 2006 International Conference on Robotics, Automation and Mechatronics (RAM2006)*, Bangkok, Thailand, 7-9 June, 2006.
- [7] Y. Zhu, R. Phillips, J. G. Griffiths, W. Viant, A. Mohsen, and M. Bielby, "Recovery of Distal Hole Axis IntraMedullary Nail Trajectory Planning," in *Proc. of the 2001 Int'l Conf. on Robotics and Automation*, Seoul Korea, 2001, pp. 1561-1566.

# An Implementation on Recovery of Intramedullary Nail Distal Hole's Orientation

Paweena U-Thainual, Saowapak Sotthivirat, and Jackrit Suthakorn

**Abstract**— Closed Intramedullary Nailing of Femur (Femur Closed Nailing) is one of frequent orthopedic operations. Closed nailing surgery requires accurate positioning and orientating of a medical inserting device, the intramedullary nail (IMN). The IMN is forcedly inserted into the femoral intramedullary canal during the surgery. This is to fix bone fractures to be in place. Deforming of the IMN is occurred during the inserting process. This causes twisting of the IMN and shifting of the screwing hole especially at the distal part of the IMN. One of the most difficult tasks in this operation is to identify the distal hole's orientation. This process is called distal locking. In the conventional closed nailing surgery, surgeons require high experience, and a number of trial-and-error adjustments to correct the path for inserting the screws through those distal holes. Figure 1 and 2 illustrate the Closed Nailing of Femur and how healthcare personals would be exposed by X-Ray during the operation. The process can be done by gradually adjusting the shooting angle until the projection of the two distal holes is seen as circular as possible on the x-ray image. Therefore, both surgeon and patient are continuously exposed by a great amount of x-ray exposure from the fluoroscopic imaging system. This could harm the surgeon and patient for their long term health. This paper discusses an implementation on recovering of IMN distal hole's orientation using a new algorithm which is using area of distal hole's projected images. Only two to three x-ray images are required during the hole's orientation recovery. In order to demonstrate the algorithm, a set of implementations is done by using MATLAB in an experimental set up to simulate acquiring x-ray images.

## I. INTRODUCTION

**I**N this section, motivation, project overview and previous works are discussed.

### A. Motivation and Project Overview

Minimally Invasive Surgery (MIS) requires identifying positions and orientations of inserting medical devices and internal organs. An MIS, called Closed Intramedullary Nailing of Femur (or Closed nailing), is one of frequent orthopedic surgeries. Closed nailing surgery requires

accurate positioning and orientating of a medical inserting device, the intramedullary nail (IMN). The IMN is forcedly inserted into the femoral intramedullary canal during the surgery. This is to fix bone fractures to be in place. Deforming of the IMN is occurred during the inserting process. This causes twisting of the IMN and shifting of the screwing hole especially at the distal part of the IMN. One of the most difficult task in this operation is to identify the distal hole's orientation. This process is called distal locking. In the conventional closed nailing surgery, surgeons require high experience, and a number of trial-and-error adjustments to correct the path for inserting the screws through those distal holes. The process can be done by gradually adjusting the shooting angle until the projection of the two distal holes is seen as circular as possible on the x-ray image. Therefore, both surgeon and patient are continuously exposed by a great amount of x-ray exposure from the fluoroscopic imaging system. This could harm the surgeon and patient for their long term health. Our approach is to recover the IMN distal hole's orientation by using only two to three x-ray images. The acquired x-ray images are processed to recover and generate the screw's inserting path. Then, the path is mapped to optical images using marker as a reference frame.

### B. Previous Related Works

Minimally invasive surgery (MIS) is currently popular because of its advantages especially the patient recovery period which can be reduced tremendously. Computer-integrated surgery (CIS) gains more interest from biomedical researchers [1-4], because it can reduce complexity in MIS procedures. Closed nailing surgery is also a frequent orthopedic MIS case. This surgery requires accurate positioning and orientating of medical inserting devices (e.g. nail) with respect to the internal organs (e.g. femoral fractures). During the conventional closed nailing surgery, both surgeon and patient are continuous exposed by a great amount of X-ray exposure from the fluoroscopic imaging system. Long term X-ray exposure could harm both the surgeon and patient.

Thus, a new approach was previously proposed by the third author [5] to aid surgeons in recovering the position and orientation of an intramedullary nail after being inserted into a patient's femoral canal. This approach utilizes both fluoroscopic and optical stereoscopic systems with a computer-integrated method. The method includes using a 3-D tracking system with markers, and mapping coordinate frames and axes received from fluoroscopic images into real-time optical images on a computing system. A mathematical model and an algorithm are developed to

Paweena U-Thainual is with Department of Biomedical Engineering, Mahidol University, Thailand.

Saowapak Sotthivirat is with the National Electronics and Computer Technology Center, Thailand.

Jackrit Suthakorn (Corresponding Author) is with the Applied Research Network Center of Biomedical and Robotics Technology, and Dept of Mechanical Engineering, Mahidol University, Thailand.

This project is supported by National Metal and Materials Technology Center, Thailand. Project No. MT-B-49-BMD-14-125-G.

Paweena U-Thainual

generate a guiding path for the surgery guidance system. Neatpisarnvanit and Suthakorn preliminarily implemented the 1-D path-generating algorithm using Blob analysis and Hough transforms [6]. Zhu *et al.* presented a similar approach to derive the 3-D position and orientation of the distal hole axis using two radiation images [7].

Prior to the presented in this paper, The first and the last authors proposed an inverse kinematics based algorithm to predict nail rotation of 1-D case using only the vertical and horizontal lengths of distal hole's projected images [8]. Figure 1 illustrates diagrams show key information used to recover the nail's orientation. However, this algorithm has limitations during the real implementations.

II. METHODS

Prior to describe the full details of our new algorithm, example of x-ray images of IMN from different angles are shown in Figure 2. A diagram to compare optical images and projected images (x-ray) is also shown in Figure 3.

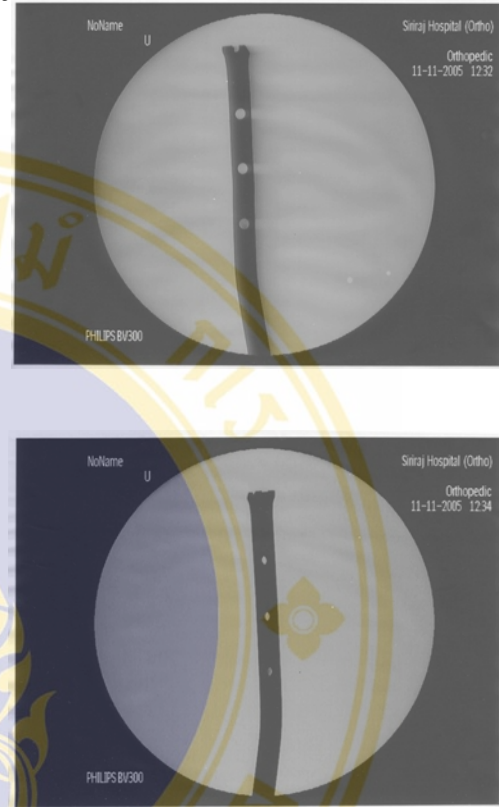
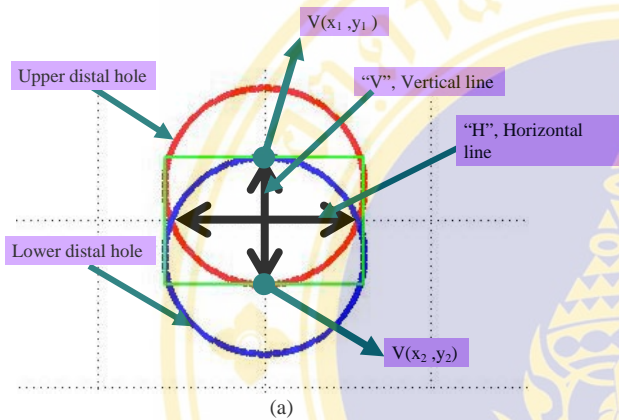


Fig 2. IMN distal holes are shown at different angles of view.

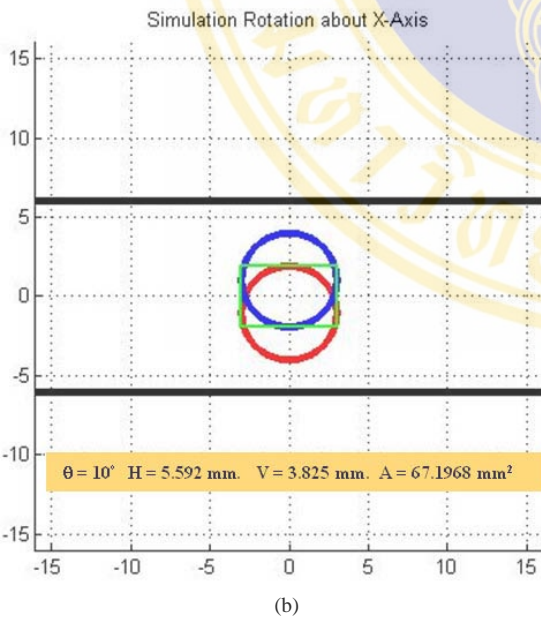


Fig 1.(a) All parameters are detected from algorithm and (b) the collected data of the simulation [8].

This paper discusses an implementation on recovering of IMN distal hole's orientation using a new algorithm which is using area of distal hole's projected images instead of vertical and horizontal lengths. In order to demonstrate the algorithm, a set of implementations is done by using MATLAB in an experimental set up to simulate acquiring x-ray images.

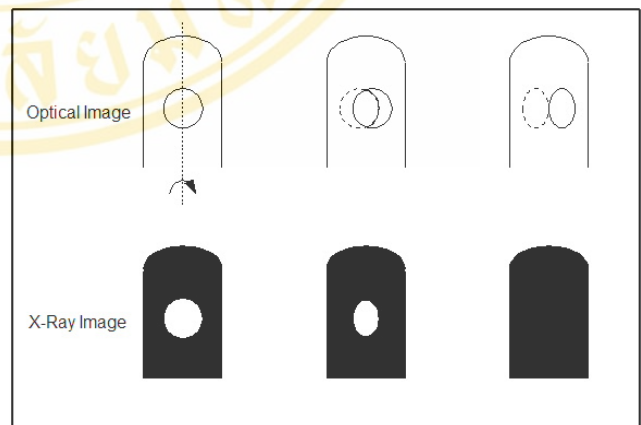


Fig 3. IMN diagram comparing images as seen from the optical stereoscopic (upper) and fluoroscopic (lower) systems.

The key of our new approach is to use only the area of distal hole's projected images (such as, x-ray images) to recover the nail's rotational angle. A diagram describes overview of algorithm as shown in the Figure 4. Part I, the approach is starting with collecting data process which is done during the pre-operation. The images of distal hole are taken at different rotating angles to collect the images data.

These images are processed by extracting only interesting parts (an example as shown in Figure 5.) The extracted images are processed to determine the area of distal's holes. All processed data is plot on an area to angle graph. A fitting curve technique is then applied to find the best fit to the data. The curve is called the "Tool Curve," and is used to be the key to reversely determine rotating angle in the Part II.

*Part I: Collecting Data*

Part I can be divided into two main steps, image preparation and distal hole detecting processes. Image preparation is starting with RGB distal hole imaging. A stereo camera is used to collect distal hole's images at different rotating angles which are 0, 5, 10, 15 and 20 degrees clockwise and counter clockwise. All RGB images

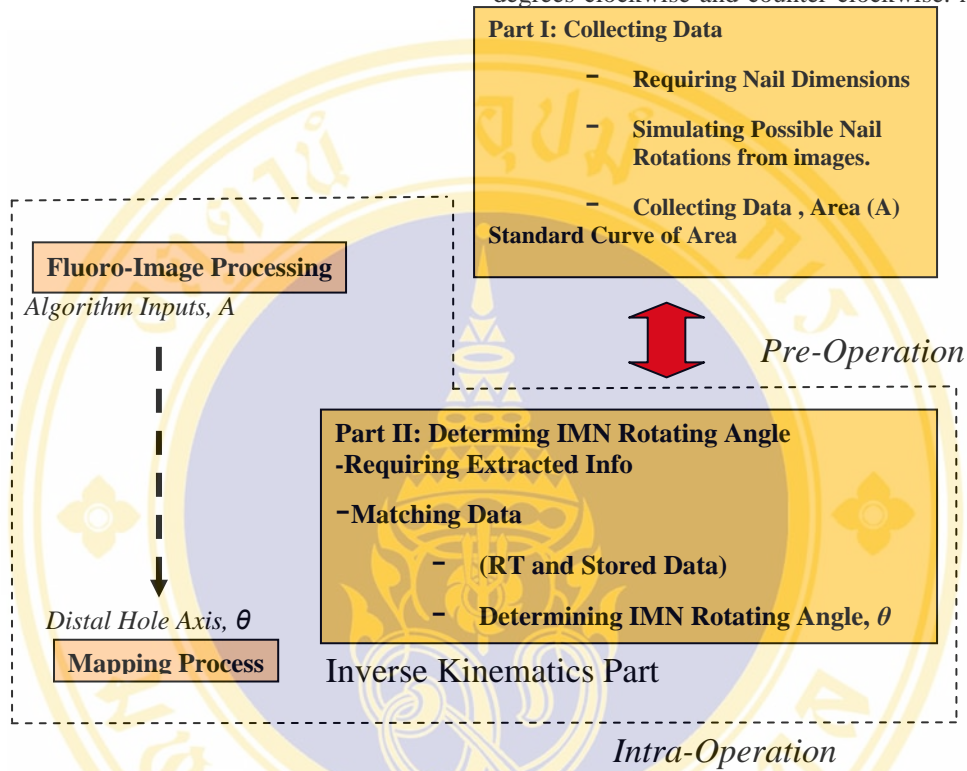


Fig 4.Overview of our approach

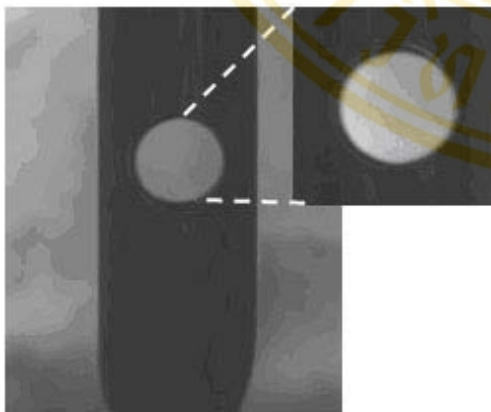


Fig 5.Interesting Part of X-Ray Image

**III. IMPLEMENTATION**

In order to prove our algorithm, an implementation is done by using our experimental set up. The assumptions of our implementation are: 1) nail rotates about its axis only; 2) nail is in a cylindrical shape; 3) the distal holes are in circular shapes and 4) diameters of nail and its distal holes are known.

The second step is to detect the distal hole part. Image cropping technique is applied to detect only interesting part of image. The area of distal holes are calculated and stored during the second step. The data of area vs. angle are plotted on its graph. A fitting curve technique is then applied to find the best fit to the data. The curve, called the "Tool Curve," is used to be the key to reversely determine rotating angle of the IMN.

*Part II: Determining the IMN rotating angle*

This part is to simulate during the intra-operation process. Images acquired from fluoroscopic system are instantly processed to determine the area of distal hole's projected image. Therefore, matching process of a real-time area data to the Tool Curve is to reversely recover the rotational angle of IMN. This is the same axis which can be used to represent the orientation of distal hole.

**IV. EXPERIMENTS AND RESULTS**

The experimental set up can be separated into 2 steps.

*Step I: Image preparation*

- To prepare database for Part I: Images of IMN rotation at 0, 5, 10, 15 and 20 degrees are taken for 10 data sets. This information is to generate the “Tool Curve.”
- To prepare database for Part II: Images of IMN rotation at 2, 4, 6, 8, 12, 14, 16 and 18 degrees are taken for 15 data sets. This information is used to determine the errors of our algorithm.

*Step II: Data analysis*

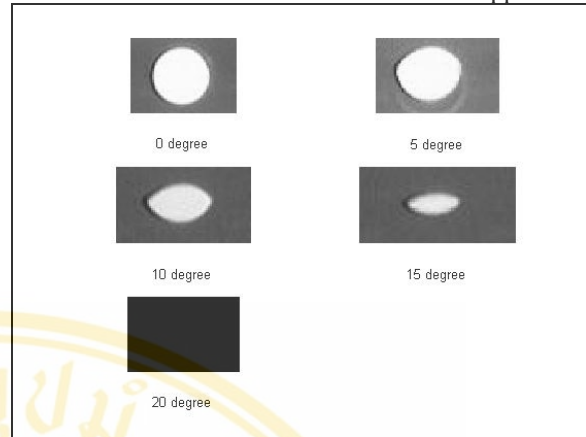
Compute average areas of the distal hole’s images using MATLAB. Construct the Tool Curve by plotting graph of area vs. rotational angle. It has been found that quadratic curve fitting technique is a proper selection. The equation is shown as followed:

$$\theta = ax^2 + bx + c$$

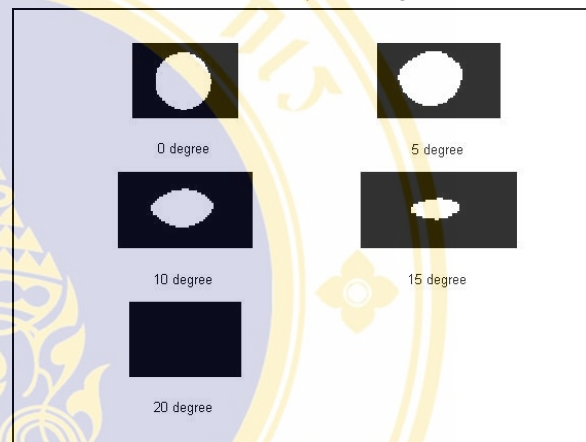
- $a$ ,  $b$  and  $c$  are constant values.
- $x$  is the input which is the computed area of an unknown image
- $\theta$  is the output which is the rotation angle in degree

Figures 6 (a), (b) and (c) show example of a series of image processing steps during the distal hole’s area determining process.

Average computed areas at different angles are plot in a graph of area vs. rotational angle. The “Tool Curve” is generated as shown in Figure 7. Table 1 shows experimental results from our algorithm.



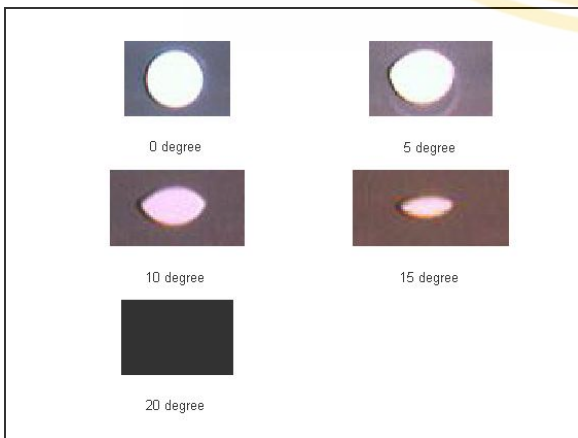
(b) Grayscale Images



(c) Binary Images



Fig 6. One data set of distal hole images at 0, 5, 10, 15 and 20 degrees (a) RGB Images (b) Grayscale Images (c) Binary Images.



(a) RGB images

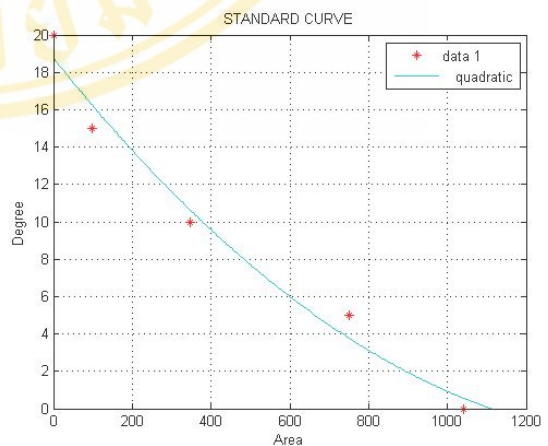


Fig 7. Tool Curve

Table 1 Distal hole's rotational angle recovered from our algorithm.

Expected Rotational Angle	Average Predicted Angle
2°	2.2854
4°	4.1335
6°	6.2041
8°	8.5826
12°	12.8454
14°	14.9214
16°	16.1414
18°	18.2370

## V. CONCLUSION

This paper discussed an implementation on recovering of IMN distal hole's orientation using a new algorithm which is using area of distal hole's projected images. Only two to three x-ray images are required during the hole's orientation recovery. In order to demonstrate the algorithm, a set of implementations is done by using MATLAB in an experimental set up to simulate acquiring x-ray images. The experimental results showed the positive potential of the new algorithm to be used in a real operation. The analyzed error of prediction is approximately 5.48% in average.

## REFERENCES

- [1] D. Stoianovici, L. L. Whitcomb, J. H. Anderson, R. H. Taylor, and L. R. Kovassi, "A Modular Surgical Robotic System for Image Guided Percutaneous Procedures," in *Proc. of the Int'l Conf. on Medical Image*, Trento, Italy, 1990.
- [2] R. H. Taylor, P. Jensen, L. L. Whitcomb, A. Barnes, R. Kumar, D. Stoianovici, P. Gupta, Z. Wang, E. de Juan, and L. R. Kavoussi, "A Steady-Hand Robotic System for Microsurgical Augmentation," *Journal of Robotics Research*, 1999.
- [3] H. Kang, and J. T. Wen, "Robotic Assistants Aid Surgeons during Minimally Invasive Procedures," *IEEE Engineering in Medicine and Biology*, Jan – Feb 2001.
- [4] G. Fichtinger, "Surgical Navigation, Registration, and Tracking," Available:<http://cisstweb.cs.jhu.edu/people/gabor/Cs-600.145/Lectures/RegTrack.pdf>
- [5] J. Suthakorn, I. Chuckpaiwong, and B. Mahaisavariya, "A Novel Surgical Guidance System Utilizing Hybrid Fluoro-Stereoscope Navigation For An Orthopedic Surgery," in *Proc. of The 8<sup>th</sup> International Research/Expert Conference (TMT2004)*, Neum, Bosnia and Herzegovina, 15-19 September, 2004.
- [6] C. Neatpisarnvanit, and J. Suthakorn, "Intramedullary Nail Distal Hole Axis Estimation Using Blob Analysis and Hough Transform," in *Proc. of The 2006 International Conference on Robotics, Automation and Mechatronics (RAM2006)*, Bangkok, Thailand, 7-9 June, 2006.
- [7] Y. Zhu, R. Phillips, J. G. Griffiths, W. Viant, A. Mohsen, and M. Bielby, "Recovery of Distal Hole Axis IntraMedullary Nail Trajectory Planning," in *Proc. of the 2001 Int'l Conf. on Robotics and Automation*, Seoul Korea, 2001, pp. 1561-1566.
- [8] U-Thainual P. and Suthakorn J. "A New Algorithm for Recovering Distal Holes' Pose in Intramedullary Nail," *Journal of Biomechanics* 2006, Vol. 39 Suppl. 1, page S209

**BIOGRAPHY**

<b>NAME</b>	Miss Paweena U-Thainual
<b>DATE OF BIRTH</b>	8 February 1983
<b>PLACE OF BIRTH</b>	Bangkok, Thailand
<b>INSTITUTIONS ATTENDED</b>	Mahidol University (2001-2005) Bachelor of Engineering (Mechanical Engineering) Mahidol University (2005-2007) Master of Engineering (Biomedical Engineering)
<b>HOME ADDRESS</b>	125/16 Moo 6, Kanjanapisek Rd, North Bangkae, Bangkae, Bangkok Email: paweena@bartlab.org